NUMERICAL AND EXPERIMENTAL INVESTIGATION OF INCREMENTAL SHEET FORMING

A MASTER'S THESIS

in

Manufacturing Engineering

Atilim University

by

M. EMİN TAMER

JUNE 2014

NUMERICAL AND EXPERIMENTAL INVESTIGATION OF INCREMENTAL SHEET FORMING

A THESIS SUBMITTED TO

THE GRADUATE SCHOOL OF NATURAL AND APPLIED SCIENCES

OF

ATILIM UNIVERSITY

BY

M. EMİN TAMER

IN PARTIAL FULFILLMENT OF THE REQUIREMENTS FOR THE DEGREE OF

MASTER OF SCIENCE

IN

THE DEPARTMENT OF MANUFACTURING ENGINEERING

JUNE 2014

Approval of the Graduate School of Natural and Applied Sciences, Atılım University.

_____

Prof. Dr. İbrahim Akman

Director

I certify that this thesis satisfies all the requirements as a thesis for the degree of Master of Science.

_____

Prof. Dr. Engin S. Kılıç

Head of Department

This is to certify that we have read the thesis "Numerical and Experimental Investigation of Incremental Sheet Forming" submitted by "M. Emin TAMER" and that in our opinion it is fully adequate, in scope and quality, as a thesis for the degree of Master of Science.

_____	_____
Asst. Prof. Dr. İzzet Özdemir	Asst. Prof. Dr. Besim Baranoğlu
Co-Supervisor	Supervisor

Examining Committee Members

Asst. Prof. Dr. Omer Music	_____
Asst. Prof. Besim Baranoğlu	_____
Asst. Prof. Dr. İzzet Özdemir	_____
Assc. Prof. Dr. Hasan Okuyucu	_____
Dr. İsmail Durgun	_____

Date: 04.06.2014

I declare and guarantee that all data, knowledge and information in this document has been obtained, processed and presented in accordance with academic rules and ethical conduct. Based on these rules and conduct, I have fully cited and referenced all material and results that are not original to this work.

Name, Last name: M.Emin Tamer

Signature:

ABSTRACT

NUMERICAL AND EXPERIMENTAL INVESTIGATION OF INCREMENTAL SHEET FORMING

Tamer, M. Emin

M.S., Manufacturing Engineering Department

Supervisor: Assoc. Prof. Dr. Besim Baranoğlu

Co-Supervisor: Assoc. Prof. Dr. İzzet Özdemir

June 2014, 113 pages

Prototype manufacturing necessitates the production in low quantities with as low cost as possible. It is for this reason, the production techniques utilized in mass production cannot be applied to prototype manufacturing.

Incremental sheet forming (ISF) process can be defined as forming the sheet metal by pressing a spherical-tip tool on a single point, or several such tools on multiple points and by changing the location of the point of the load. The process can be performed in a CNC vertical milling machine. In ISF, the plastic deformation occurs in the vicinity of the forming tool(s).

Unlike conventional sheet metal forming processes, where a full set of dies are to be used mostly, in ISF, either there is no need for utilization of dies, or use of partial dies or supports are employed in process.

The objective of this thesis is to predict the geometry, tolerances and strain history of a part that is manufactured with ISF (with a specific tool path obtained from the CAD of the product) through numerical simulations. The strain history may then be used to

predict the mechanical properties after the process. The results of the numerical simulations are verified through the comparison of the results with the measurements of those in a set of designed experiments where the same tool path is programmed to a CNC vertical milling machine to obtain the actual product. The aim of this study is to obtain a numerical simulation tool to evaluate and compare the outcomes of different forming strategies without manufacturing the product–a selected set of strategies may then be manufactured after the simulations.

Keywords: Incremental Sheet Forming Process, Prototype Manufacturing, Numerical Simulation.

ÖZ

ARTIMLI SAC ŞEKİLLENDİRME İŞLEMİNİN SAYISAL BENZETİM VE DENEYSEL OLARAK İNCELENMESİ

M. Emin, Tamer

Yüksek Lisans, İmalat Mühendisliği Bölümü

Tez Yöneticisi: Yrd. Doç. Dr. Besim Baranoğlu

Ortak Tez Yöneticisi: Yrd. Doç. Dr. İzzet Özdemir

Haziran 2014, 113 sayfa

Prototip imalat, düşük miktardaki üretimin mümkün olduğunca az maliyette olmasını gerektirmektedir. Bu nedenle, seri üretimde kullanılan üretim yöntemleri prototip imalata uygulanamaz.

Artımlı sac şekillendirme (ASŞ) işlemi, sac metale tek bir küresel uçlu takım ile tek noktaya ya da çeşitli takımlarla birden fazla noktaya baskı uygulayarak ve bu baskı nokta veya noktalarının zaman içinde yerlerinin değiştirilmesiyle şekil verilmesi işlemi olarak tanımlanabilir. İşlem, CNC dik işleme tezgahında gerçekleştirilebilir. ASŞ işleminde plastik deformasyon şekillendirme ucunun civarında meydana gelir.

Çoğunlukla tam bir kalıp setinin kullanıldığı geleneksel sac metal şekillendirme işlemlerinin aksine, ASŞ'de ya kalıp kullanılmasına gerek yoktur ya da kısmi kalıpların veya destek kalıplarının kullanılması işlem için yeterli olmaktadır. ASŞ işlemi seri üretimde derin çekme ya da presleme ile karşılaştırıldığında zaman alan bir işlem olmasına rağmen yeni bir parçanın yeni bir kalıp seti tasarlanması yerine tercih edilebilir.

Bu tezin amacı, ASŞ ile üretilen parçada (parçanın bilgisayar destekli çiziminden – CAD elde edilen özgül takım yolu ile) geometriyi, toleransları ve genleme geçmişini sayısal benzetimler yoluyla tahmin etmektir. Daha sonra genleme geçmişi, ASŞ işleminden sonra elde edilen parçanın mekanik özelliklerinin tespitinde kullanılabilir. Sayısal benzetim sonuçları, gerçek ürün elde etmek için aynı takım yolunun programlandığı bir dik işleme CNC fereze makinasında bir dizi deney sonuçları ile karşılaştırılarak doğrulanmıştır. Bu çalışmada amaçlanan, ürünü imal etmeden önce farklı şekillendirme yollarının çıktılarını çözümleyecek ve karşılaştıracak bir sayısal benzetim aracı geliştirmektir – bu yolla elde edilecek olan stratejiler daha sonra imalatta kullanılabilecektir.

Anahtar Kelimeler: Artımlı Sac Şekillendirme İşlemi, Prototip İmalat, Sayısal Benzetim.

To My Family

ACKNOWLEDGEMENTS

TABLE OF CONTENTS

LIST OF TABLES

TABLE

LIST OF FIGURES

FIGURES

xv

xvi

xx

LIST OF ABBREVIATIONS

ISF	Incremental Sheet Forming
CNC	Computer Numerical Control
CAD	Computer Aided Design
NC	Numerical Control
SPIF	Single Point Incremental Forming
IFWCT	Incremental Forming With Counter Tool
TPIF	Two Point Incremental Forming
B	Bending
S	Shear
TTS	Through Thickness Shear
FFLC	Fracture Forming Limit Curve
TRB	Tailor Rolled Blanks
FEM	Finite Element Method
Fe	Ferrous
MFCE	Metal Forming Centre of Excellence
HBT	Hydraulic Bulge Test
3D	Three Dimensional
ESPI	Electronic Speckle Pattern Interferometry
VPB	Viscous Pressure Bulge
FEA	Finite Element Analysis
CCD	Charge Coupled Device

FLD   Forming Limit Diagram

EDM   Electric Discharge Machine

NOMENCLATURE

t_i	Initial Thickness
t_f	Final Thickness
λ	Semi Cone Angle
ψ	Drawing Angle
Δz	Step Width
P	Load
l_o	Gauge Length of the Specimen
w_0	Width of the Specimen
t_0	Thickness of the Specimen
σ_t	True Stress
A	Current Area
$d\varepsilon$	Strain Increment
l	Current Length
ε	True Strain
σ	Flow Stress
K	Strength Index
n	Strain Hardening Coefficient
σ_1	True Stress in Tension Test Direction
σ_2	True Stress in Width Direction
σ_3	True Stress in Thickness Direction
σ_b	Balanced Stress at the Pole
p	Pressure
R	Radius of the Pole
t	Instantaneous Thickness
R_1, R_2	Corresponding Radius of the Curved Surfaces
d_c	Diameter of the Die Cavity

h$_d$	Dome Height
$\bar{\sigma}$	Equivalent Stress
$\bar{\varepsilon}$	Equivalent Strain
ε_x	Strain in Length Direction
ε_y	Strain in Width Direction
ε_z	Strain in Thickness Direction
R_d	Instantaneous Radius of Curvature
R_c	Fillet Cavity
t_d	Thickness at the Apex of the Dome
h_c	Dome Height
t_0	Initial Sheet Thickness
ε_1	Strain in Length Direction
ε_2	Strain in Width Direction
ε_3	Strain in thickness direction
β	Strain Ratio
M	Mass Matrix
a^n	Acceleration
d^n	Displacement
n	Time Step
f^n	Force at time Step n
$v^{n+1/2}$	Velocity
M_{IJ}^D	Lumped Mass Matrix
$\Delta t_{critical}$	Critical Time Step Size
l_e	Characteristic Length Element
c_e	Wave Speed
$r(d^{n+1}, t^{n+1})$	Residual Force
k	Iteration Counter
K	Consistent Tangent Matrix

CHAPTER 1

INTRODUCTION

1.1 General Aspects of ISF

The prototype manufacturing is the stage of design process where the designed parts are manufactured and assembled to obtain the prototype of the product and this prototype is then evaluated through a set of tests and experiments. The results of these tests and experiments constitute feedback to the design where mostly through this feedback, the design may be subject to some changes. The final design is obtained through iterations with prototyping stage. Therefore, it can be said that, the time-to-market of a new design is mostly affected by the prototyping stage of the process.

Since the design is subject to many changes within the iterations with the prototyping stage, prototype manufacturing needs flexible methods where the new or changed design can easily be manufactured in a comparatively small time. In sheet metal forming, however, high tooling costs and tool manufacturing times constitute a major drawback for the flexibility of the conventional forming methods such as deep drawing. Therefore, the different methods used in mass production have to be found and applied to the prototype manufacturing.

One of the simplest and oldest example of flexible forming is manual hammering of a sheet into a wooden die. This method is one of the most ancient methods of metal forming, which is still in use in the form of art. Nowadays, with the development of the Computer Numerical Control (CNC) technology, this hammering process can be programmed to a CNC punching machine – the advantage being the precise motion of the hammer by computer control and speeding up of the process.

Another flexible forming process is shot peen forming where steel pellets are shot to the surface of the sheet metal using compressed air. Every shot behaves like a peening hammer that produces elastic stretching and causes local plastic deformation. The joint-action of the tensile and compressive stresses generated as such, large regions such as panels can be formed.

The other flexible forming type is multi point forming which consists of two parts with several spherical-tip pins integrated to give the surface form of the tools in a discrete form. When one side of the tool forms the male die, the other side forms the female die [1]. The laser forming is a developing flexible forming process in which a localized region is subjected to deformation with a two phase heating and cooling process. The plastic strains induced by thermal stresses result bending in a preferential direction [2]. An alternative flexible forming method which is still in research is the water jet forming where a water jet is directed to the sheet metal surface creating local deformation on the corresponding contact region [1].

A most widely used flexible forming method is metal spinning, whose origins can be traced back to the art of potter's wheel in ancient Egypt [3]. This technique involves clamping a sheet metal blank against a rotating mandrel and gradually forming the sheet against the mandrel in either a single pass or a number of passes. It is one of the oldest flexible forming processes, and as such has inspired a number of new flexible forming processes. Nowadays, parallel to the developments on the CNC technology, the process can be automated. Finally, the most popular flexible forming process is ISF, which has been a subject of a large volume of research recently.
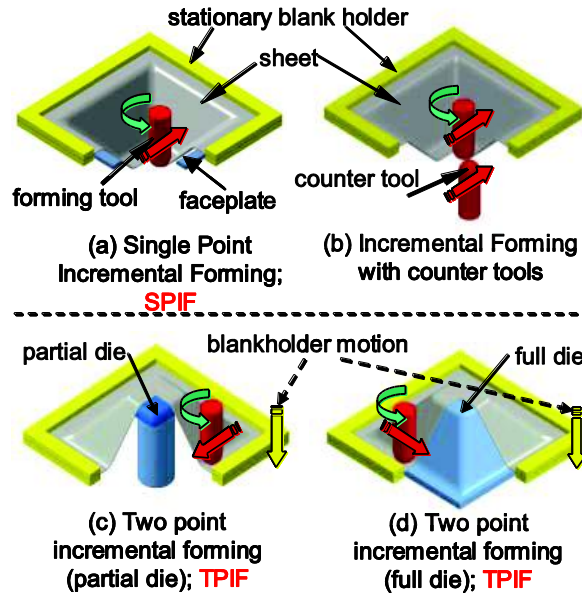
Figure 1.1 Schematic representation of variations in ISF [2].

Incremental sheet forming (ISF), which was first patented by Leszak [4], comes out from die-free forming with a spherical ended tool. The tool pushes into the sheet metal and the shaping occurs incrementally in which the tool follows a path obtained from CAD data [5].

In ISF process, both symmetric and asymmetric shapes can be manufactured by using spherical tool tips and controlling the tool movement in three dimensional space without expensive dies.

ISF process can be divided to four categories as illustrated in Figure 1.1. The first is single point incremental forming (SPIF) in which the sheet is clamped on the backing plate with a stationary metal frame or blank holder and an indenter moves on the sheet following a tool trajectory which is defined by CAM program. Figure 1.1-a zone's detailed illustration is given in Figure 1.2. The second is the incremental forming with counter tools (IFWCT) having the same configuration as in SPIF. The only change being the use of a counter tool against the moving indenter. The other categories are the two point incremental forming (TPIF) with partial and full die. In these processes (Figure 1.1 (c) and (d)), the sheet is formed against a full or partial die with a moving blank holder. In TPIF nonspecific or specific supports are used partial or full die respectively with the aim of enhancing the dimensional accuracy.
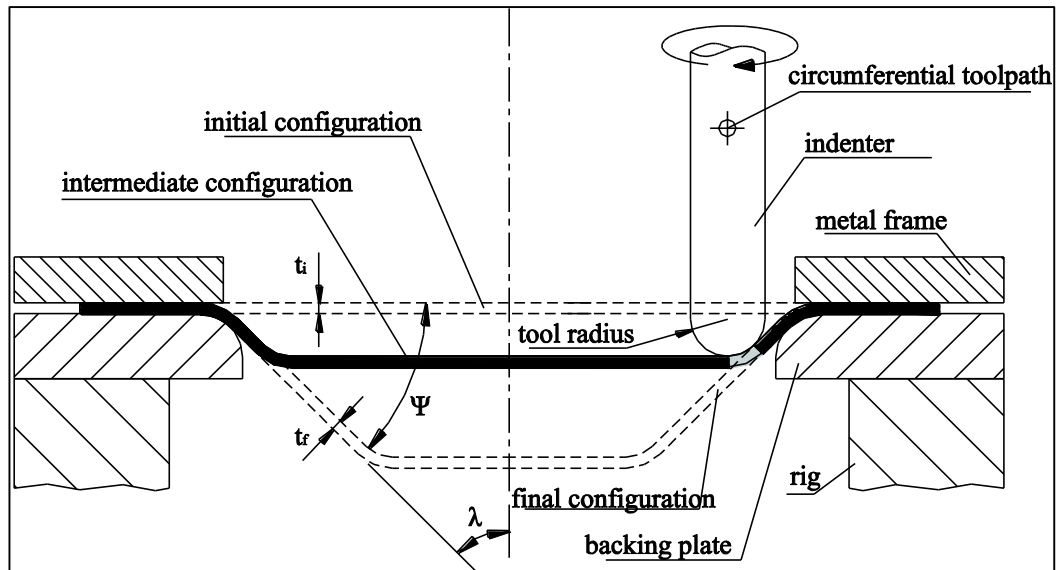
Figure 1.2 Schematic representation of SPIF from cross section view [6].

This study is carried out using SPIF with hemispherical carbide tools. The basic parameters of the process is displayed in Figure 1.2, where, t_i is the initial thickness, t_f is the final thickness of the blank, λ is the semi-cone angle and ψ is the drawing angle.

The ISF process has several advantages over conventional sheet metal forming processes, some of which are listed below:

- There are no expensive tools, dies and the use of dies are either eliminated or reduced,
- The process can be performed by any CNC vertical milling machine with 3 axes,
- The process flexibility is wider than conventional process techniques which means the only thing to be required is CAD drawing of the desired shape,
- The process is suitable for prototype manufacturing,
- The formability limits exceed the traditional forming limits [7] and a variety of geometries can be obtained (as seen in Figure 1.3).

On the other hand, there are some disadvantages such as:

- The manufacturing time is slow,
- The necessity of special care to be given to obtain the desired accuracy in geometrical tolerances.

4
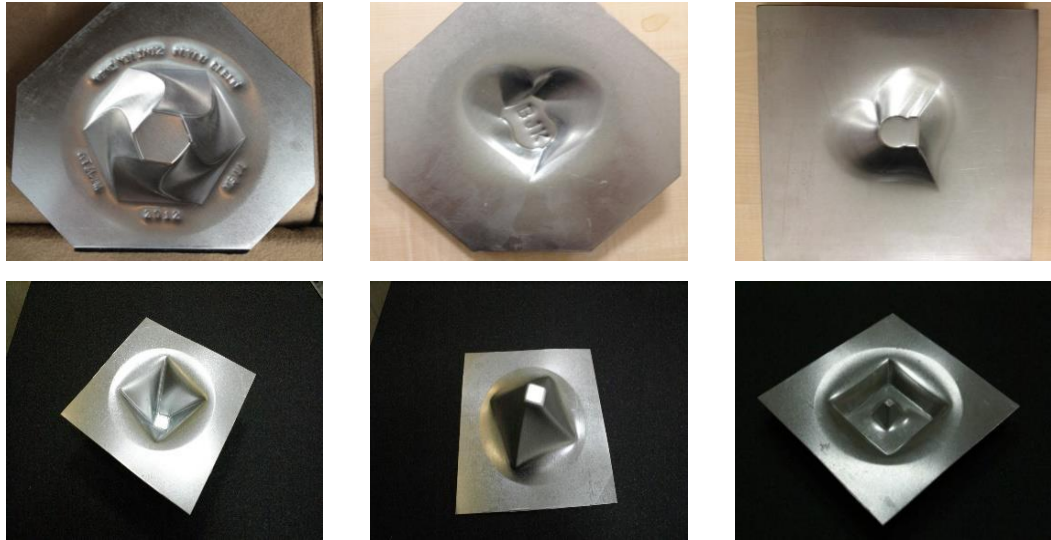
Figure 1.3 The manufactured parts by ISF with different shapes.

1.2 Aim and Scope of the Thesis Study

In this study, the main objective is to investigate the ISF process in detail with special emphasis on the geometrical tolerances, major-minor strains and thickness distributions manufacturing the shapes with different tool diameters and different depths, to optimize tool path strategy for complex parts which have steeper walls and to observe the difference of ISF and deep drawing processes.

1.3 Organization of Dissertation

This thesis consists of 6 chapters including this introduction and the conclusion parts. Chapter 2 gives brief explanation about deformation mechanism of ISF and the process parameters with literature survey. Chapter 3 includes numerical modeling with the proper material characterization. Chapter 4 gives the experimental results which falls into three groups: Experimental Setup of ISF, 3D Coordinate Measurements and Deformation Measurements. In Chapter 5, the results, which are obtained from numerical simulations and experiments, are compared and the verification is done. Finally, the discussion about findings are performed and the conclusion is given.

CHAPTER 2

THEORETICAL BACKGROUND

2.1 Deformation Mechanism of ISF

The mechanics of the ISF process can be characterized by small localized deformation region in the vicinity of tool and the blank. In ISF, there are several deformation mechanisms reported in literature [1], [2], [6], [7] and [8]. The deformation mechanisms can be described as;

- Bending under tension
- Cyclic straining
- Through thickness shear
- Plane strain tension
- Biaxial stretching

Contact stress is based on normal compressive stresses and the blank is affected locally by the tool [9]. In bending under tension mechanism, the tool bends and unbends the sheet continuously [10] and the stress is not uniform over the thickness of the sheet. The stress state is not changed so, the thickness stress is reduced while some part of the thickness is compressed. In the cyclic straining, the tool passes through a certain material point several times, in each pass the tool causes bending and unbending [9]. Figure 2.1 shows the deformation where the thick line indicates the high contact stress zones. If the tool diameter is small, then the stresses will be very high. Additionally, the deformed wall shows a simple stretch in perpendicular with little or no shear.
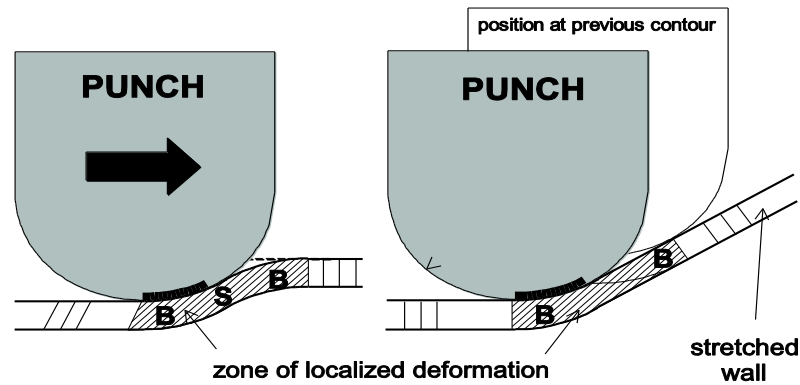
Figure 2.1 The localized deformation between the tool and the contact. B is bending,
S is shear and triple lines show the shear or stretch [9].

Emmens et al. [10] have also mentioned bending under tension mechanism. In order to investigate the mechanism, tension tests with repetitive bending were performed. It was concluded that the stretching with simultaneous bending does allow large uniform straining even in low angle of bending.

The other mechanism is based on an assumption of hydrostatic pressure. Jeswiet et al. [2] mentioned that the mechanics can be defined due to the hydrostatic pressure caused by elastic deformation zone. A high level hydrostatic stress has an effect on evolution of the voids and the voids affect the fracture limit. So, much higher strains can be obtained due to presence of hydrostatic stress. Also, Bambach et al. [11] have investigated the deformation mechanism and concluded that the hydrostatic pressure comes out during shaping the sheet, thus it indicates higher formability limits in ISF process as compared to conventional forming processes.

The through thickness shear (TTS) mechanism is caused by the tool movement which occurs in the direction of the indenter ([12], [13]). The shear prevents the necking due to no tension in the plane of the sheet [8]. Shear decreases the yield stress in tension and raises the necking limit up to a certain level. Hence, the formability of the incrementally formed parts would be higher. The presence of through thickness shear has been detected in [12], by measuring the relative displacement of both surfaces of a sandwich panel. Another study from Eyckens et al. [14] which was aimed to present the experimental measurements of (TTS).

The plane strain stretching mechanism occurs at rotational symmetric surfaces and flat surfaces of the parts. However, the deformation behavior of truncated square pyramids shows biaxial stretching condition at the transition region between the one side of lateral surface and the other side (Figure 2.2).

Figure 2.2 The deformation behaviors are different at lateral sides and transition regions.

Silva et al. [6] have aimed to find answers to several unknown mechanics of ISF such as the state of stress and strain at the small plastic zone and the crack occurrence while the transition between the inclined walls and the corner radius whether caused by shear or tensile stresses. In order to answer these issues, they have investigated membrane analysis of the small plastic zone neglecting the bending moments due to the assumption of circumferential, meridional and thickness stresses to be the principle stresses. It was concluded that the cracks may occur due to the meridional tensile stresses instead of in-plane shearing stresses.

Another study was performed by Silva et al. [15], in which the applicability of analytical model (which was obtained in [6]) has been investigated to the different modes of deformation, especially in truncated square pyramids. They have also investigated the influence of the triaxility ratio σ_m/σ_{eq} which plays a significant role in the formability of the materials. They have concluded that the onset of the cracks are located at the corners in pyramidal shapes due to the triaxility ratio and the corners has equ-biaxial stretching conditions then the ratio is higher as compared to plane strain conditions.

The other subject in ISF process is forming limits which is higher than conventional forming limits. Skjoedt et al. [16] have been aimed to check whether fracture forming limit curve (FFLC) can be established the forming limits of multistage ISF. They have also aimed to present an enhanced multistage ISF to produce flat bottom cylindrical cups with steeper walls. The movement of the tool is performed in the direction of downward and upward, respectively. The upward going tool implies more biaxial strains than downward moving tool head. The correlation between the experimental FFLC and the resulting from the theoretical framework was good and provided that SPIF is limited by fracture instead of necking. By using multistage strategies it was allowed to produce flat bottom cylindrical cups with steep walls.

Filice et al. [17] have investigated that the material formability can be characterized by taking into account a wide range of straining conditions. Hence, different test procedures are prepared to obtain the straining conditions which are differing from pure uniaxial stretching to fully biaxial stretching. In pure uniaxial stretching a square loop consisting of four strain lines in which each loop the punch moves vertically to the blank. However, in biaxial stretching the tool trajectory was a simple cross consisting of two perpendicular lines. Also, a third type of test in which a spiral tool path was used. It was concluded that the forming limit curve in ISF was quite different from the conventional forming. Much higher strains be achieved rather than conventional forming process. Therefore, the fracture limits are higher than traditional forming process.

2.2 Process Parameters

In ISF, there are several parameters that effects the process in terms of formability, process time, dimensional accuracy and surface quality. Those are;

- Speed of the tool movement (feedrate)
- Step width (Δz)
- Tool diameter
- Thickness of the material
- Tool path strategy
- Lubrication

The feedrate is defined as the speed of the forming tool which moves around the mill bed. It has a significant role on the process time. As mentioned before, the ISF process is relatively time consuming as compared to traditional stamping or deep drawing processes. If the feedrate increased or decreased, the process time could be lower or higher. Additionally, by changing the feedrate the formability would be affected due to the frictional conditions [2]. If the feedrate adversely effects the formability, the different tool setups could be used. Kwiatkowski et al. [18] have been investigated the use of more than one tool for reducing the process time considering the formability. They have achieved this by using twin tool setup.

The orange peel effect, which is explained in [19], is a defect which occurs when the forming tool is in a close contact only with one side of the sheet. Since there are different orientations of neighboring grains at the surface, Hamilton et al. [20] have investigated the feasibility of forming at high feed rates, the orange peel effect and a model showing the limits of forming before the orange peel effect occurs. They have obtained consistent results in the sight of thickness distributions when the comparison is made between the high feedrate forming and low feedrate forming.

The step width can be defined as the amount of material, deformed for each revolution of the forming tool. It influences the process time, formability and the surface quality. The lower step width increases the process time, while it increases the formability and surface quality. In [18], it was mentioned that the maximum pitch is limited with the tool radius. The maximum step width should be chosen as 1/15 of the tool radius. In Hagan et al. [21] study, it was mentioned that the formability is influenced by the ratio of step width to the initial thickness. The forming limit increases when this ratio decreases below a value of 2. Also, it is mentioned that the small step widths would increase the forming limit of the blank.

The smaller tools enhance the formability due to gathering strains nearby the contact area. In contrast, using a larger tool diameter lowers the formability since it behaves like conventional sheet metal forming processes since the tool may distribute the strains over a more enlarged area [19].

The thickness of the material effects the formability. In ISF, the sheet gets thinner much more than deep drawing process due to the deformation mechanism. Hence, the sheet has excessive thinning. Hirt et al. [22] have investigated formability by using

tailor rolled blanks (TRB) especially for compensating the excessive thinning. They have manufactured the part with the flange angles 63^0 and 45^0. It was concluded that the use of TRB affected the sheet thickness positively.

Additionally, the sine law, which is mentioned in several studies ([1], [2], [6], [7], [8], [23]), is a geometrical model for predicting the final thickness in ISF. It depends on the assumption that the deformation of the undeformed sheet onto the surface of the final part. The formulation is given below:

$$t_f = t_i sin\lambda \qquad\qquad\qquad Eq.2.1$$

Probably the most important parameter in ISF process is the tool path strategy. Indeed, it influences formability, process time, surface quality and dimensional accuracy. One of the drawback for obtaining desired shape is dimensional errors. The first reason for dimensional errors can be a relevant sheet bending which closes to the bottom base of the part. However, it can be solved by using a backing plate whose edge hole is close to the forming zone. The second reason may be the springback occurrence when the clamp is relaxed after the process or after the trimming operation. The final reason could be the pillow effect happening on the top base due to smaller tool tip and the contact stress (Figure 2.3).
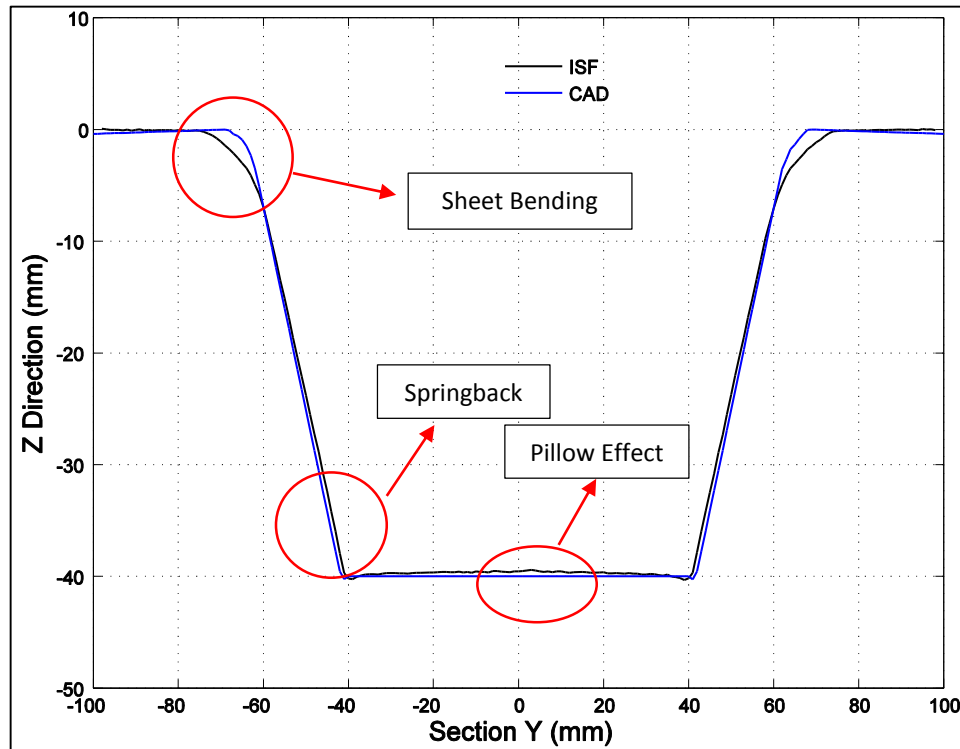
Figure 2.3 The illustration of possible dimensional errors in ISF process.

Micari et al. [7] have proposed to reduce the dimensional errors in terms of geometry. In order to improve the dimensional accuracy they have observed some relevant solutions. The first solution was the use of flexible support which has a rubber counter tool with the aim of reducing springback. The second solution was the use of counter pressure by utilizing pressured water. The third one was the multipoint incremental forming. The final solution was backdrawing incremental forming technique, which was based on a simple punch working at the both sides of the blank. It was concluded that it was possible to manufacture parts which have 90^0 wall angle using backdrawing incremental forming.

Generally, for complicated parts having steep walls, the achievement in manufacturing these parts is not possible. The different tool paths or multi-stage strategies should be used. The two tool path algorithms, z-level finishing and arbitrary stock roughing, are commonly used in ISF process. From the view point of process time and surface quality, there are some differences between z-level finishing and arbitrary stock roughing algorithm while manufacturing the parts. The process time is shorter while using z-level finishing algorithm, because the tool path trajectory is shorter. Also, the surface quality is better than in stock roughing algorithm (Figure 2.4).

(a)   (b)
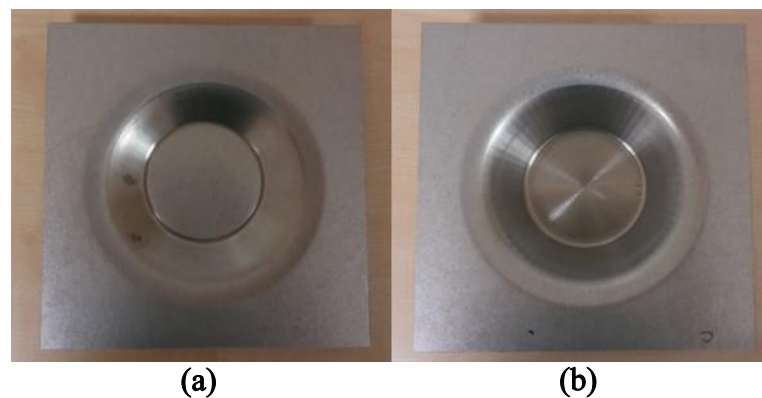
Figure 2.4 (a) the truncated cone, manufactured by using z-level finishing algorithm, (b) the truncated cone, manufactured by stock roughing algorithm.

Duflou et al. [19] have investigated the mechanics of the tool path strategy. In order to achieve this, a conical part has been manufactured in five steps which is started from 50^0 wall angle and continue with the increasing angle of 10^0. They have experimentally obtained that the maximum strains in both circumferential and meridional directions

arising at the base part of the adjacent of inclined wall. Bambach et al. [24] have studied multi-stage strategies which are used to improve the geometric accuracy. By using multi-stage forming, it could be possible to reduce the local springback in the final forming stage. Ambrogio et al. [25] have investigated the reduction of dimensional errors in ISF. They have compared ISF, backdrawing ISF and double backdrawing ISF processes. It was concluded that the backdrawing ISF results reduce the dimensional error. In Attanasio et al. study [26], it was aimed to investigate the experimental evolution of the tool path for an automotive component to obtain dimensional accuracy, good surface quality and the lowest sheet thinning by optimization of the tool path in TPIF with a full die. The die and the blank holder were made of epoxy resin in order to reduce the tool cost. As a result, for the best dimensional accuracy could be achieved by using the lower step widths. Ham et al. [27] have also investigated the dimensional accuracy using different methods.

The lubrication, which is essential in SPIF, does not affect the process in a good manner as compared to other influences. However, the lubrication is significant to reduce the friction, thus to improve the surface quality. If there is no lubrication while forming operation, there will be severe wear both on the indenter and the sheet surface.

Finally, this study includes the comparison the numerical results with experimental data in order to investigate the geometrical and deformation behavior. Bambach et al. [11] have aimed to use finite element framework by using explicit models. They have predicted the thickness distribution, necking and geometric accuracy which were compared with experimental results. It was mentioned that the deformation mode on flat surfaces was very close to plane strain conditions due to optical deformation measurements. Additionally, the measurements of sheet thickness showed that the amount of necking appears to be influenced by step width and the tool diameter. It was concluded that the shell elements used for modelling ISF gave good results as compared to experimental as far as sheet thickness and geometric accuracy. Moreover, the plastic deformation was found to be accompanied by hydrostatic pressure.

In Dejardin et al. [28] study, the improvement of final shape accuracy, elastic springback and sheet thinning are investigated. Another study from Dejardin et al. [29] also includes the investigation the agreement between the numerical and experimental results to assess the convenience of the model. They have focused on the reliable relationship between ISF and process parameters. They have compared finite element

results which is based on shell elements with the geometrical accuracy. Also, an explicit time integration scheme is used with an adaptive mesh refinement execution. The purpose of this is to reduce the element size when the distortion level reaches a maximum value. Finally, a comparison of finite element results and optical measurement results are carried out. A proper conclusion is observed where the maximum error does not exceed 3%. So, they have concluded that the explicit analysis gives accurate results in terms of geometrical comparison.

CHAPTER 3

NUMERICAL MODELING

3.1 Introduction

Finite element based modelling of the ISF process is a challenging task due to complex tool paths, large strain plasticity and evolving contact between the blank and the tool. An integral part of numerical modelling in metal forming is proper material characterization. In fact, the predictive capabilities of the numerical models are largely dictated by the quality of the material and interface (friction) characterization.

In this chapter, first the characterization tests carried out in this study are briefly mentioned. Afterwards, the procedure used to construct the flow curve from the experimental data of different tests is presented. Identified flow curves are used in the numerical modelling part which is presented in section 3.3. Modelling of the ISF process is realized using the finite element method (FEM) and essentials of the solution algorithms are given in the subsections of section 3.3. The actual model constructed using commercial FE package Abaqus® is presented in the last section including the details such as element type, mesh density and boundary conditions.

3.2 Material Characterization Tests

In this study, 0.8 mm thick Fe P04 sheets supplied by Tofaş A.Ş are used for material characterization. European equivalents of Fe P04 is DC04 non-alloy quality steel [30]. Zinc coated sheets are cold rolled and suitable for cold forming operations.

3.2.1 Tensile Test

Probably the most commonly used characterization test for sheet metals is the uniaxial tension test. This test is preferable due to its simplicity and well defined testing standards [31]. The mechanical properties such as Young's modulus, Poisson's ratio, anisotropy, yield strength, and ultimate tensile strength can be determined by using this test. However, it should be noted that, the maximum strain level that can be reached is 0.24, which is low as compared to strain levels reached in cold forming operations. Tensile test is carried out by extension of a flat specimen (Figure 3.1) with two jaws. One of the jaw is fixed and the other jaw can be moved in other direction by applying force (P). During the elongation of the specimen, force-displacement data is recorded by data acquisition system. In Figure 3.1, a standard tensile test specimen is shown, where l_0 is the gauge length, w_0 is the width and t_0 is the thickness of the specimen.
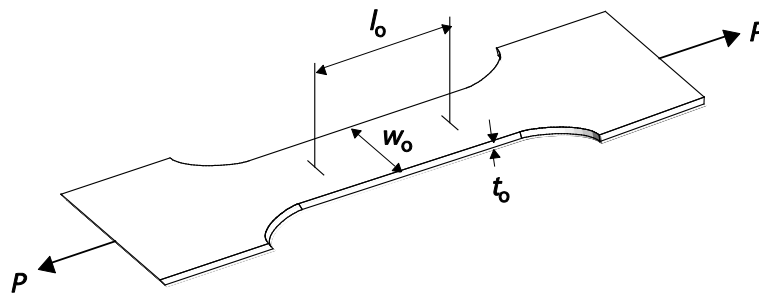
Figure 3.1 A standard tensile test specimen with the parameters [32].

| (a) | (b) |
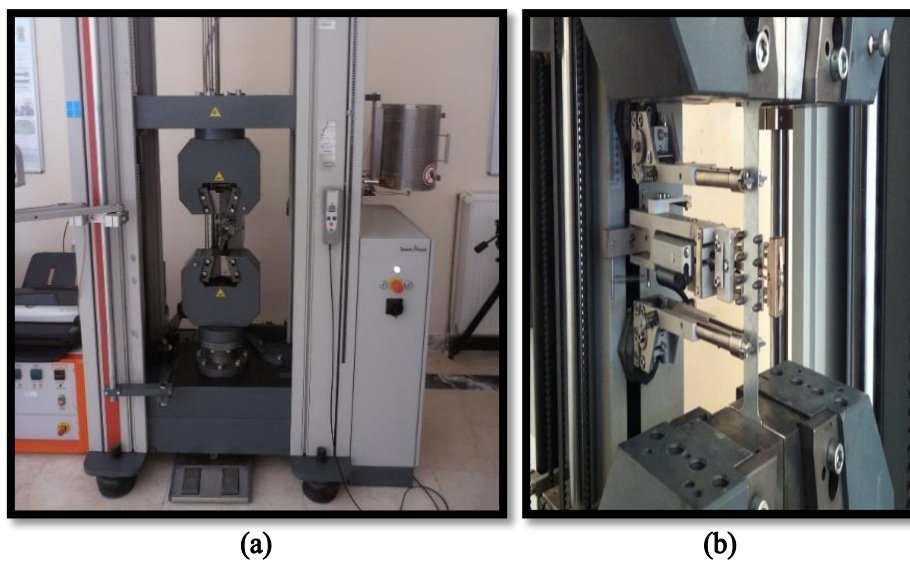
Figure 3.2 (a) Tensile test device in MFCE and (b) a tensile test is being performed with macro and transverse extensometers.

The tensile tests were performed in Metal Forming Center of Excellence (MFCE) using Zwick/Roell Z300 tensile testing device with 300 kN capacity which has a macro-extensometer and a transverse-extensometer (Figure 3.2).

The tests are performed with three repetitions in each direction (rolling, diagonal and transverse) at 150 mm/min speed.

After the tests, the force-displacement datum are converted into stress-strain curves using the true stress and true strain expressions [33].

$$\sigma_t = \frac{P}{A} \qquad\qquad\qquad Eq.3.1$$

$$d\varepsilon = \int_{l_0}^{l} \frac{dl}{l} \rightarrow \varepsilon = \ln\frac{l}{l_0} \qquad\qquad\qquad Eq.3.2$$

respectively, where, σ_t is the true stress, ε is the true strain and l is the current length of the specimen. The flow curves are shown in Figure 3.3.
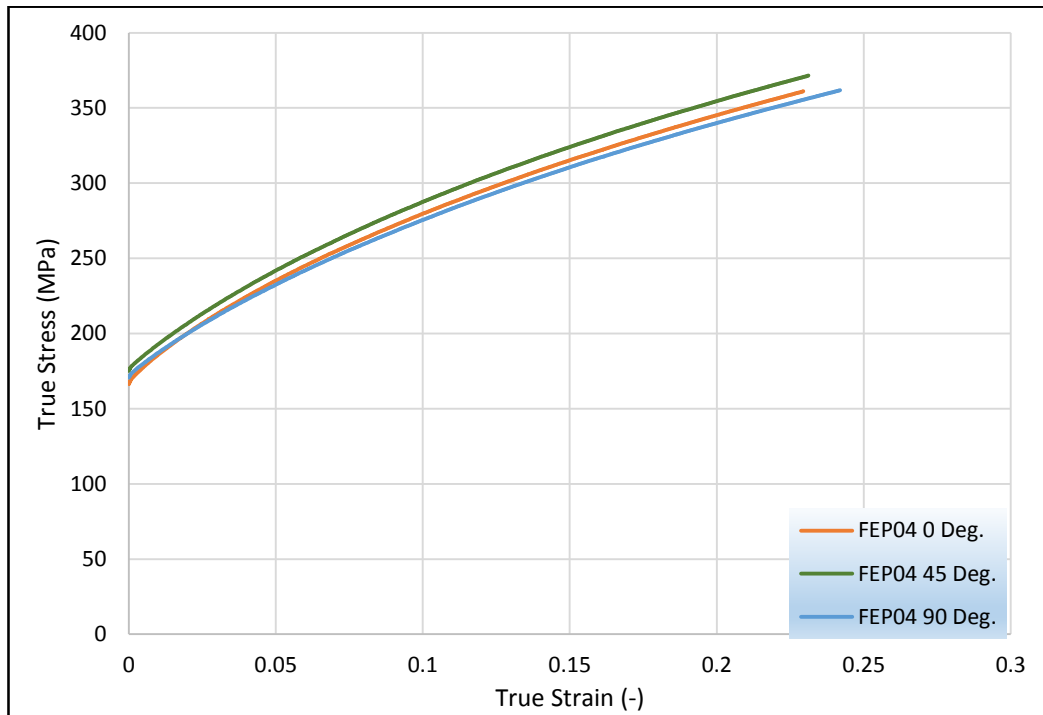
Figure 3.3 Flow curves of FEP04 in each direction obtained by tensile test.

Since, in ISF process the total strain value reaches to 2, the characterization based on uniaxial testing is not sufficient. These flow curves can be extrapolated to cover the whole strain range by using different flow models such as

$$\sigma = \sigma_0 + K.\varepsilon^n \ Ludwick - Hollomon \ Equation \qquad\qquad Eq.3.3$$

$$\sigma = (A * (\varepsilon + B)^n) - C \ \ Ghosh \ Equation \qquad\qquad Eq.\,3.4$$

$$\sigma = A - (A - B) * e^{-a\varepsilon^p} \ Hockett - Sherby \ Equation \qquad\qquad Eq.\,3.5$$

where,

- σ: Flow Stress(MPa)
- K: Strength index (MPa)
- ε: Strain
- n: Strain hardening coefficient
- A: Saturation stress
- B: Initial stress
- C: Coefficient in strain hardening law
- a & p: Exponents in the Hockett-Sherby strain hardening law
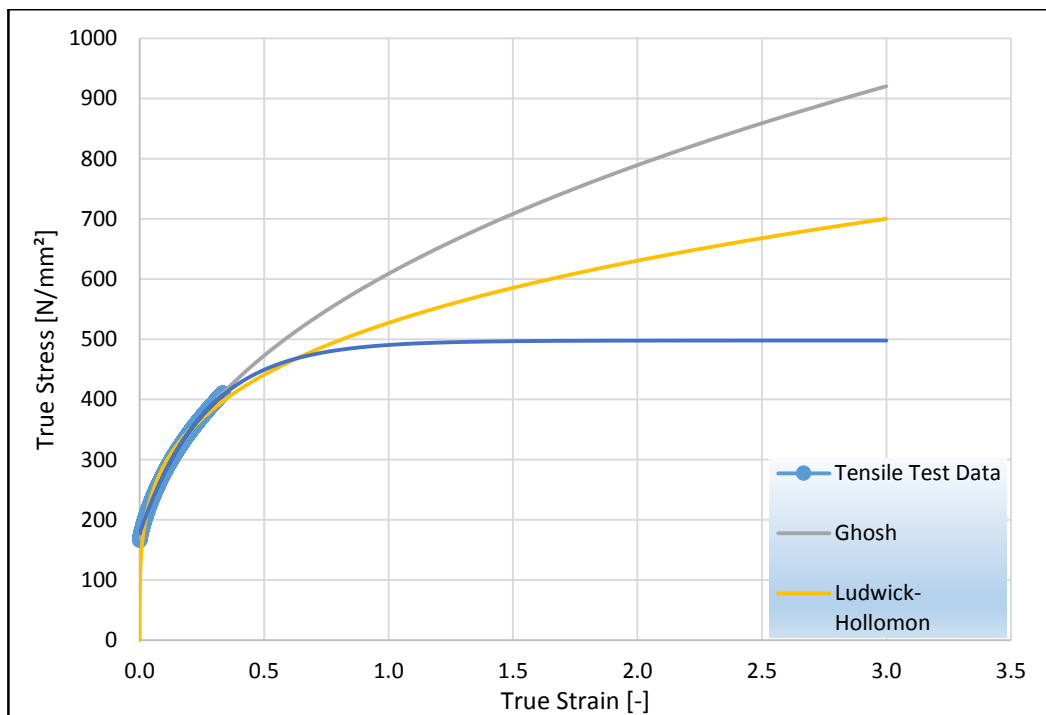
Figure 3.4 Different flow curves of FEP04 with respect to different material models.

The extrapolated curves are shown in Figure 3.4 from which the large differences are clearly seen. In order to obtain a general flow curve, the data taken from other experiments should be used. In the following subsection, the hydraulic bulge test (HBT) is explained.

3.2.3 Hydraulic Bulge Test (HBT)

The Hydraulic Bulge Test (HBT) is a convenient and commonly used experiment for obtaining flow curve which provides higher strains without the necessity of extrapolation beyond the limits of tensile test data.

The major advantage of this test is the absence of friction [34]. In HBT, a flat sheet metal is formed by oil pressure until the sheet cracks. The oil constructs a homogeneous pressure (see Figure 3.6) on the sheet metal internal surface which is being measured by a measurement sensor on the device. Moreover, the pressure causes a biaxial strain state on the material point located at the pole.
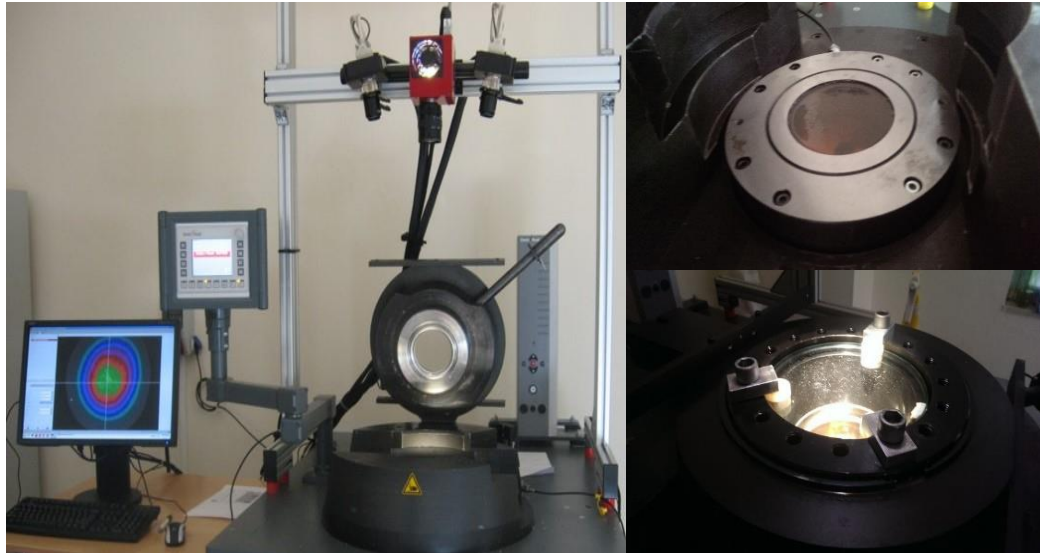
Figure 3.5 The experimental setup of HBT.

In HBT, the flat sheet metal is clamped around its edges which is exposed to fluid pressure supplied by oil under the sheet. On the top of the experimental setup, ARAMIS 3D deformation analysis system is located. To avoid from oil splash, the tempered glass cover is used. In Figure 3.5, the experimental setup can be seen.

Assuming that,

- the stresses at the pole are balanced $\sigma_1 = \sigma_2 = \sigma_b$ [34],

- the effect of bending is negligible,
- the shape of the deformed part resembles to spherical cup,
- the material is incompressible,

one can use the equation,

$$\sigma_b = \frac{p.R}{2.t}$$
Eq.3.6

which is based on the membrane theory and known as Kessel formula [34]. In equation 3.6, R is the radius of the pole, t is the instantaneous thickness, and p is the pressure.

In literature, there are several studies on material characterization with HBT. Koç et al. [35] used HBT setup with spherical die cavity under cold and elevated temperature conditions for calculating the flow curves. They have concluded that in room temperature conditions, non-contact optical measurement system gives acceptable results. However, in elevated temperatures (150^0C, 260^0C [36]) optical measurement system's results lead to large deviations. They have mentioned that electronic speckle pattern interferometry (ESPI) and laser optical methods are quite useful for obtaining good results at several elevated temperatures as compared to optical measurement system Aramis.

Another study for determination of flow curves was proposed by Gutscher et al. [37]. They applied the pressure on the internal surface of the sheet by using viscous material instead of hydraulic oil. This method is called as viscous pressure bulge (VPB) test. They have obtained larger strains which are relevant to stamping process. They have already compared VPB results with the tensile test data. They have also studied the relationship between the geometrical and material variables such as dome wall thinning, dome height and dome radius. It was concluded that, although use of viscous material instead of oil has made the VPB test simpler and easier, VPB test gives wrong results at high deformation velocities, since the viscous material is strain rate dependent.

Altan et al. [38] have developed an elliptical bulge test method to determine the flow curve and anisotropy coefficients. They also compared the experimental results with FEA. It was concluded that the flow stress along the rolling direction is higher as compared to tensile test data. In contrast, the strain hardening coefficient is

approximately same in both tests. However, the anisotropy coefficients obtained from bulge test were lower than the tensile test.

In HBT, the membrane theory is used to determine the flow curve [37]. The membrane theory neglects bending stresses which is acceptable for thin sheet metals. According to the numerical examinations, the bending effects can be neglected for the sheets which have the thickness range of 0.5 mm up to 3 mm and the membrane theory is valid [39].
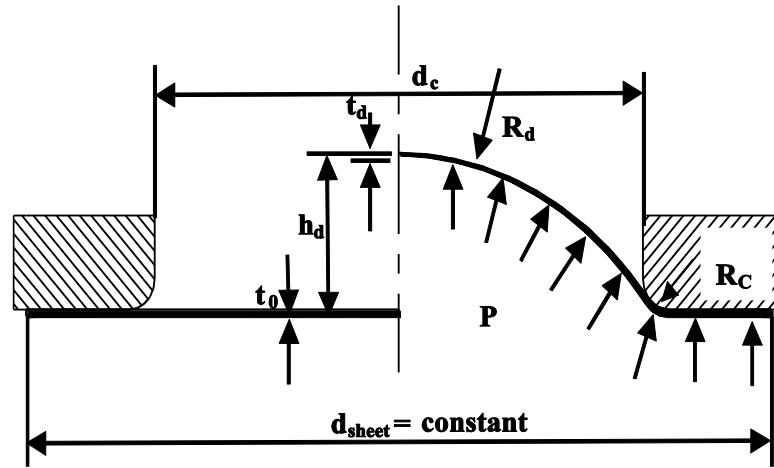
Figure 3.6 Schematic illustration of the bulge test [37].

According to the figure, the relationship between stress, sheet geometry and bulge pressure is:

$$\frac{\sigma_1}{R_1} + \frac{\sigma_2}{R_2} = \frac{p}{t}$$

<div align="right">Eq.3.7</div>

where σ_1 and σ_2 are the principal stresses on the sheet surface, R_1 and R_2 are the corresponding radii of the curved surface, p is the oil pressure and t is the sheet thickness. Due to axisymmetry of the geometry,

$$\sigma_1 = \sigma_2 = \sigma$$

<div align="right">Eq.3.8</div>

and the radius of the dome at the apex is

$$R_1 = R_2 = R_d$$

<div align="right">Eq.3.9</div>

Therefore, equation $Eq.\,3.7$ simplifies to,

$$\sigma = \frac{pR_d}{2t_d} \qquad \text{Eq.3.10}$$

where t_d is the thickness at the top of the dome. The pressure is applied on the internal surface. No normal forces act on the outer surface. So, the average stress σ_n is

$$\sigma_n = \frac{1}{2}(-p+0) = \frac{1}{2}(-p) \qquad \text{Eq.3.11}$$

The equivalent stress $\bar{\sigma}$ can be calculated then both by using Tresca and von Mises plastic flow criterion as;

- Tresca:

$$\bar{\sigma} = \sigma_{max} - \sigma_{min} = \frac{pR_d}{2t_d} - \left(-\frac{p}{2}\right) \qquad \text{Eq.3.12}$$

$$\bar{\sigma} = \frac{p}{2}\left(\frac{R_d}{t_d} + 1\right) \qquad \text{Eq.3.13}$$

- Von Mises:

$$\bar{\sigma} = \sqrt{\frac{1}{2}\left[\left(\sigma_1 - \sigma_2\right)^2 + \left(\sigma_2 - \sigma_3\right)^2 + \left(\sigma_3 - \sigma_1\right)^2\right]} \qquad \text{Eq.3.14}$$

$$\bar{\sigma} = \sqrt{\frac{1}{2}\left[\left(\frac{pR_d}{2t_d} + \frac{p}{2}\right)^2 + \left(-\frac{p}{2} - \frac{pR_d}{2t_d}\right)^2\right]} \qquad \text{Eq.3.15}$$

$$\bar{\sigma} = \frac{p}{2}\left(\frac{R_d}{t_d} + 1\right) \qquad \text{Eq.3.16}$$

The equivalent strain $\bar{\varepsilon}$ can be calculated using material incompressibility, which implies:

$$\varepsilon_x + \varepsilon_y + \varepsilon_z = 0 \qquad \text{Eq.3.17}$$

$$\varepsilon_x + \varepsilon_y = -\varepsilon_z \qquad \text{Eq.3.18}$$

$$\bar{\varepsilon} = -\varepsilon_z = -\varepsilon_t = \ln\frac{t_d}{t_0} \qquad \text{Eq.3.19}$$

In order to calculate flow stress using Eq.3.16, in addition to internal pressure p, instantaneous radius of curvature of R_d, thickness and dome height have to be known.

The radius at the top of the dome can be calculated by assuming that the dome is spherical,

$$R_d = \frac{d_c^2 + 4h_d^2}{8h_d}$$ Eq.3.20

where d_c is the diameter of the cavity and h_d is the dome height. Considering the fillet in the cavity R_c (see Figure 3.6), the radius of the dome can be calculated by,

$$R_d = \frac{(\frac{d_c}{2} + R_c)^2 + h_d^2 - 2R_ch_d}{2h_d}$$ Eq.3.21

In HBT, one of the most important parameter is the determination of the thickness at the apex of the dome. Assuming that the locus of each point on the sheet is a circle during deformation the wall thickness at the top is,

$$t_d = t_0 (\frac{1}{1 + (2h_d / d_c)^2})^2$$ Eq.3.22

where,

t_d: Thickness at the apex of the dome. h_c: Dome height.

t_0: Initial sheet thickness. d_c: Diameter of the cavity.

This equation was improved by Chakrabarty and Alexander [37] who took strain hardening into account and got

$$t_d = t_0 (\frac{1}{1 + (2h_d / d_c)^2})^{2-n}$$ Eq.3.23

where,

n is strain hardening coefficient. It is concluded that n-value influences the dome height and the thickness of the dome which means that the material with larger strain hardening coefficient has a larger thickness at the top of the pole.

Algorithmic steps of flow curve construction using HBT data is shown in Figure 3.7.

Flow Chart
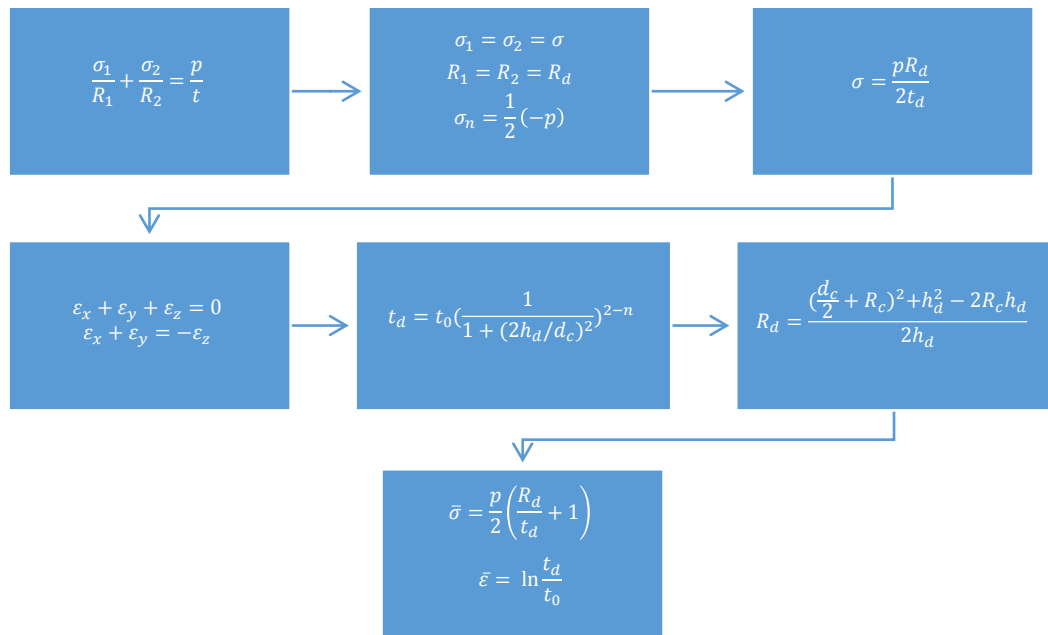
Figure 3.7 Flow curve calculation using HBT data.

Experimental Work

The HBT tests are performed by using Zwick/Roell BUP 600 Nakazima testing device which has 600 kN capacity with integrated Aramis 3D deformation analysis system (see Figure 3.22). As seen in Figure 3.8, Aramis has a typical sensor which includes two CCD (charge coupled device) cameras and a light source. Before the measurement, the cameras are adjusted for the measurement using the apertures on the camera. Then the calibration is done.

Figure 3.8 Aramis system with CCD cameras and a light source.

In order to prevent the reflection of the light and measure deformation of the sheet a stochastic pattern is created on the outer surface of the specimen (Figure 3.9). The uncertainty in the strain and thickness calculation is reduced by measuring the points on the sample's surface due to the stochastic pattern. In Figure 3.8, it can be seen that the black dots helps the software to carry out the strain and thickness calculations.
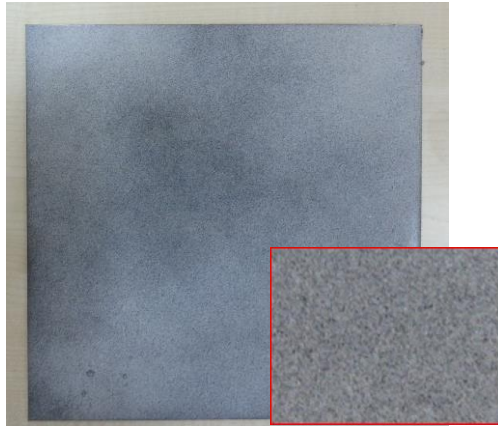
Figure 3.9 FEP04 sample with stochastic pattern.

After the application of stochastic pattern onto 200x200 mm square specimens, the measurements are performed with the following measurement parameters:

- Clamping force: 340 kN.
- Cupping speed: 2.5 mm/m.
- Cupping force: 550000 kN.

(a)   (b)
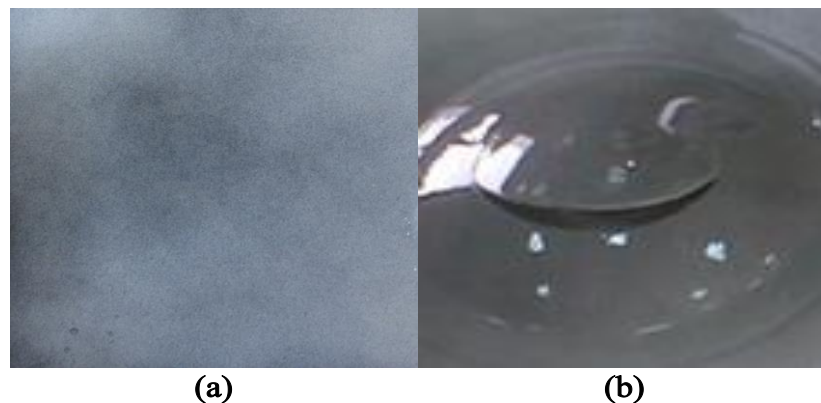
Figure 3.10 (a) the square test specimen with stochastic pattern (b) after HBT test the crack occurred on the top.

First, the sheet is put on the BUP 600 device and clamped between the upper and lower dies of the system from its flange areas. The drawbead helps the sheet to be formed

without excessive drawing by inducing tension. The specimen is formed by using hydraulic oil which provides the pressure. Meanwhile, the deformation of the sheet metal is recorded by Aramis system. While performing the operation the frame rate was 20 frames per second. The cameras recorded the images until the crack occurs (Figure 3.10). Besides, during the deformation, oil pressure is recorded with the load cells located under the hydraulic pistons. When crack occurs, the drawing operation is stopped and computation stage begins.

The measurement system provides the bulge radius by fitting a sphere before the burst stage, as shown in Figure 3.11. By fitting a sphere onto the deformed shape, flow curve of the material is calculated by using a code written in Matlab®. Finally, in HBT under biaxial stress state, up to true strain level of 1.0 could be reached.
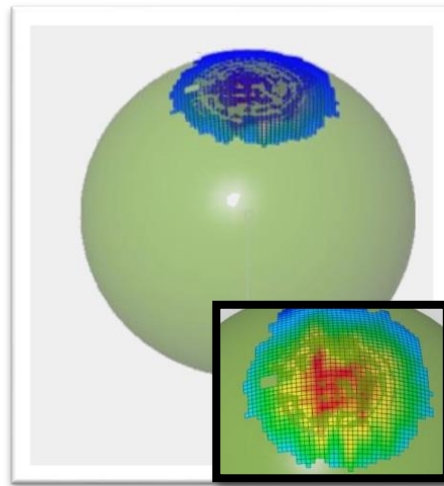
Figure 3.11 Aramis best fit sphere application to obtain the deformed specimen radius.
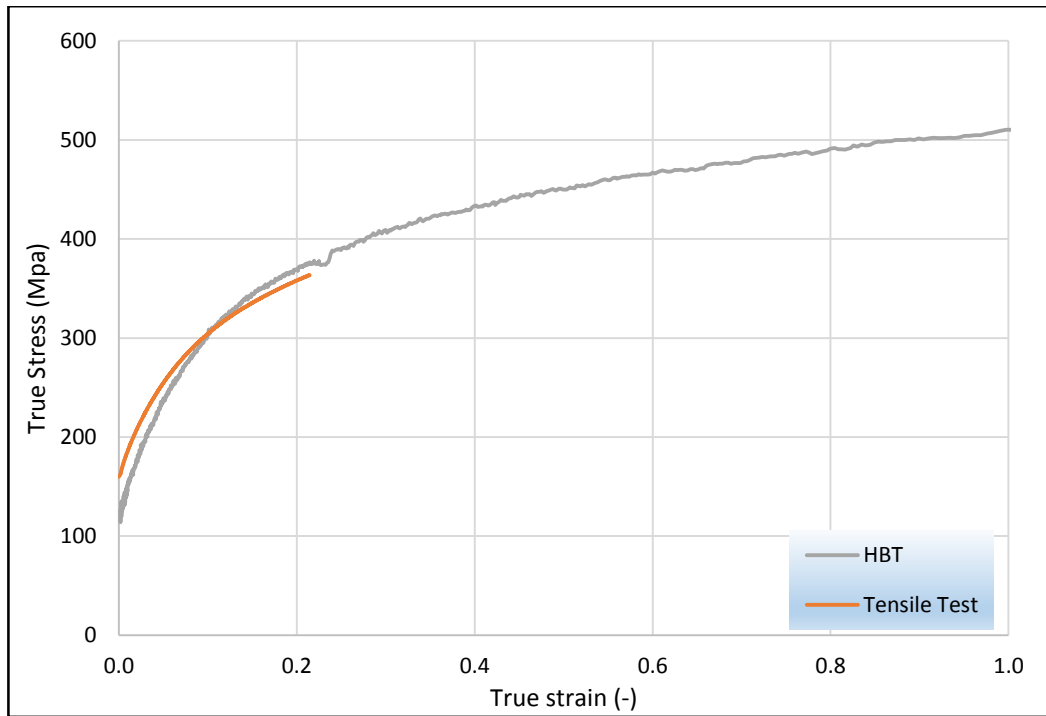
Figure 3.12 The flow curve which is obtained from HBT and tensile test.

As can be seen in Figure 3.12, the tensile test data reaches approximately 0.22 (up to diffused necking). It is obvious, when any extrapolation is applied to tensile flow curve up to 1 strain value, the curve follows different path from the HBT curve. In order to obtain the flow curve as well as providing accurate material behavior to FEA, the fitting operation is applied. Firstly, the tensile test data is taken up to 0.22 (since the tensile test trend up to diffused necking remains constant in rolling direction, even if the material is anisotropic) and the other part of the flow curve is taken from HBT flow curve. There is a transition region between tensile flow curve and HBT flow curve, which is irregular. Finally, a convenient curve, which is a combination of Hockett-Sherby and Ludwick-Hollomon models, is fitted by using MS Office Excel solver onto this curve.
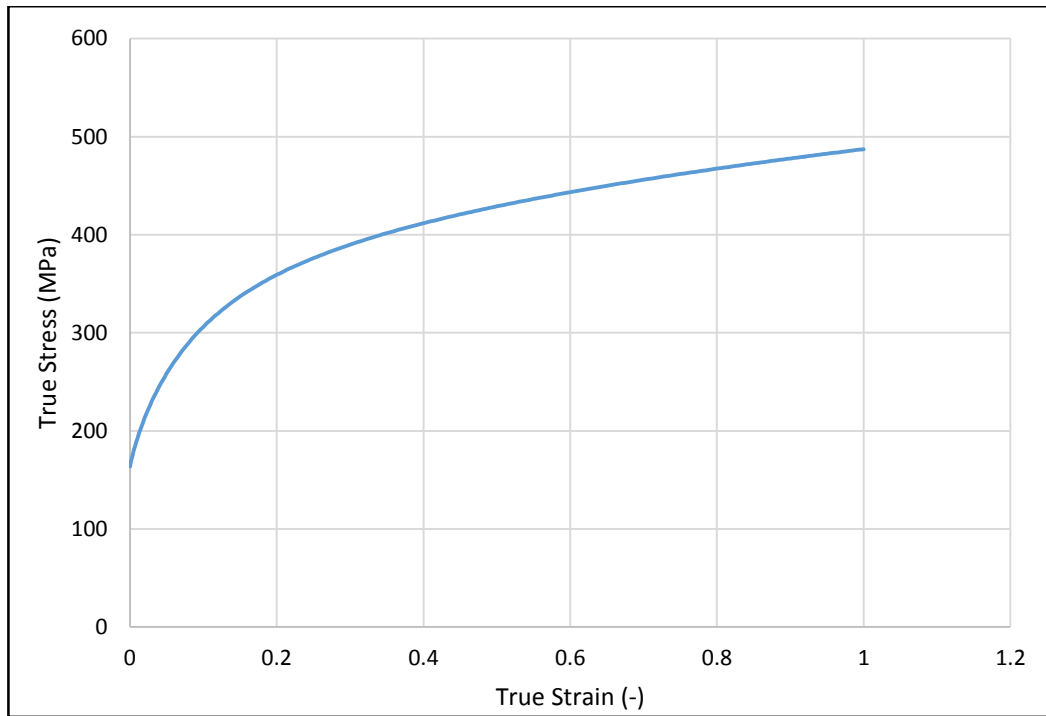
Figure 3.13 Flow curve obtained from the combinations of Ludwick-Hollomon and Hockett-Sherby material models.
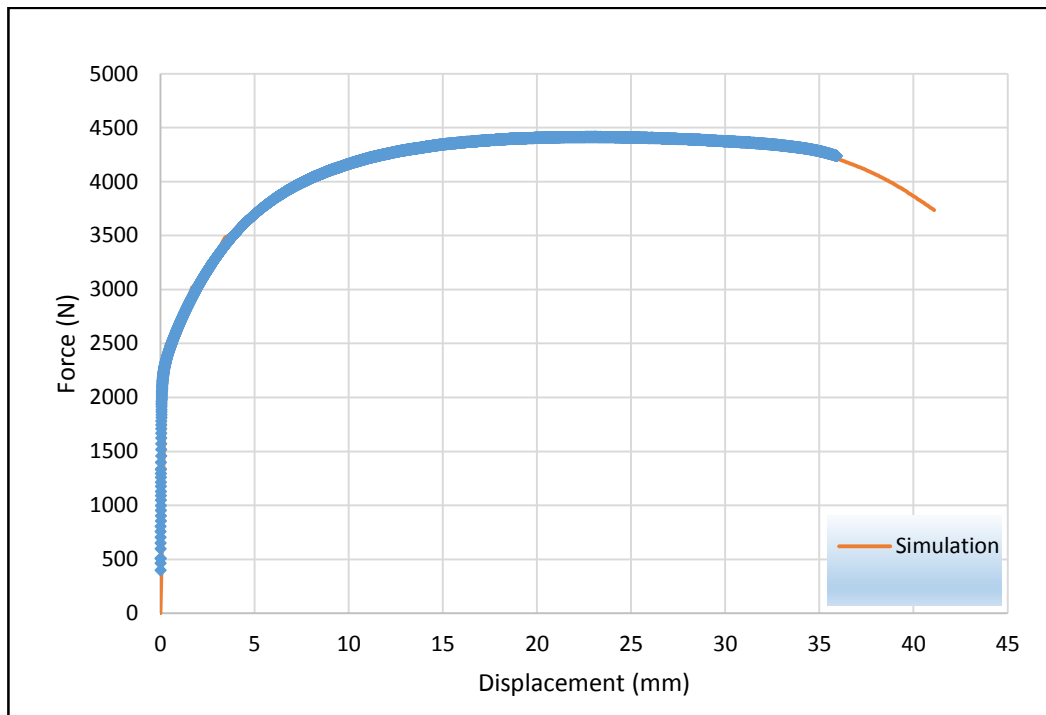
Figure 3.14 Force-displacement of FEA and uniaxial tension test data.

With the aim of obtaining accurate flow curve for numerical modeling, this curve is used in FEA software as a material model in order to obtain force-displacement curve of a uniaxial tension test.

Later, the obtained force-displacement curve is compared with experimental curve and the fitting parameters of the combined model are tuned until the two curves are almost coincident, see Figure 3.14. The actual flow curve obtained following this procedure is shown in Figure 3.15.
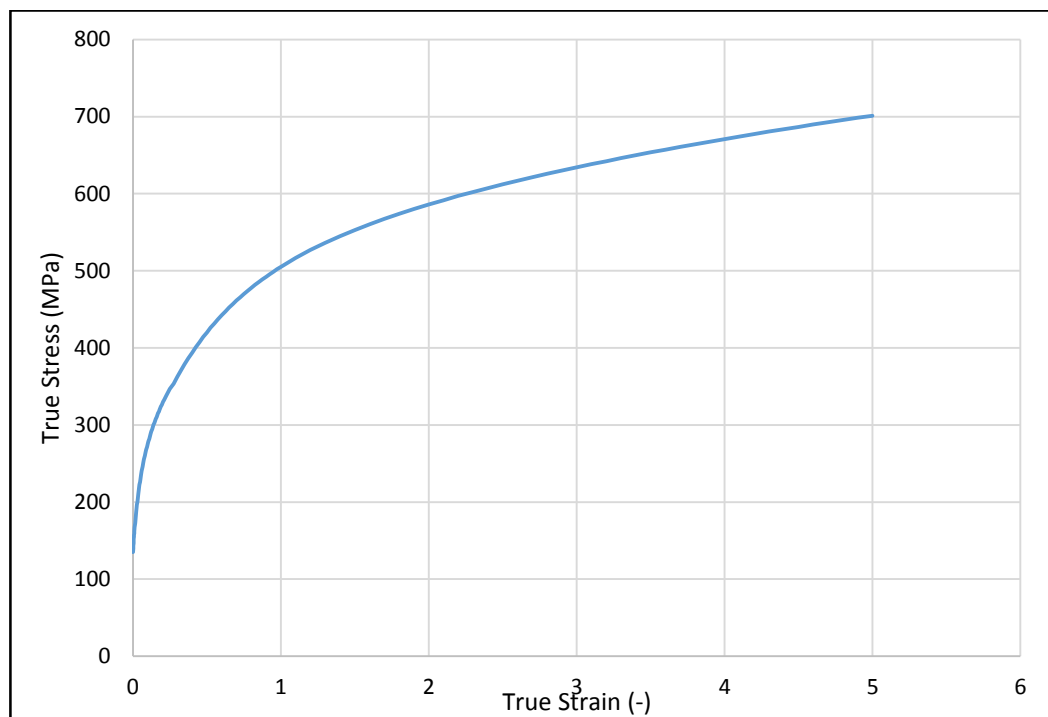
Figure 3.15 The flow curve used in FEA in this study.

3.2.4 Forming Limit Diagram (FLD) Test

Forming limit diagram indicates the principle strain values (ε_1, ε_2) measured at the onset of failure of thin sheets. The stochastic pattern created on the surface of the specimen is tracked during the deformation by the optical measuring system as in HBT and principle strain values are calculated.
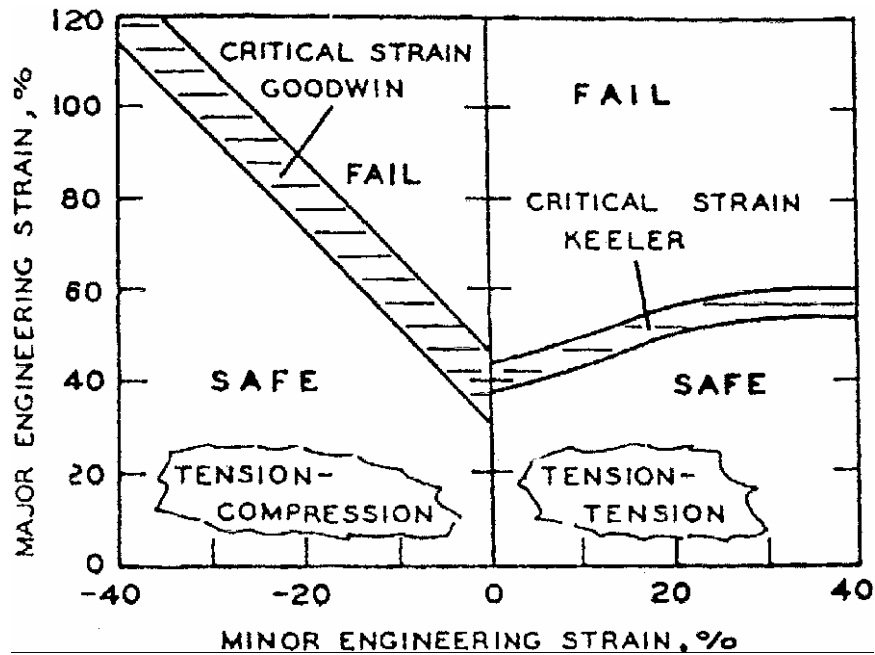
Figure 3.16 Forming limit diagram of Keeler and Goodwin [40].

The researches in this field was settled by Keeler which is based on the previous work of Gensamer [41]. Keeler was first plotted the major strain versus minor strain graph after the deformation of circles into ellipses at fracture in biaxial condition. Later, Goodwin [41] plotted the curve for tension/compression domain by different mechanical tests.

Generally, the diagrams of Keeler (right) and Goodwin (left) are called as the forming limit diagram, see Figure 3.16. As can be seen in the figure, if one exceeds the solid curve, then the condition is called 'fail', if one stays below this curve then it is called 'safe' region. In the figure, a vertical axis can be seen, which is located in the intersection of Keeler and Goodwin graph and represents the plain strain deformation in which $\varepsilon_2 = 0$. The location of this point on this axis has an important role because the position can be changed by strain hardening coefficient and thickness [34]. In order to determine FLD, one needs ε_1 and ε_2 values ranging from biaxial tension to pure shear ($\varepsilon_1 = -\varepsilon_2$).

Figure 3.17 Deformed Nakazima test geometries.

In this study, Nakazima test are performed to obtain the forming limits. The aim is to show that despite the ISF process reaches higher strain values and exceeds traditional forming limit curve, there is no tearing on the manufactured parts. Generally, Nakazima test consists of different geometries, circular die and hemispherical punch. The test geometries are prepared from 200x200 mm square sheet by cutting them at electric discharge machine (EDM). The shape of the specimen is provided by ISO12004 standard ('Metallic Materials. Determination of the forming limits') [34]. Additionally, the best solution for decreasing the friction between the sheet and the punch, the paraffin is used for lubrication.

Measurement procedure is briefly given in Figure 3.18. First of all, the cameras recorded the instantaneous deformation. After the crack occurs the recording is finished and the system starts to observe the deformation of the specimen through the images by using facets (a layer). The facet is applied both right and left camera individually for the computation. Then, a start point is created on the facet. With the help of this point, one can observe the deformation in each image. It should be noted that this procedure is same as in HBT test. Finally, the computation of strain data is executed and afterwards forming limit curve can be calculated.
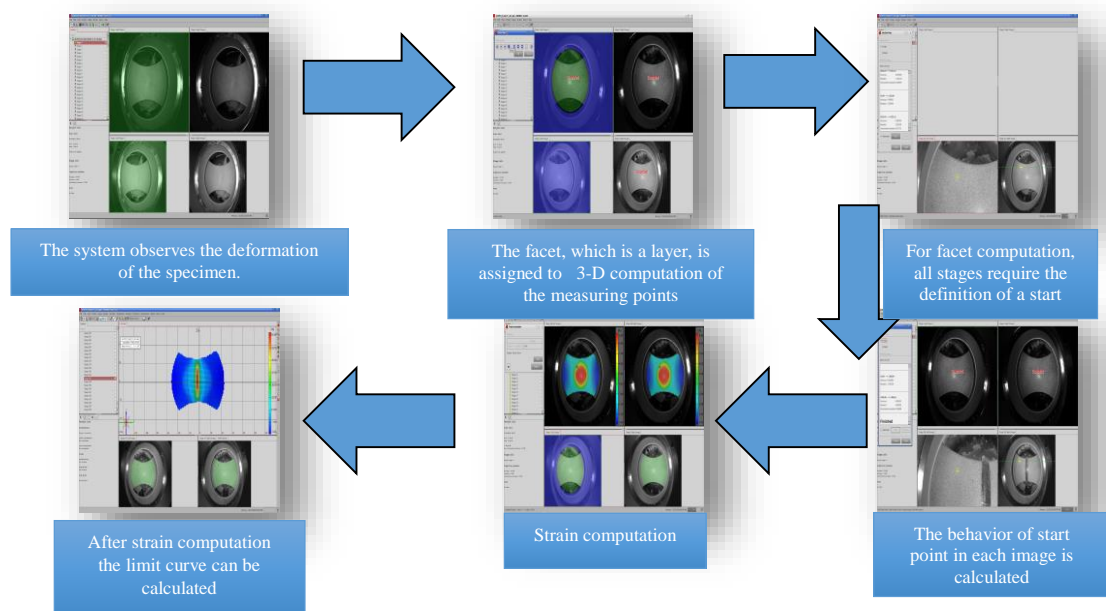
Figure 3.18 The computation process of deformation analysis.

For a good measurement, a specimen should satisfy the following conditions:

- The surface has an accurate pattern in order to assign the pixels in the camera images.

- The pattern should be able to follow the deformation of the specimen, which means the layer of the painting should stand on the sheet until the crack occurs.
- The pattern should not be reflective since reflections cause brightness differences and prevents facet computation.

The FLD test is performed by applying circular grids or stochastic pattern. The limit diagram can be influenced by the diameter of the circular grids or pattern. Moreover, the orientation of the specimen with respect to rolling direction, the lubricant, the thickness of the sheet, deformation history and the strain rate influence the FLD [41]. The surface strain can be measured by comparing stochastic or grid patterns starting from initial state to deformed state. The surface strains are calculated from the measured lengths of the major and minor axis, d_1 and d_2, see Figure 3.19.

In general, if the deformation behavior of a sheet metal is observed, the failure happens when a sharp local necking begins [42]. Sometimes localized necking can be confused with diffused necking. In diffused necking the load reaches to the maximum value and then instability occurs [43]. Additionally, a contraction occurs in both the lateral and width directions (the shortening of both width and thickness when $\varepsilon_1 = n$ [42]). On the contrary to diffused necking, in localized necking a groove arises in the middle of the diffused neck. Also, the specimen gets thinner without any change in width.
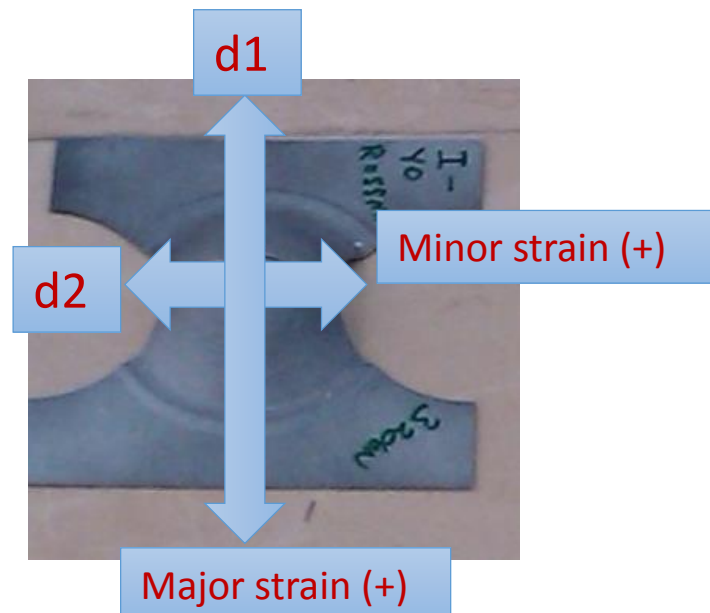
Figure 3.19 The directions of major and minor strains in a deformed specimen.
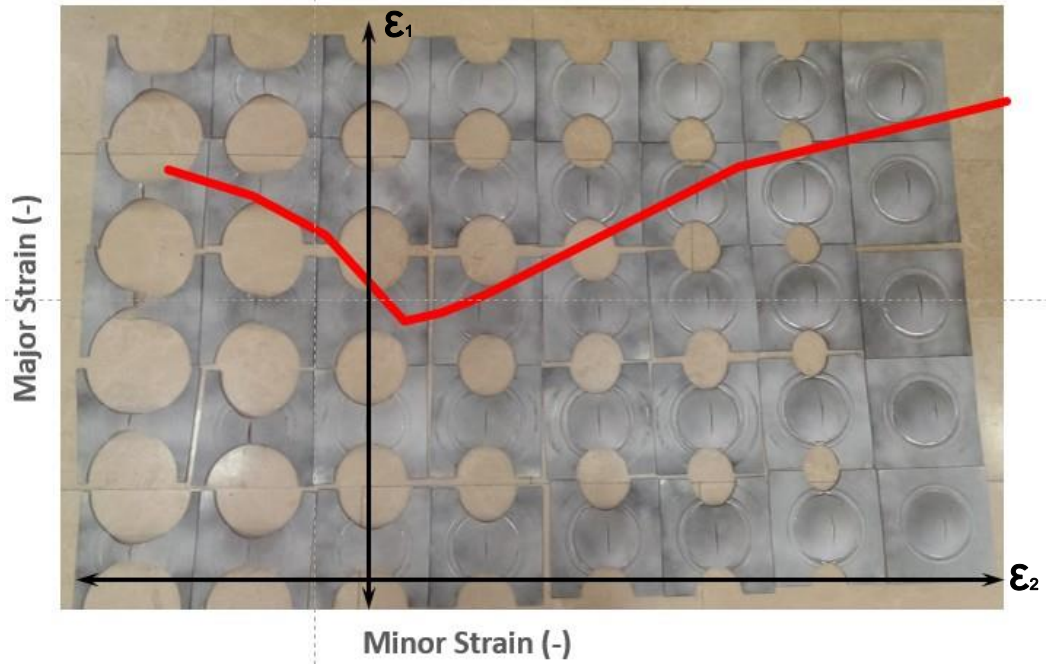
Figure 3.20 The deformed specimens with 8 different geometries.

The strains are plotted to principle strain space in order to obtain the yield locus at any stage of forming operation. The yield locus expands due to continuation of the deformation, then the grids on the sheet outer surface reach to the maximum deformation limits. Therefore, the strain diagram is created. As can be seen in Figure 3.20, a general limit diagram obtained from Nakazima tests is presented. Once, the major and minor strains are measured then the calculation of the forming limit diagram is as follows:

- Firstly the principle strains ε_1, ε_2 and ε_3 are calculated
- Then, the strain ratio is calculated which is

$$\beta = \frac{\varepsilon_2}{\varepsilon_1}$$

Eq.3.24

- Finally the thickness is calculated

$$\varepsilon_3 = ln\frac{t}{t_0} = -(1+\beta)\varepsilon_1 = -(1+\beta)ln\frac{d_1}{d_0}$$

Eq.3.25

$$t = t_0 \exp(\varepsilon_3) = t_0 \exp\left[-(1+\beta)\varepsilon_1\right]$$

Eq.3.26

Hence, the modes of deformation can be described after the calculation of points which is explained in above. As can be seen in Figure 3.21, there are 5 deformation zones which will be discussed in the following:

33

- Region-1 indicates the equibiaxial tension or stretching in which the strain ratio is 1. Here the sheet is stretched and the deformation occurs in the center. The membrane strains are equal in all directions. The grid circle gets larger as iso-circle. The thickness gets lower more quickly and the n-value increases rapidly with respect to ε_1,
- Region-2 indicates plane strain tension zone. The sheet deforms only in one direction. The strain ratio is 0,
- Region-3 indicates the uniaxial tension. The strain ratio is -1/2. This is the strain state of the uniaxial tension. The sheet deforms in one direction and contracts in the other direction,
- Region-4 indicates pure shear. The membrane stresses and strains are equal and opposite. The thickness doesn't change. The strain ratio is -1. It occurs in the flange of a deep drawn cup,
- Region-5 indicates the uniaxial compression zone in which the strain ratio is -2. Here, the minor stresses are compressive. The sheet thickens, since the effective strain and stress is negative.
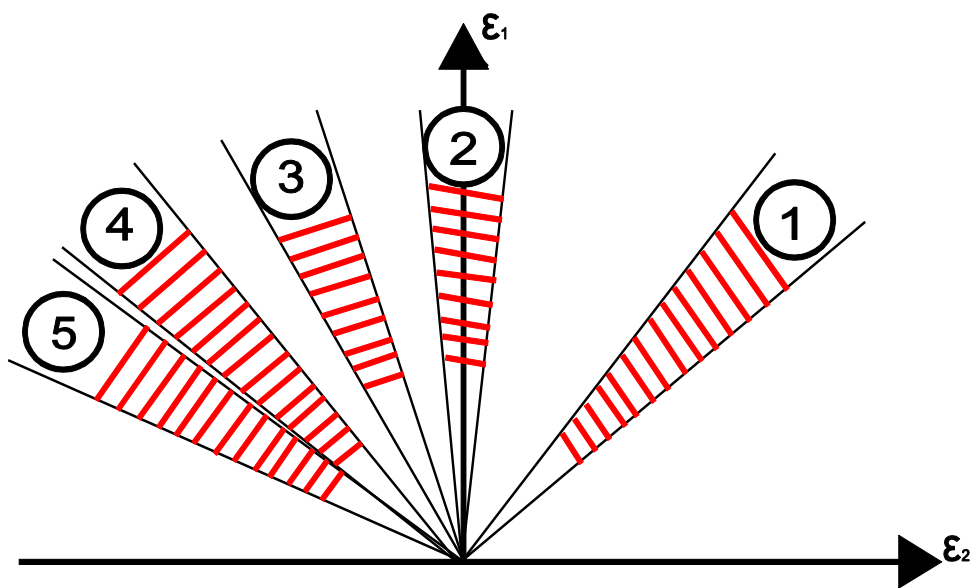
Figure 3.21 Strain diagram with 5 different zones.

Thinning and thickening can be identified by looking at the strain ratio. If the ratio is greater than -1 then thinning occurs. If it is lower than -1, the thickening happens and wrinkling would arise.

Forming Limit Diagram test is standardized by ISO 12004-2 'Metallic Materials – Sheet and strip – Determination of forming limit curves' [34]. As in HBT, the measurements are performed in 600 kg-f capacity Zwick/BUP600 machine integrated with GOM/Aramis optical deformation measurement system.
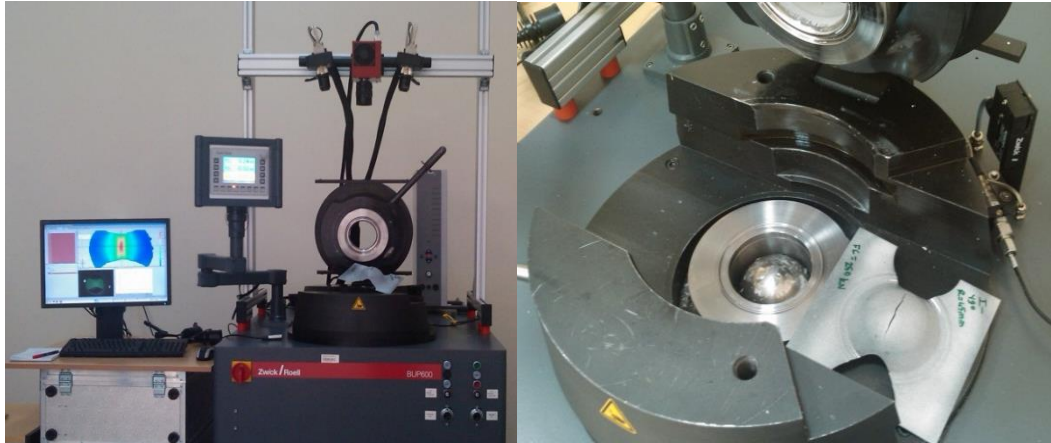
Figure 3.22 Experimental setup of FLD test.

In order to obtain FLD, at least 5 different geometries with 3 repetitions should be conducted [44]. In this study, 8 different geometries with 3 repetitions are carried out. Figure 3.23 illustrates the deformed sheets.
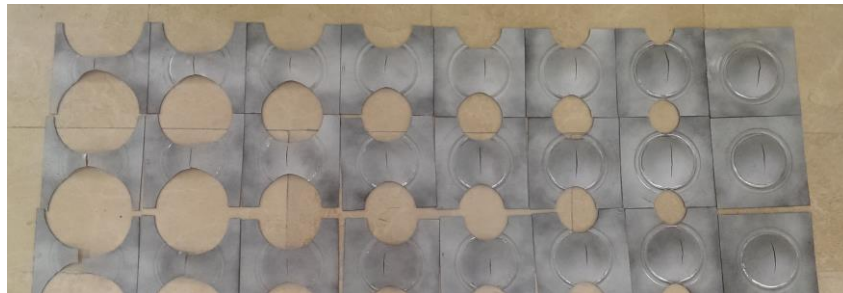
Figure 3.23 The deformed specimens after Nakazima test.

For the FLC calculation 3 sections are executed for each geometry and repetition (Figure 3.24).
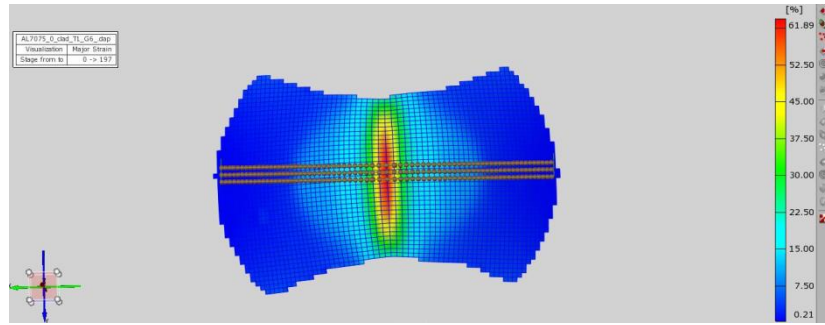
Figure 3.24 Aramis 3D strain data with 3 sections.

The results of 3 repetitions are given below:
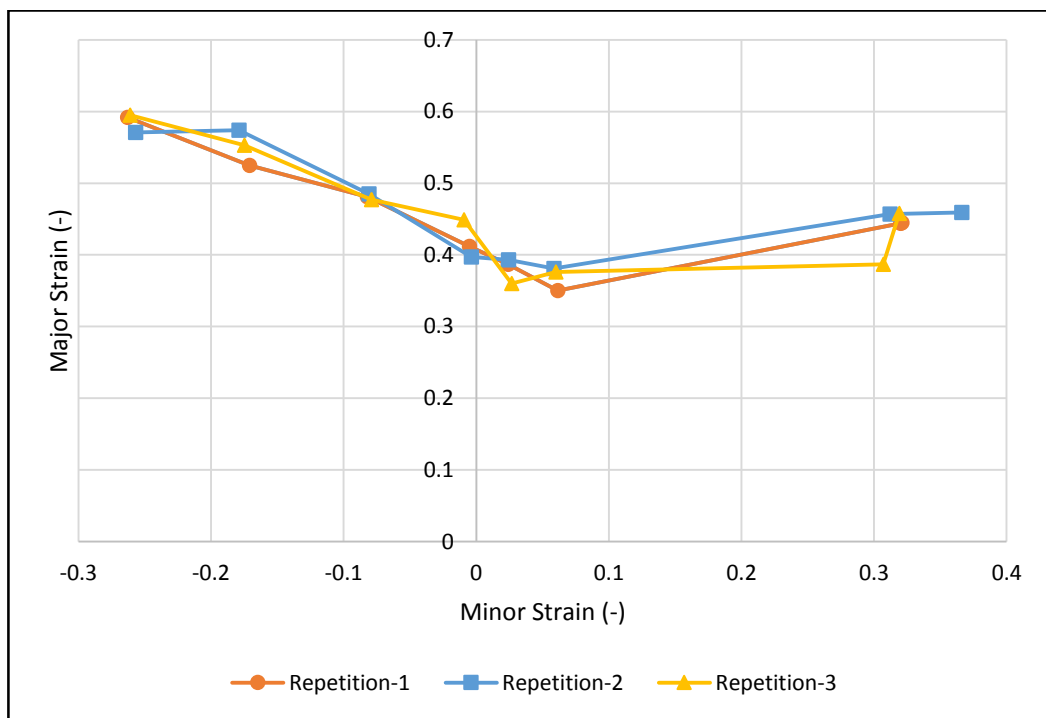
Figure 3.25 Forming limit diagram of FEP04 with 3 repetitions.

3.3 Numerical Modelling

3.3.1 Introduction

Finite element method (FEM) is an approach to solve physical problems in engineering, which are described in terms of partial differential equations, such as stress analysis or heat transfer [45]. Classical methods, for instance analytical methods, is inadequate to solve partial differential equations on complicated geometries.

36

The use of FEA provides a rapid and less expensive solution to evaluate the design of experiments and their details. In general, for metal forming operations two basic approaches are conceivable for the formulation and solution of the governing equations which are the implicit and explicit methods. These methods are briefly introduced in the following subsections.

3.3.2 Explicit Method

In explicit methods, the dynamic equilibrium equations are enforced at the beginning of the time step and expressed as,

$$Ma^n = f^n = f^{ext}\left(d^n, t^n\right) - f^{int}\left(d^n, t^n\right)$$
Eq.3.27

where, a^n is the acceleration, d^n is the displacement and n is the time step, respectively. Discretization in time is done by using the central difference method which yields the following formulas

$$v^{n+1/2} = \frac{d^{n+1} - d^n}{t^{n+1} - t^n}$$
$$= \frac{d^{n+1} - d^n}{\Delta t^{n+1/2}} : Velocity\ Formula$$
Eq. 3.28

$$a^n = \frac{v^{n+1/2} - v^{n-1/2}}{t^{n+1/2} - t^{n-1/2}} = \frac{(d^{n+1} - 2d^n + d^{n-1})}{(\Delta t^n)^2}$$
$$: Acceleration\ Formula$$
Eq. 3.29

for velocity and acceleration, respectively. Using these relations, the system of equations to be solved can be put in the following form

$$a^n = M^{-1} f^n$$
Eq.3.30

where, M is the mass matrix. Once a^n is determined, the velocities and unknown displacements d^{n+1} can be updated.

In order to get an efficient solution algorithm, the consistent mass matrix is diagonalized using the row-sum technique.

$$M_{IJ}^D = \sum_J M_{IJ}^C$$
Eq.3.31

37

resulting in the lumped mass matrix M_{IJ}^D. Since the off-diagonals of lumped mass matrix are zero, solution of Eq.3.30 does not require a matrix inversion and can be done in a straight forward manner.

The major drawback of explicit methods is their conditional stability which imposes a limitation on the maximum time step size can be used. Δt has to be smaller than,

$$\Delta t_{critical} < \frac{l_e}{c_e} \qquad \text{Eq.3.32}$$

where, l_e is a characteristic length of element e and c_e is the wave speed. The critical time step decreases with mesh refinement and increasing stiffness of the material. If the time step exceeds the critical time step, instability will occur. Instabilities can lead to exponential growth of the solution or a large overprediction of displacements [46].

The instabilities can be monitored by an energy balance check. However, when a model has a few stiff elements, the solution will grow unboundedly. Because the critical time step of the entire mesh is set by these stiff elements. In order to solve this problem, mass scaling technique is used. In this technique, the masses of stiff elements are increased, thus the time step is not decreased.

In the context of ISF, Bambach et al. [47] have mentioned that the ratio of total kinetic energy and total internal energy should stay below 5%. An important issue turned out to be the non-smooth tool path which creates local jump in the acceleration and velocity. It was concluded that, the jumps could be controlled through a velocity based description of the tool path trajectory and a suitable choice of mass scaling.

3.3.3 Implicit Method

In implicit methods, the equilibrium equations are enforced at the end of the time step and expressed as;

$$r\left(d^{n+1}, t^{n+1}\right) = f^{int}\left(d^{n+1}, t^{n+1}\right) - f^{ext}\left(d^{n+1}, t^{n+1}\right) \qquad \text{Eq.3.33}$$

where, $r(d^{n+1}, t^{n+1})$ is the residual forces. As seen from Eq.3.38, the inertia term is neglected for ISF process considered in this thesis.

The solution of Eq.3.33 is obtained generally by the Newton-Raphson method which requires the consistent linearization of the non-linear equation set Eq.3.33. In a general form, the linearized equations can be written as,

$$r \mid_k + \frac{\partial r}{\partial k} \mid_k \delta u = 0 \qquad \text{Eq.3.34}$$

$$r \mid_k + K \mid_k \delta u = 0 \qquad \text{Eq.3.35}$$

where, k is the iteration counter of the Newton-Raphson solution procedure and K is the consistent tangent matrix. Upon the solution of this system, the unknown displacements are updated

$$d^{n+1} \mid_{k+1} = d^{n+1} \mid_k + \delta u \qquad \text{Eq.3.36}$$

and the iteration process is continued until a convergence criteria is fulfilled.

The advantage of an implicit method over an explicit method is that, this method is unconditionally stable. The major restriction on the time step size in implicit methods stems from accuracy requirement and decreasing robustness of the Newton's procedure when the time step increases.

There are several studies in ISF process related with implicit analysis. In Hadoush et al. [48], it was mentioned that the standard implicit time integration scheme is inefficient because of Newton-Raphson strategy for the whole system of equations. The recommendation was to use iterative update for strong nonlinear parts. In order to do this, the mesh was split into two domains, in which the first domain models the strong nonlinearity part and the second domain models the elastically deformed zone. As a conclusion, the two domain method reduced the overall computing time of implicit analysis. This method with 6400 shell elements speeded up the implicit analysis by a factor of 2.42 with a geometric deviation less than 40 microns.

Another study of Hadoush et al [49] involves the reduction of the computational time in the implicit simulation of ISF by using the direct substructuring method. It was divided into two groups which were the plastic nonlinear substructure and the elastic-pseudo-linear substructures. The first group described the plastic zone which occurred between the vicinity of the tool and finite element mesh. The second modeled the elastic deformation of the rest of the mesh which has linearized and condensed

linearized approaches. As a result, the methods reduces the computing time as compared to standard solution techniques.

Eyckens et al. [50] have tried a new approach, in which only a small part of unclamped sheet is considered in finite element model. They have used much finer mesh. The finite element submodelling technique allowed the boundary conditions on the edges of the model to be physically meaningful. Four different ISF processes are modelled. Each of them were simulated with 3 implicit finite element models at different scales. In all cases, the sheet is modeled as several layers of linear brick elements. As a result, the finite element submodelling was used for improving the plastic deformation zone modeling.

3.3.4 Finite Element Modeling

In this study, three different shapes at different depths and wall angles have been investigated. Those are truncated cones, square pyramids and a real car component, respectively. Both implicit and explicit analyses have been carried out using the commercial FE software Abaqus®.

Two parts are drawn for modelling, the blank and the indenter. The blank with an initial thickness of 0.8 mm is discretized by shell elements. The element type is S4R which is a 4-node, quadrilateral, conventional shell element (has displacement and rotational degrees of freedom and discretizes the blank by defining the geometry at a reference surface) with reduced integration [51]. The S4R element is used instead solid elements with the aim of decreasing the computational time [52]. Also, the S4R element uses a reduced integration rule with one integration point which makes the element computationally less expensive than S4 element [53]. The number of the integration points through the thickness is 7. In Table 3.3, the simulation parameters are given for all investigated parts including the number of elements for each part.

	Element Type	Element Number	Integration Points Through the Thickness	Element Integration
Truncated Cone	S4R	~6000	7	Reduced
Truncated Square Pyramid	S4R	~7300	7	Reduced
Real Car Component	S4R	~10200	7	Reduced

Table 3.1 The simulation parameters of ISF process.

The meshes are illustrated in Figure 3.32. As can be seen in the figure, fine meshes are used in the contact area where the high localized deformation occurs. The approximate element size is 2 mm at fine mesh region. The inner and outer part of truncated cone have an approximate mesh size of 20 mm. However, the other shapes have 15 mm element size. Further, the blank is modelled as a rate independent isotropic elasto-plastic material.

In all of the analyses, the tool is assumed to be rigid. The contact between the blank and the tool is assumed to be frictionless and the impenetrability constraint is enforced by the penalty method. In implicit analysis, an adaptive time stepping is used and in explicit analysis mass scaling technique is activated. Mass scaling is applied to whole model at the beginning of the step and the scale factor is 10. The linear and quadratic bulk viscosity parameter are 0.06 and 1.2, respectively. The density of the material is 7.8 tone/mm^3. Mass scaling is used to constitute a nonphysical mass to element's structure in order to adjust the time step with the aim of controlling the numerical stability. Increasing the mass causes to lower the frequency of the problem, thus it increases the time step. The advantage of the mass scaling is if the appropriate parameters are used, then the computational time will be lowered and accurate results will be obtained.

The material behavior has been supplied from calculated flow curve in subsection 3.2.3. The Young's modulus was taken to be 190000 MPa which was experimentally calculated in [54]. The Poisson's ratio was taken to be 0.3.
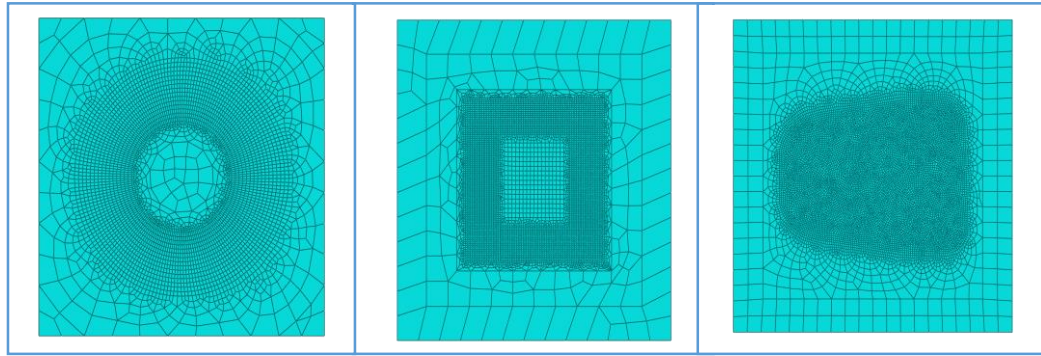
Figure 3.26 The mesh description for manufactured parts in FEA.

As can be seen in Figure 3.26, fine mesh is assigned in the middle part of the blank, whereby the deformation occurs in the vicinity of the tool and blank in the middle. In Figure 3.27, the model of ISF process, before and after the deformation, is given.

(a)   (b)
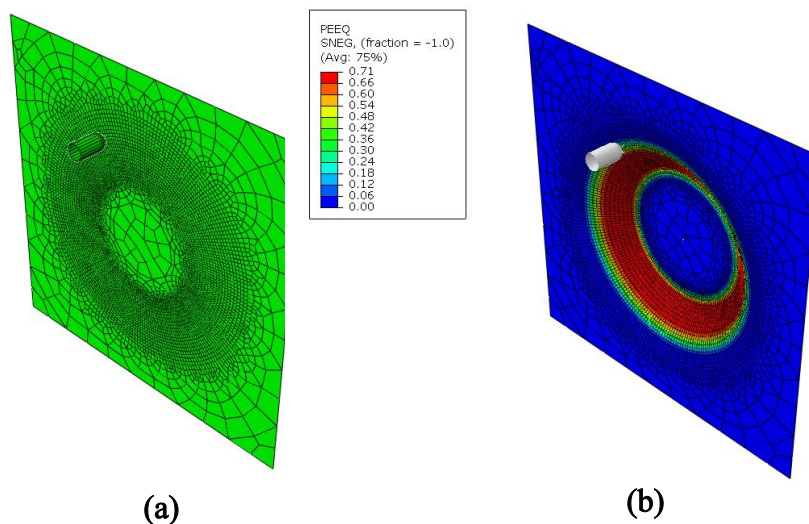
Figure 3.27 The ISF model, (a) before deformation, (b) after deformation with plastic equivalent strain results.

The analysis results are assessed and compared with experimental measurements in the next chapter.

CHAPTER 4

EXPERIMENTAL STUDY

4.1 Experimental Setup of ISF

4.1.1 Introduction

In this study, all the parts are manufactured on 3-axes CNC milling machine which has a FANUC controller system. Experiments were carried out by using 3 different backing plates as shown in Figure 4.1.
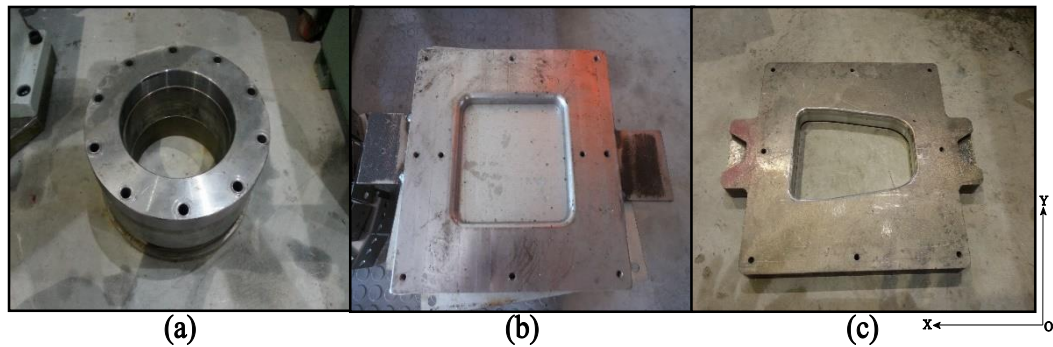
Figure 4.1 The backing plates used in manufacturing of workpieces, (a) used for truncated cones, (b) used for pyramidal shapes and (c) used for real car component.

The circular backing plate has 242 mm outer and 151 mm inner diameter. In addition to this, the square backing plate has 254 mm x 254 mm working area. The real car component's backing plate has an asymmetric working area which has a maximum length of 193.7 mm in X direction and 139.8 mm in Y direction.

The blanks, used in manufacturing truncated cones on circular backing plate, have a square shape in which the dimensions are 200 mm x 200 mm with the thickness of 0.8

mm. The square and asymmetric backing plates are employed to manufacture pyramidal shape and the real car component which have the dimension of 300 mm x 300 mm x 0.8 mm. Further, the spherical ended tools, while manufacturing the desired shapes, are carbide tools which have diameters of 5 mm, 10mm and 15 mm, respectively.

Figure 4.2 The different diameter of the spherical tool tips which are used for manufacturing the parts in a general ISF process.

It is worth mentioning that the metal frame, which is a significant component of ISF setup, clamps the blank onto the backing plate in order to avoid the sliding of the sheet over the backing plate while forming.

The tool paths are generated in commercial CAM software program Hypermill® in which the CAD data obtained from commercial software CATIA V5R19®. It is worth pointing out that the tool path design has an important role to manufacture the complicated parts as compared to manufacturing the simple parts which have lower drawing angles. In order to manufacture complicated shapes, having greater than 70^0 wall angle, the multi-stage tool path strategy is necessary. In the following section, detailed literature survey will be given.

4.1.2 Tool Path Design

ISF has an enhanced forming technology and great flexibility, thus the tool path design becomes more important. The tool path efficiency provides maximum formability to complex parts with a good surface finish and dimensional accuracy.

The tool path algorithms which are z-level finishing and equidistant finishing strategies are mostly used in this study. In z-level finishing algorithm, the spiral tool path is used, in which there are two types of vertical infeed modes describing the tool's movement. The first one is constant step down which allows to adjust step size by smaller value to higher values. The second one is scallop height, in which the step width between the tool paths depends on the surface curvature and steepness [55]. Moreover, the complete z-level is taken into consideration and the smallest value is calculated to determine step width. Additionally, the infeed strategy, provided by the equidistant finishing algorithm, is flowing between two selected profiles of desired part. The step width is calculated automatically using surface of the part.

In literature, there are several studies on tool path design and optimization as mentioned before. They are related to decreasing springback, on the contrary, increasing dimensional accuracy or surface quality by using most convenient tool path strategy. Also, some of the studies are related to how to avoid tearing. In addition to tearing issue, the tool path strategy is a significant point to form the steep walls for complicated and asymmetric shapes.

In Skjoedt et al. [56] study, it was mentioned that for complicated parts in which the part consists of 90^0 wall angle, it is not allowed to manufacture that part by using one step strategy. They have also pointed out that Kitazawa et al. [57] used two step strategy for manufacturing hemi-ellipsoidal shape. Their study involved the forming cups which have a 90^0 drawing angle. The experiment had two different tool path steps which are down-up-down-down (D-U-D-D) and down-down-down-up (D-D-D-U). They were succeeded to use D-D-D-U strategy (Figure 4.3). On the contrary to this strategy, they have failed at fourth stage while using D-U-D-D strategy. As can be seen in Figure 4.3, the crack has occurred due to the heavier thinning conditions in the direction of thickness strain.

(a)	(b)

Figure 4.3 (a) The manufactured part with the achievement of D-D-D-U strategy and (b) is the failed part [56].

Another study on ISF was performed by Duflou et al. [58]. They have investigated the manufacturing of solar cooker and a cranial plate which is used for reconstructive skull surgery. Firstly, a single pass procedure was used which was a contouring strategy. There was a lot of springback at the side walls in final product. Afterwards, they have used two steps, in which the first step includes the manufacturing the part to an arbitrary stage and the second step includes the final stage of desired shape. Hence, they had an accurate shape. Additionally, they have applied the same procedures for manufacturing of cranial plate. As a result, they have achieved to capture the accurate shapes. In Duflou's [58] study, it was mentioned about several tool path strategies which were used for obtaining accurate parts in terms of geometric tolerances. These strategies have been compared and it was concluded that for cylindrical or spherical shapes, which had steeper walls, after preforming it was better to use vertical infeed as spiral finishing. However, for square pyramidal shapes, it was better to use scallop height.

Figure 4.4 Manufactured real car component with tear.

Ambrogio et al. [59] pointed out that the accuracy of the manufactured part depends on step size and the tool diameter. Since the step size increases, the thinning reaches to higher values due to the stretching in the movement direction of the tool. The blank was deformed under heavier condition and tearing occurred at the end. As in Figure 4.4, the blank is torn, using larger step widths.

Generally, a complicated shape can be manufactured by using multi-stage tool path design. In multi-stage design, the blank is formed to a pre-shape, later the other shapes are formed and the final geometry is obtained. According to the study of Bambach et al. [24], it was possible to improve the dimensional accuracy of the final shape by using multi-stage tool path. They have pointed out that the sheet was exposed to the tool pushing and the total deformation occurs which depends on elastic recovery. Hence, when the part is formed only by one tool path stage, the large deformation occurs in the vicinity of the tool and the blank and the sheet has a crack. By using multi-stage tool path strategy, since the total deformation is smaller as compared to one tool path stage, the part could be manufactured. Moreover, if the transition from the initial tool path stage to the second is larger than the tool diameter, the blank may also be torn as in Figure 4.5 (a).

(a)   (b)
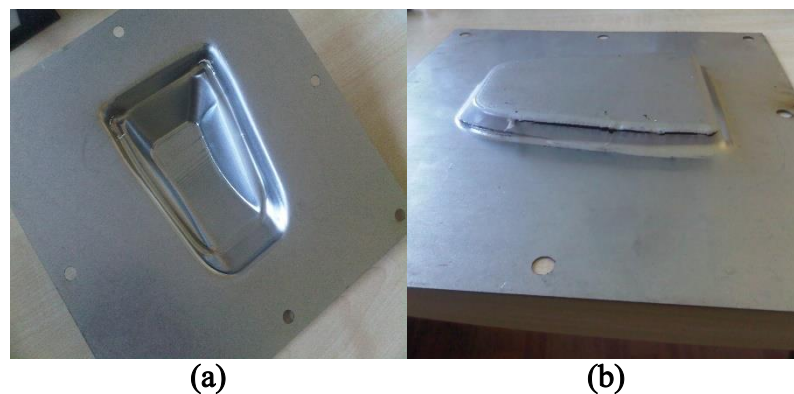
Figure 4.5 Different trials for manufacturing of real car component, (a) is multistage forming and (b) is single stage with larger step sizes.

There is another subject which was mentioned before, having a significant role in ISF, is the forming limits. Hirt et al. [60] pointed out that the forming limits can be overcome by using multi-stage tool path strategy. Also, in that study it was pointed out there are several studies on this strategy which has been developed for asymmetric

parts which have steep walls. Additionally, it has been tested by manufacturing a pyramidal shape which has an 81^0 draw angle.

4.1.3 The Experiments

The experiments have been carried in Metal Forming Center of Excellence (MFCE). At the very beginning of the trials, in order to investigate the geometrical accuracy, major-minor strain and thickness distribution, the blanks were gridded by using electrochemical etching device.
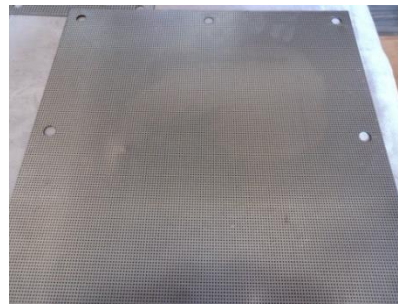
Figure 4.6 The etching is applied onto the blank in order to make deformation measurements after forming.

After etching procedure the sheet is mounted on backing plate and fixed with a metal frame. Figure 4.7 shows the ISF operation which is performed by using 10 mm carbide tool.

(a)   (b)
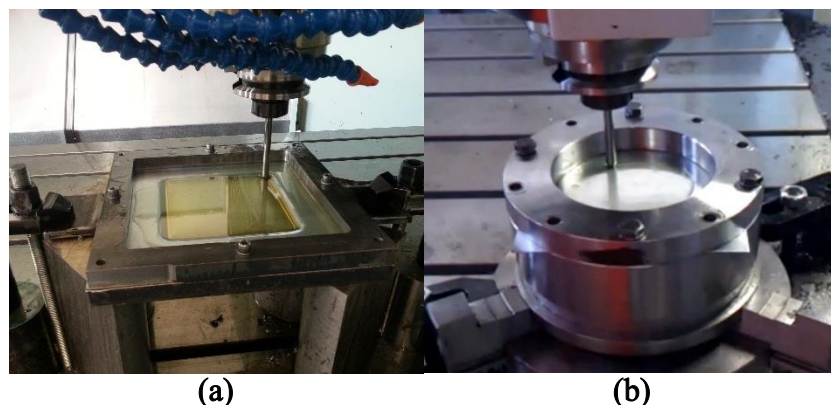
Figure 4.7 The ISF operation performed in MFCE with 10 mm diameter tool.

The tool path algorithm for truncated cones and square pyramids is spiral z-level finishing algorithm with constant step down infeed mode. The step width is 0.5 mm for both algorithms. After manufacturing simple parts, the experiments were

conducted and the results were compared with numerical results. It will be considered in Chapter-5 in detail.

Related to above instructions, firstly, three truncated cones are manufactured. In Figure 4.8 the tool path of a truncated cone is shown.

(a)   (b)

Figure 4.8 The illustration of tool path for truncated cone which has 40 mm depth with 60^0 wall angle, (a) is the upper view with tool path and (b) is only tool path view.

The depth of the cone is 40 mm with the initial process region of 128 mm. The angle between the flat surface and steep wall is 60^0. All the tool paths (for 5 mm, 10 mm and 15 mm tool) generated from CAM software and used as a boundary condition for FEA converting NC-codes into coordinate data by using commercial MATLAB program.

Figure 4.9 The formed parts in which 5 mm, 10 mm and 15 mm tools are used illustrated from left to right.

After manufacturing the truncated cones (Figure 4.9), the optical measurements are performed in order to obtain geometry and deformation behavior.

Another study is manufacturing the truncated square pyramids. Two different studies are performed. The first study involves truncated square pyramid having a depth of 60

mm with a wall angle of 60^0. The tool path is shown in Figure 4.10 and the formed truncated square pyramids are shown in Figure 4.11.

(a)   (b)
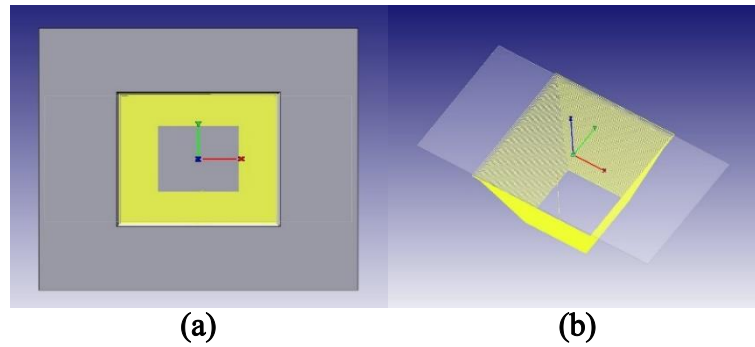
Figure 4.10 The illustration of tool path for truncated square pyramid which has 60 mm depth with 60^0 wall angle, (a) is the upper view with tool path and (b) is only tool path view.
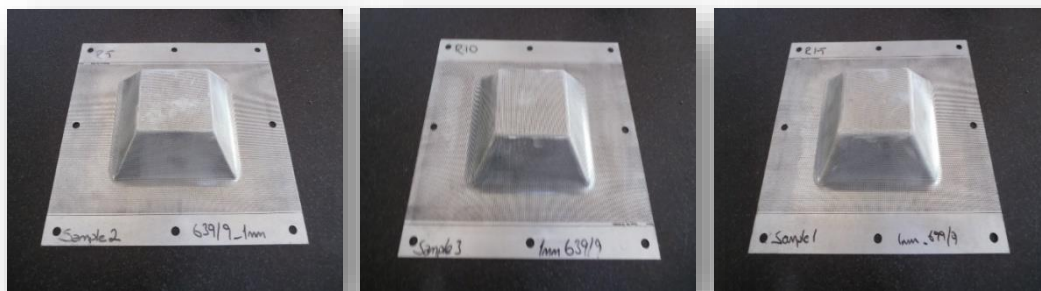
Figure 4.11 The formed parts in which 5 mm, 10 mm and 15 mm tools are used illustrated from left to right.

The other study is manufacturing relatively smaller part which has a depth of 20 mm with 10 mm diameter tool. The angle between the flat surface and the inclined wall is 40^0. The tool path algorithm is same as in truncated cones. In Figure 4.12 the tool path is shown.
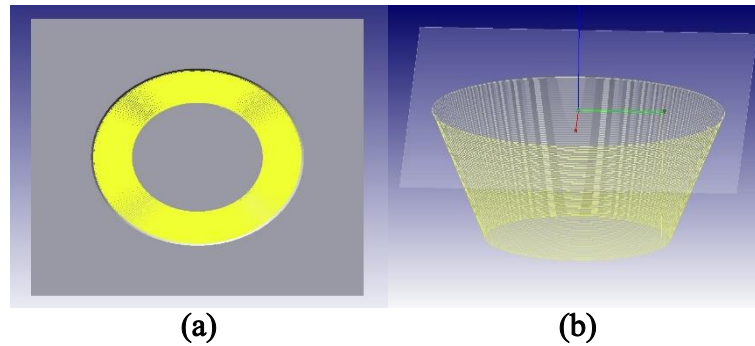
(a)   (b)
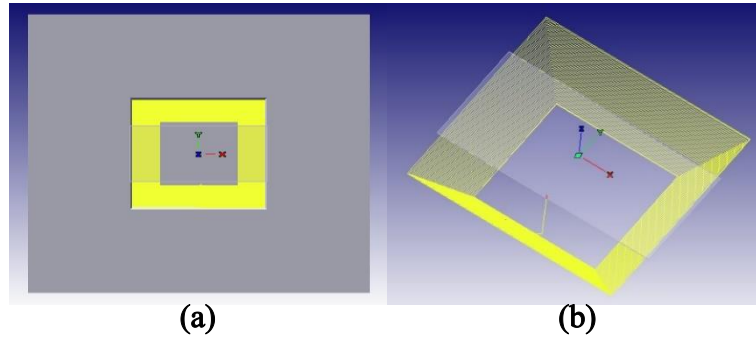
Figure 4.12 The illustration of tool path for truncated square pyramid which has 20 mm depth with 40^0 wall angle, (a) is the upper view with tool path and (b) is only tool path view.
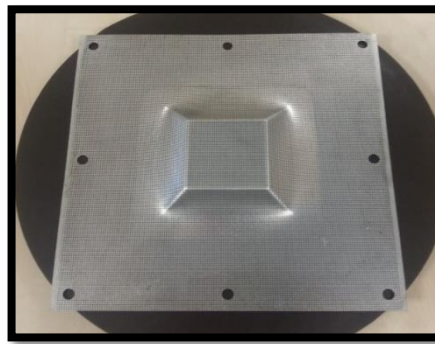
Figure 4.13 The deformed part with 10 mm diameter tool with grids.

Moreover, in order to investigate the geometric compatibility, the deformation behavior and the thickness distribution at different depths, 4 different truncated cones and square pyramids are manufactured by 10 mm diameter tool tip. The parts has the depth of 5 mm, 10 mm, 15 mm and 20 mm. Figure 4.14 demonstrates the truncated cones and square pyramids which were formed by spherical ended tool.
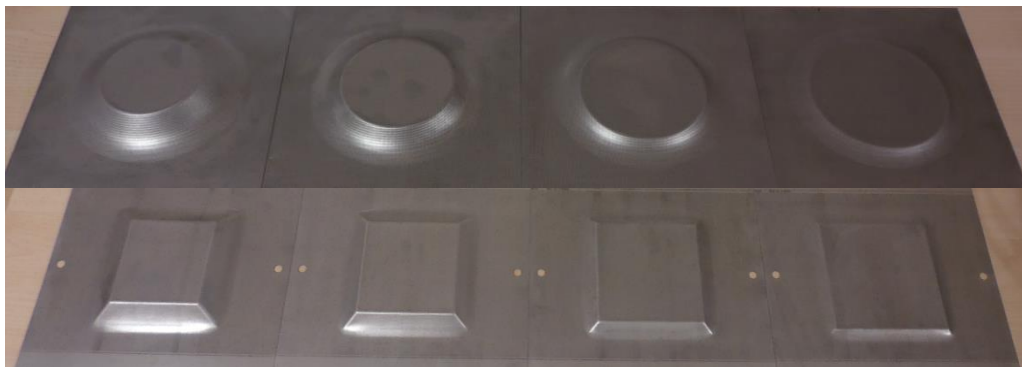
Figure 4.14 The formed parts with different depths manufactured by using 10 mm tool tip.

Up to now, the basic geometries are considered. It is obvious, manufacturing of the parts which have steep walls are impossible in one tool path stage due to deformation conditions.

The reasons for manufacturing these basic shapes can be explained as:

- to investigate the maximum limits of drawing angle for each part. Before deciding the shapes of the simple parts, several trials which has different geometries are conducted,
- to investigate the feasibility of manufacturing truncated cones and square pyramids at several depths with different wall angles,
- to compare the manufactured parts with their numerical analysis in terms of dimensional accuracy, deformation behavior and thickness,
- to determine which tool path algorithm is most convenient to use in manufacturing a complicated part.

Based on the results presented in the previous discussions, it was concluded that explicit FE models can be applied for final geometry prediction in ISF, due to its consistency with experimental results. In order to assess the potential use of explicit FE for tool path optimization and to investigate different multi-stage tool path strategies in ISF process, manufacturing of a Fiat Doblò part "Staffa Reazione Funi Freno a Mano" is fulfilled.
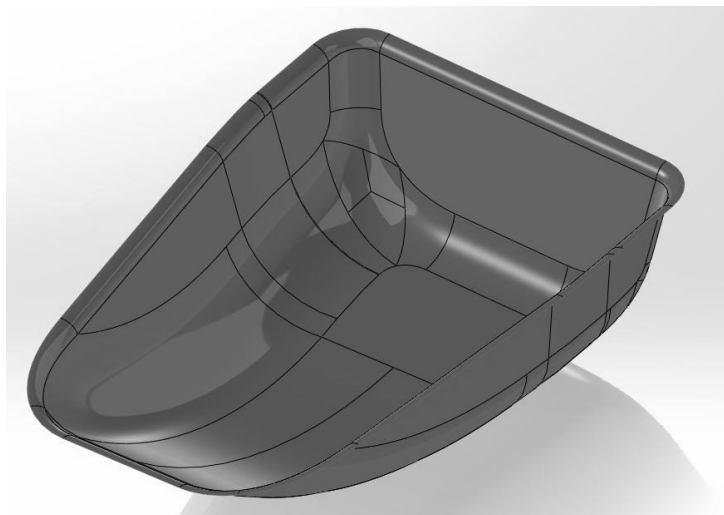
Figure 4.15 The CAD data of real car component.

The tool path algorithm is obtained from CAD drawing of the component as shown in Figure 4.15. When compared with the previous examples, the geometry is relatively

complex due to steep side walls, reaching approximately 80.4^0 of inclination and the depth of the part is 48.977 mm. At first trial, the tool path algorithm is spiral z-level finishing with constant step down infeed strategy and the step width is 0.5 mm. The lubricant is commercial hydraulic oil. The tool path is shown in Figure 4.16.
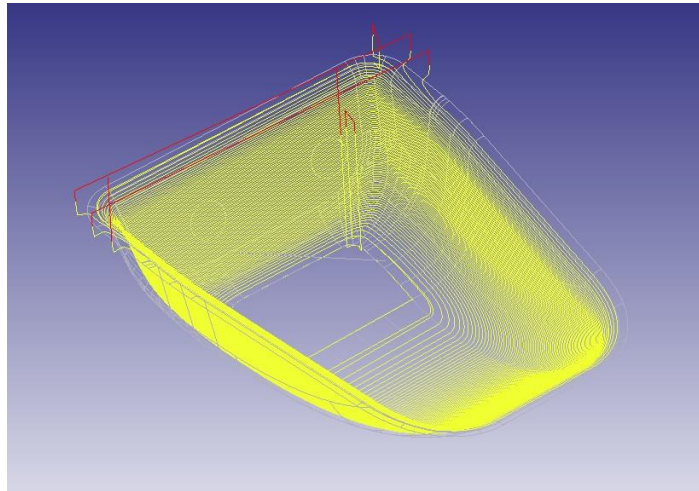
Figure 4.16 Single stage tool path with spiral z-level finishing algorithm.

The feedrate is 2000 mm/min and the spindle is not rotating. As seen in Figure 4.17, the crack has occurred on the blank, after the tool moved 16 mm downward from its initial position.

Figure 4.17 Due to high localized deformation the blank is torn.

After this trial, the other tool path algorithms have been tried. Figure 4.18 shows the part, which is manufactured by using arbitrary stock roughing algorithm. The tool movement is inside to outside direction with 0.7 mm step width. The tool is ordinary steel with the diameter of 10 mm. The feedrate and lubricant is same as in the first trial.

Figure 4.18 (a) is the view from bottom base of failed part and (b) is the view from top base.

The other trial is performed by using different tool, which has the diameter of 15 mm. The tool path algorithm, step width and feedrate was same as in the previous trial. But, the lubricant was different which a bearing grease was. The trial's result is illustrated in Figure 4.19.

Figure 4.19 (a) is the view from bottom base of failed part and (b) is the view from top base.

Another trial was involving the same tool path algorithm but different starting position. The tool path was arbitrary stock roughing with optimized in tool path. The lubricant, step width and the feedrate was the same in previous trial. The tool is ordinary steel with a diameter of 5 mm. The trial's result is shown in Figure 4.20.

Figure 4.20 (a) is the view from bottom base of failed part and (b) is the view from top base.

By using the same tool path algorithm, another trial was conducted; but the tool movement started from inside to outside. The tool diameter, lubricant and the feedrate was the same as in the previous trial. However, the step width was 0.65 mm. As can be seen in Figure 4.21, the tearing was occurred between the flat surface and the inclined wall.

Figure 4.21 (a) is the bottom view of failed part and (b) is the top view.

After several trials, it was concluded that to manufacture this real car component is not succeeded by single step. Afterwards, the first trial including multi-stage tool path strategy, is performed. In this sense, a pre-intermediate shape was manufactured. It was executed by offsetting the side walls with the reduction of steeper angle. Figure 4.22 displays the tool path in which the step width is 0.5 mm. The algorithm is z-level finishing with spiral tool path and the feedrate was 2000 mm/min.
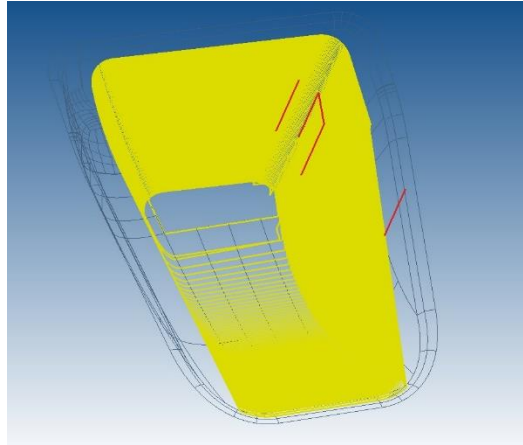
Figure 4.22 The tool path belongs to real car component which was offset.

After the application of this tool path, the second stage was performed by using the same tool path algorithm. As can be seen in Figure 4.23, the tool moved 10 mm downward from starting position, then the blank is torn. This most probably due to the transition range of tool paths (the distance of tool paths between the first and the second) is so much and the tool's diameter is smaller than this range. According to this, during the tool movement, the indentation occurs much more, thus the blank could not flow.

(a)   (b)

Figure 4.23 (a) is the view from bottom base of failed part and (b) is the view from top base.

The other trial for manufacturing this part is performed by using fuzzy offset command. This command provides the generation of an offset surface which is not a precise offset having a blurry resemblance to the original surface. With the help of this command, 10 offset surfaces were created. For each surface equidistant finishing algorithm was used (Figure 4.24).
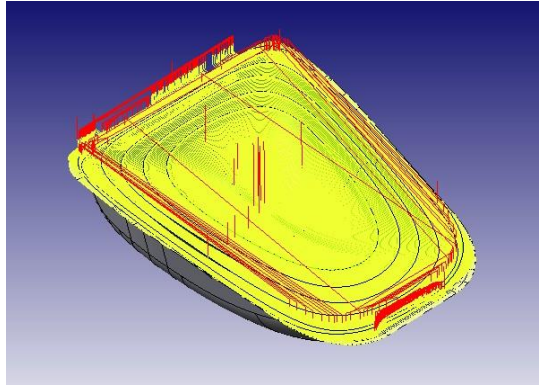
Figure 4.24 Multi-stage tool paths rising from fuzzy offset command.

This multi-stage tool path strategy is achieved. However, due to the initial geometry of the surface which resembles to an eye drop, the top base mismatches with the final geometry. As can be seen in Figure 4.25, there is a defect at the top base of the component.
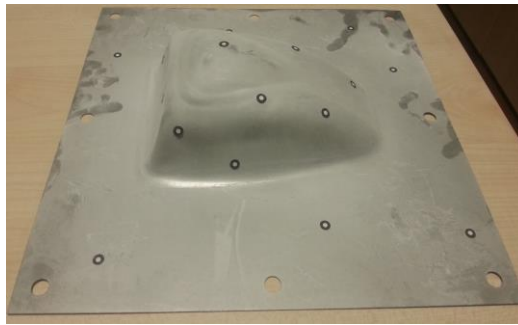
Figure 4.25 The manufactured part with a defect due to initial geometry of the tool path.

Finally, a down-up-down-up-down (D-U-D-U-D) strategy is developed (Figure 4.26). The tool path algorithm was equidistant finishing algorithm with flow strategy. In order to carry out this, 5 different surfaces were created (Figure 4.27).
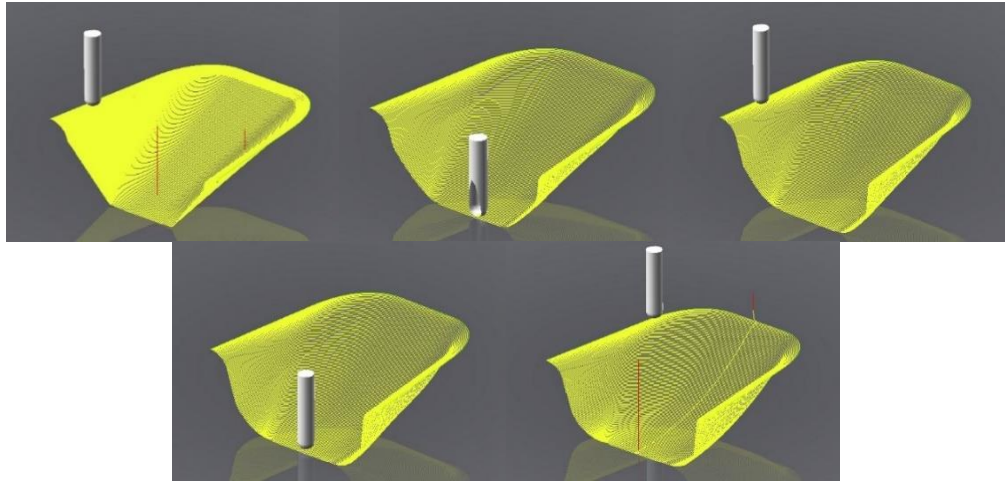
Figure 4.26 The (D-U-D-U-D) strategy for manufacturing the real car component.

The sheet was pre-formed with an initial angle of 50^0. The angle was increased at each step and at last, the car component was successfully manufactured.
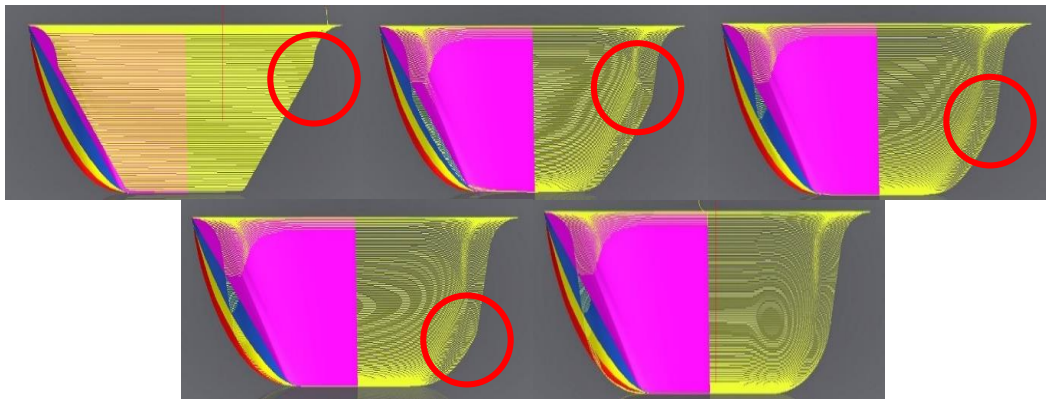
Figure 4.27 All steps with different tool paths starting from pre-form with 50^0 inclination. The red circles demonstrate the transition regions.

The manufactured part is demonstrated in Figure 4.28. As can be seen in the figure, there are some small defecst on the top surface and the lateral parts. The reason is the transition of one tool path to another tool path.
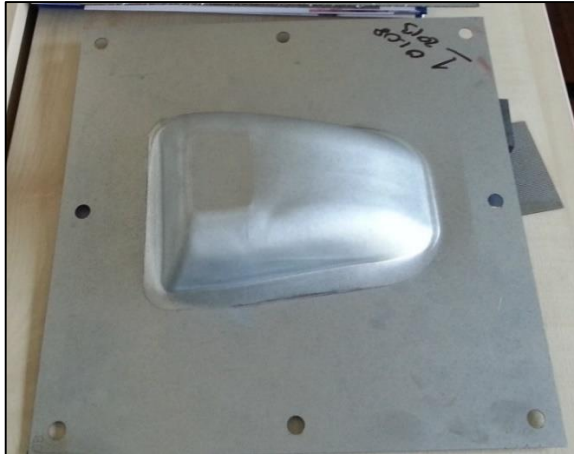
Figure 4.28 The manufactured part with ISF.

4.2. 3D Coordinate Measurements

4.2.1 Introduction

In order to measure the geometry of the manufactured parts as well as comparing with the numerical solutions, GOM-Atos optical measurement system is used (Figure 4.29).

Figure 4.29 The GOM-Atos 3D coordinate measurement system.

The data from optical measurements are exported and converted to geometric surface by an appropriate code in MATLAB®, then the geometries are compared with the finite element results in order to obtain geometric tolerances. Before the explanation, it is worth mentioning about the information of ATOS system in a brief manner.

Nowadays, the design of a car or any metal forming industry part, the view point of CAD construction or NC manufacturing become more significant than the last years. In order to establish or provide the relation between the real component and the numerical description, precise measurements are required. ATOS system is an advanced topometric sensor using the digitizing system. Due to the fact that the objects can be measured precisely, quickly and with high resolution based on the triangulation principle.

Figure 4.30 The system is based on triangulation system.

The sensor projects the fringe patterns onto the desired object then the cameras record these patterns (Figure 4.30). Each single measurement generates up to million data points (if the camera is 2M then 2 million data points are generated) [61].

Before the measurement there are some uncoded reference points (Figure 4.31) which are stuck on the measured object. By using these reference points, ATOS transforms each of the measurements into a common global coordinate system such as point cloud or sections. The reference points behave as connection points for the individual measurements. It means that the measurements, which are done individually, are transformed into a common 3D view with best fit so the system identifies the 3D coordinates of these reference points.
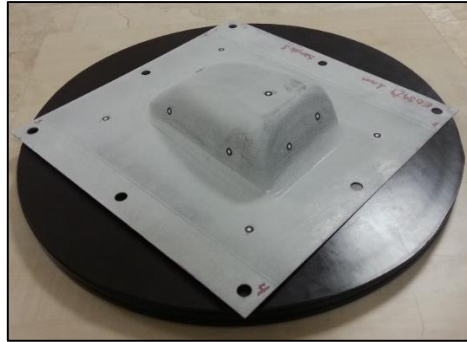
Figure 4.31 The uncoded points are stuck to obtain the point clouds in the software.

4.2.2 Experimental Campaign

Figure 4.32 shows the measurements of geometry of the truncated cones and square pyramids with 5 mm, 10 mm and 15 mm tool tips, respectively.
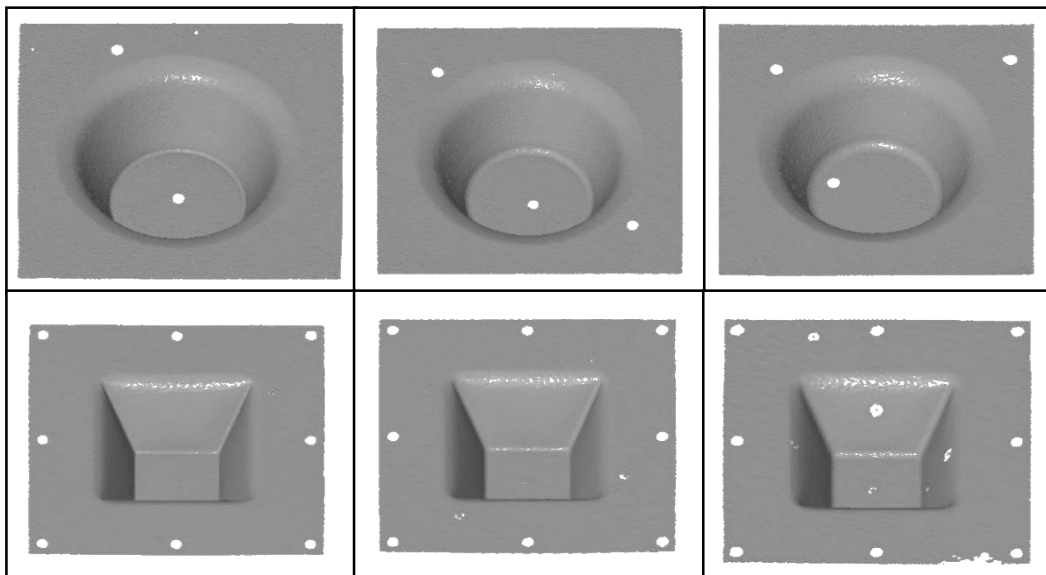
Figure 4.32 The truncated cones and square pyramids manufactured by different tool tips.

On the other hand, for the investigation of experimental results versus both implicit&explicit results, a small part is manufactured by 10 mm tool tip. Figure 4.33 demonstrates the scanned part.
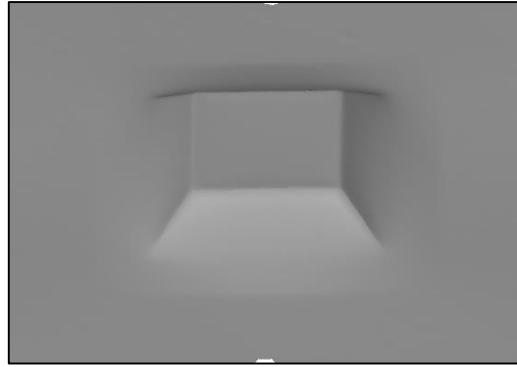
Figure 4.33 Truncated square pyramid with a depth of 20 mm.

After these measurements the manufactured real car components, which are irregular and regular, are analyzed. The parts are compared with the CAD data (Figure 4.34) and the deviation's are detected. As in Figure 4.35, the differences are given in a legend bar.

(a)   (b)
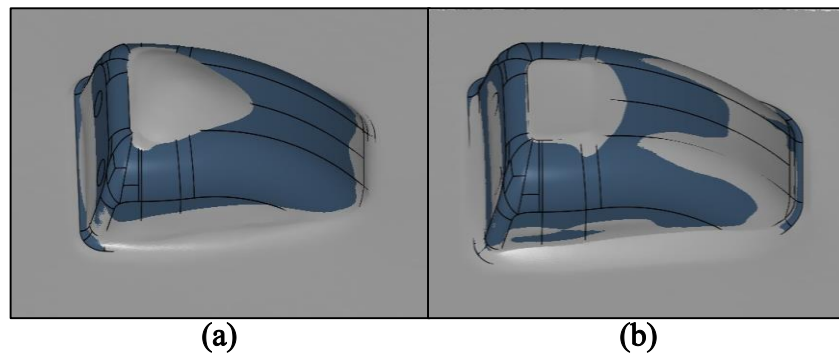
Figure 4.34 Real car component with different tool path algorithms, (a) is manufactured by z-level finishing with fuzzy offset surfaces and (b) is manufactured with 5 steps by equidistant finishing algorithm.

As can be seen in the figure (a) the top surface deviates about 10.2 mm form the desired shape. However the other regions are in a good agreement with desired shape. On the other hand, the top surface at second part (b) is almost identical with the desired shape. But, the other regions have some deviations which are not exceeding 3 mm at the adjacent point between the edge and the corner radius.
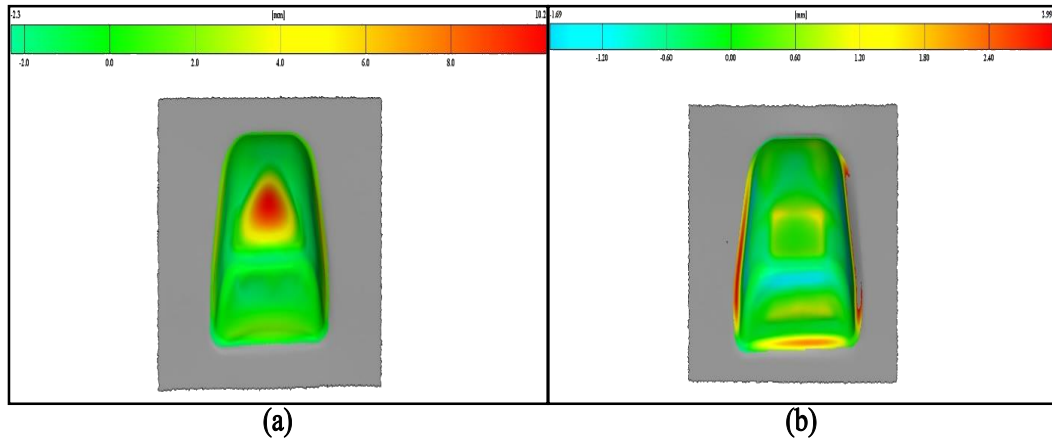
Figure 4.35 The geometric comparison of CAD drawing and optical measurement, (a) demonstrates the first trial with defect, (b) demonstrates the last trial.

4.3 Deformation Measurements

4.3.1 Introduction

In any sheet metal forming processes, the deformation analysis of the formed parts has a significant role to measure the major strain, minor strain and thickness distribution. In the deformation measurements, GOM-Argus optical forming analysis system (hardware and software) is used to obtain the distribution of major and minor strain and the thickness distribution on the surface (Figure 4.36).

Figure 4.36 GOM-Argus optical forming analysis system in MFCE, (a) the etching system with stencil and marker head, (b) camera system and coded referece points .

The measurement principle of the system can be explained by the comparison of the points (obtained by electrolytic marking (Figure 4.36 (a)) applied to the sheet before the measurement) either in undeformed or deformed state [62]. To describe the electrolytic marking firstly, the sheet is cleaned by some alcohol or benzene for the purpose of the degreasing and then right electrolyte is chosen. Also, the right stencil should be chosen for the precise measurement. If the part geometry is complicated then it is better to use relatively small dotted stencil. The illumination is also an important issue in order to prevent the experimental errors.

After the forming operation the formed part is measured by a camera which records the marked points in different images with different views. Firstly, four reference images are captured at the top of the formed part with 90^0 angle and then, it continues taking several images with different views from 60^0 and 45^0, respectively (see Figure 4.37).

(a)　　　　　　　　　(b)
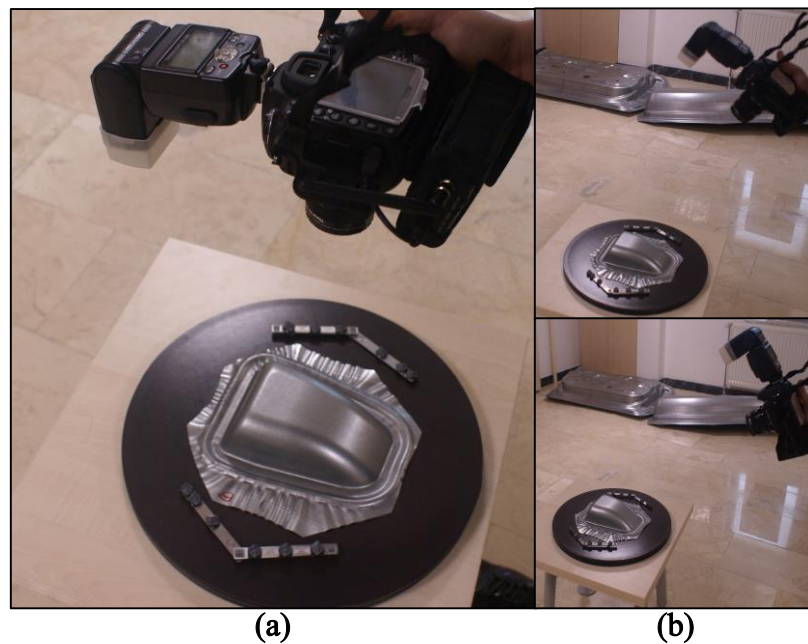
Figure 4.37 The image taking procedure, (a) shows the reference image taking and (b) at different angles.

The computation is carried out by calculating the 3D coordinates of the coded and uncoded points which are put around the formed part. This measuring method is called photogrammetry.

For the computation of strain and thickness reduction, data the system compares the undeformed and deformed states. In a standard measurement, there is no need to capture undeformed part's images due to the results of theoretical point distance

defined in the project parameters. This is called virtual reference which is used mostly for relatively non precision parts e.g. automotive inner-door panel.

4.3.2 Experimental Work

The comparisons between the experimental and numerical results will be made in next chapter. In this subsection, the deformation behavior of different parts in ISF is explained in detail. As mentioned before, the mode of deformation is plane strain tension for truncated cones. However, the mode of deformation is both plane strain tension and biaxial stretching at the corners for truncated square pyramids. In deep drawing process, the deformation behavior tends to pure shear in which the strain ratio is -1 [32].

The first investigation involves the truncated cone, which has 20 mm depth with the wall angle of 40^0, manufactured by 10 mm diameter tool. As can be seen in Figure 4.38, the measured part and its major-minor strain diagram are shown. Secondly, the truncated square pyramid is investigated. In Figure 4.39, a manufactured pyramid with the diameter of 15 mm tool tip is demonstrated. The part has a depth of 60 mm with 60^0 inclination.

Finally, the two real car component parts are investigated with the aim of comparing two different processes. The first part is manufactured by ISF process and the second part is manufactured by deep drawing process. As can be seen in Figure 3.40, the deformation mechanism is the plane strain tension. Especially, the maximum deformation occurs at the adjacent point of lateral side and the top radius. After this investigation the truncated square pyramid has examined. As mentioned before (see subsection 3.2.4), ISF process has higher forming limits than traditional forming limits. Although the forming limits exceed the conventional forming limits, there is no tearing in the parts. As seen Figure 4.39 and Figure 4.40, the parts did not fail though their strain values are high.
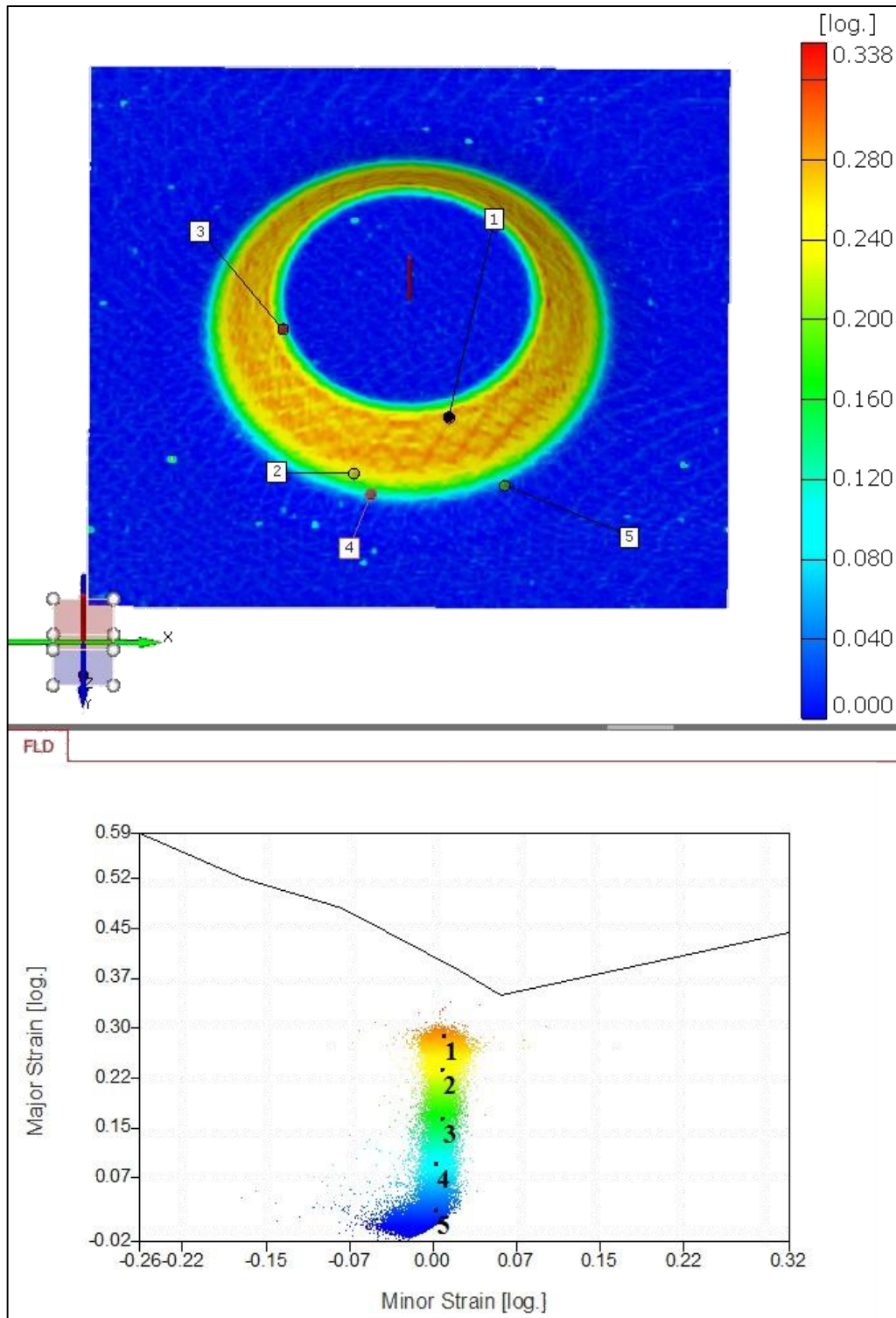
Figure 4.38 The location of measured dots at strain space.

As can be seen in the figure the lateral wall has the plane strain condition. However, when the tool passes through from one lateral side to other, the biaxial stretching occurs (Figure 4.39 – Point 6 and 7).
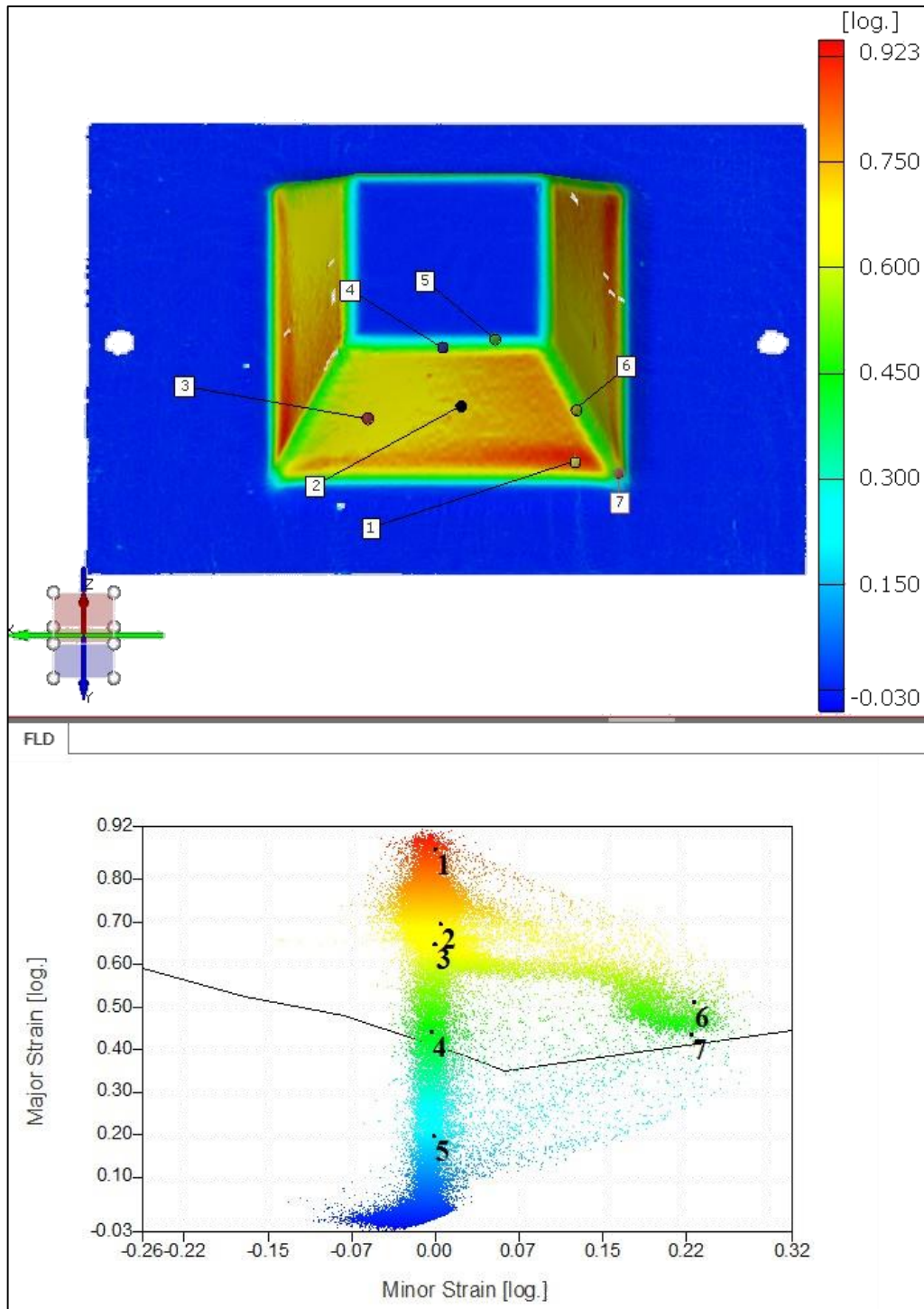
Figure 4.39 The location of measured dots at strain space.
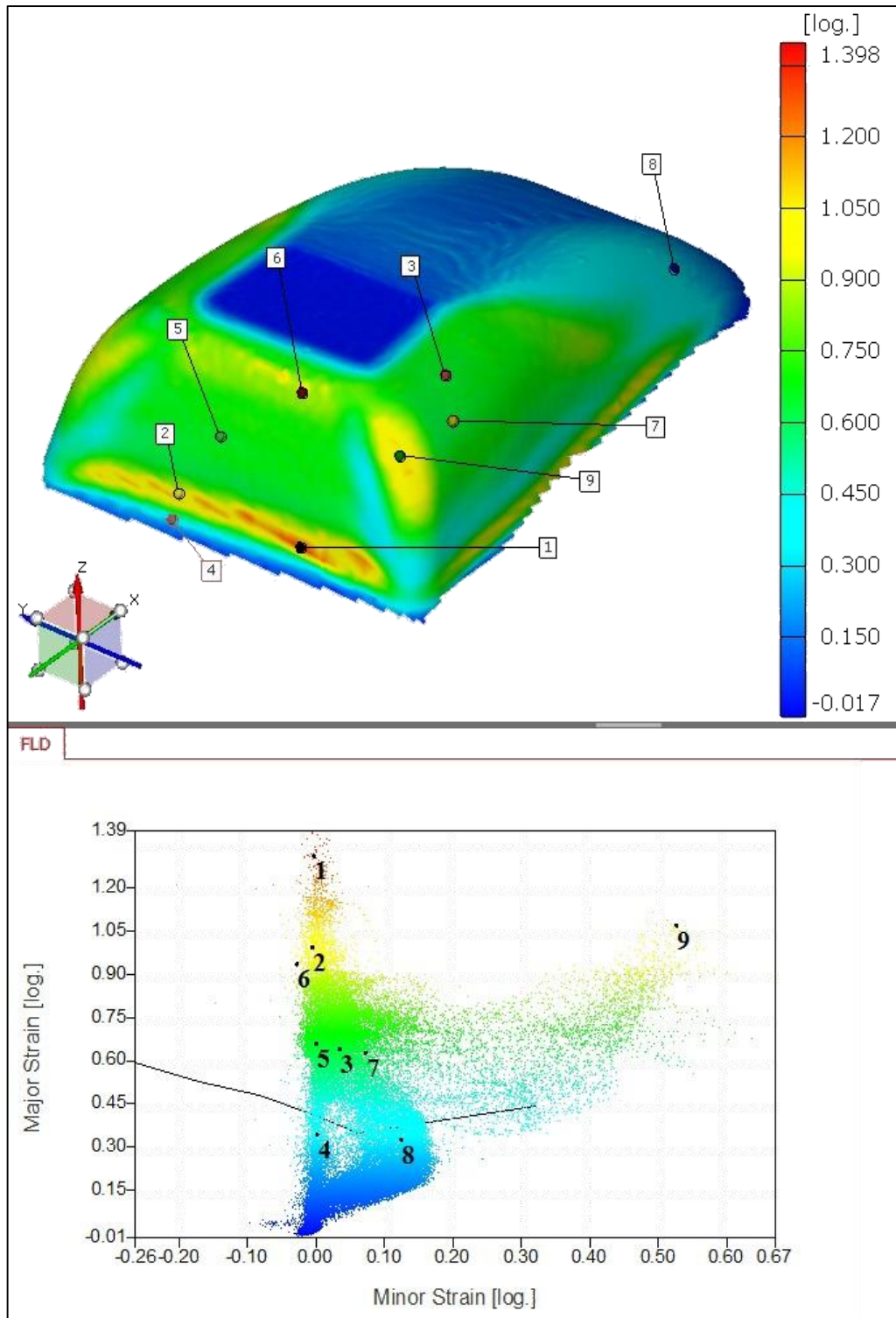
Figure 4.40 The real car component manufactured by ISF process and the optical
measurement results in strain space.
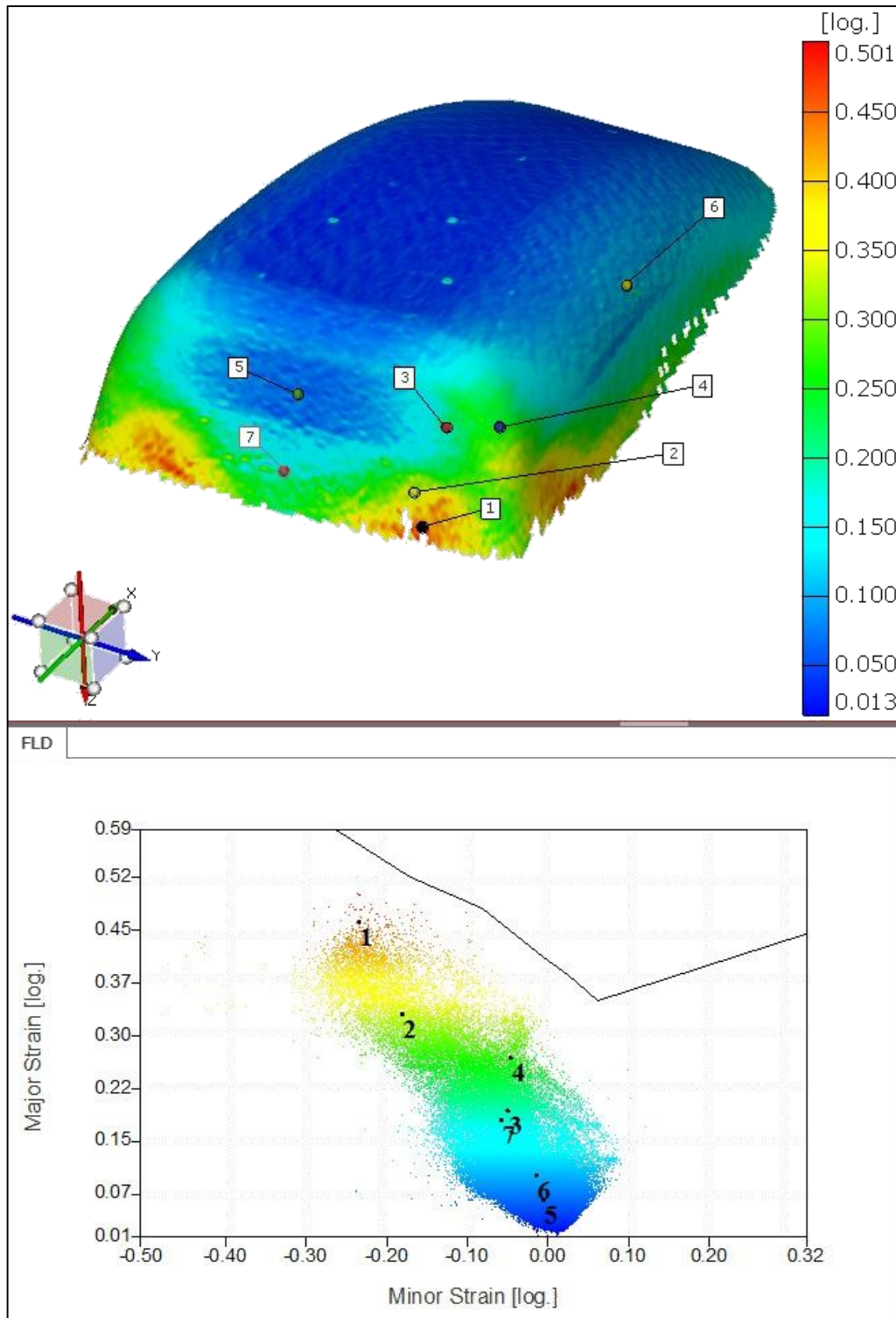
Figure 4.41 The real car component manufactured by deep drawing process and the optical measurement results in strain space.

Figure 4.40 and Figure 4.41 illustrate the deformation behavior after two different forming process as mentioned before. In Figure 4.40, the real car component manufactured by ISF is given. As can be seen in the figure, while at the lateral sides the mode of deformation is plane strain but at the lateral corners (Figure 4.41 – Point 8 and 9) the deformation behavior is biaxial stretching. Besides, the deep drawn part shows the pure shear condition.

The results given above for realizing the mode of deformations in ISF and deep drawing. In the following section, a detailed validation will be done with numerical results.

CHAPTER 5

VALIDATION OF RESULTS

In this chapter, the validity of the predictions of the numerical models are assessed through comparison with the measurements of manufactured components. To this end, three different components are manufactured using the 3-axis vertical CNC milling machine as mentioned before. Two of those components are relatively simple in terms of geometry whereas the third one is an actual car component.

The CAD data of the component is converted into appropriate NC-codes using the commercial software Hypermill®. Meanwhile, NC-codes are converted into coordinate data by using MATLAB® which in turn is used in the FEA phase. After the manufacturing process, optical measurements are conducted and compared with the implicit and explicit FEA. The comparisons have been made in terms of geometries, major-minor strain and thickness distributions. In the following subsections, three geometries are assessed separately. In the all assessments, the bottom and top bases are assumed as in Figure 5.1.
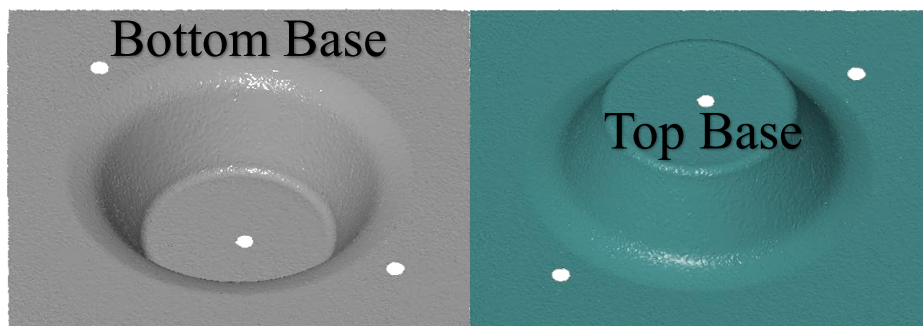
Figure 5.1 The dome part is assumed to be top base and the other part is assumed to be bottom base in all assessments.

5.1 Truncated Cone

As mentioned before, the first considered geometry is a truncated cone with a base diameter of 128 mm and a height of 40 mm. The inclined wall angle of the part is 60^0. This part is manufactured by using 5 mm, 10 mm and 15 mm diameter spherical tools. The pitch size is 0.5 mm and the thickness of the sheet is 0.8 mm. The assessments have been made by using two orthogonal X and Y section profiles on each part as shown in Figure 5.2.
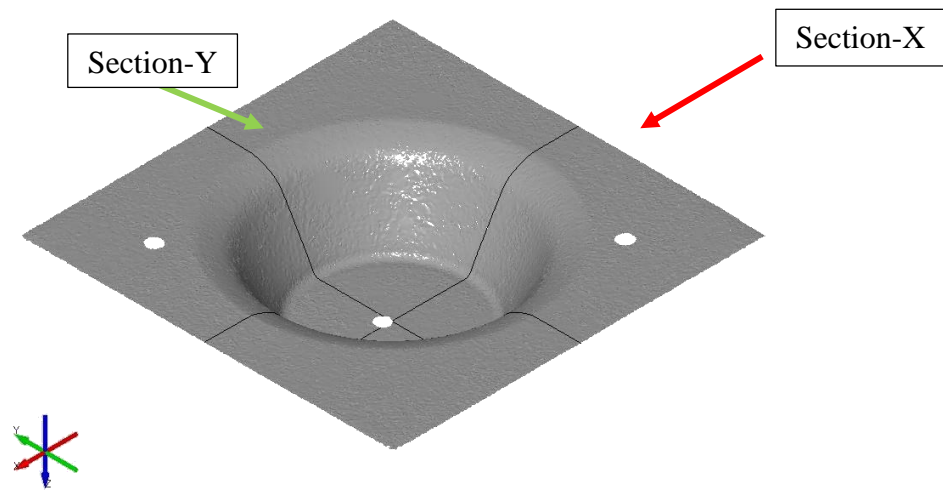
Figure 5.2 The surface from optical measurement with the tool diameter of 10 mm.

In Figure 5.3, the deformed profiles for 5 mm diameter tool obtained from optical measurements and FEA are compared along the Y-axis. The implicit analysis profile differs from the optical measurement 1.5 mm at the inclined surface. Explicit and implicit analysis results are consistent on the inclined surface. But, the agreement failed on the top base. The difference is 0.47 mm in the direction of Z. One reason is most probably due to dynamic effects, while the first indentation by the tool performs, the tool applies an impact onto the sheet and the equilibrium of the solutions system recovers the equilibrium condition. The other possible reason is, the tool starts to move to downwards by an acceleration, and then the tool decelerates at the clearance plane.
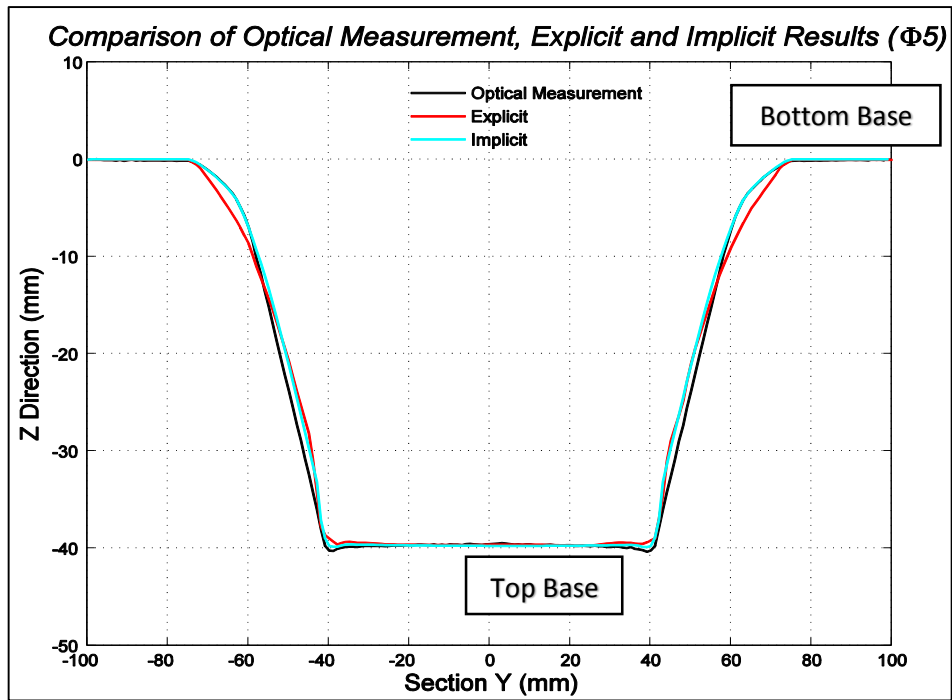
Figure 5.3 The geometrical comparison through section along Y.

Additionally, the explicit analysis profile deviates 3 mm both from optical and implicit profiles on the bottom base. Moreover, it deviates 1 mm in the direction of Z on the top base.
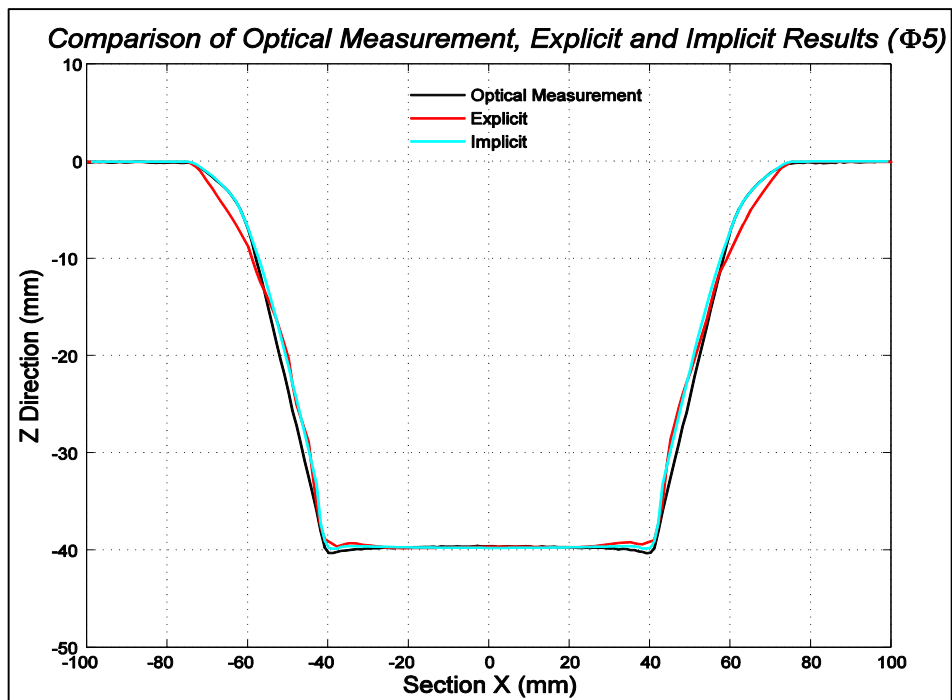
Figure 5.4 The geometrical comparison through section along X.

As shown in Figure 5.4, the comparison along section-X is very similar to section-Y both qualitatively and quantitatively.

After geometric comparisons, major and minor strain profiles have been compared. In Figure 5.5, the major strain profiles are examined. The explicit and implicit results agree well with the optical results with a maximum deviation of 4%. However, as can be seen in the figure the optical measurement result has a loss in symmetry due to the measurement errors. This is probably due to the fact that while performing the measurement, some of the grids could not be computed by the optical measurement system. The difference between the implicit and explicit analysis does not exceed 3%.

Figure 5.5 The major strain comparison of optical measurement, explicit and implicit results for section along Y.

Although there is a loss in symmetry in the optical measurement profile in Y direction, as seen in Figure 5.6, the symmetry is preserved in X direction in the optical measurement profile.

Figure 5.6 The major strain comparison of optical measurement, explicit and implicit results for section along X.

Also, the consistency between the implicit results and optical measurement results is better than the section-Y results. The difference between the explicit results and implicit results are almost same as in the section-Y results.

Minor strain profiles are given in Figure 5.7. It has to be noted that, minor strains are much smaller than the major ones in magnitude. Although the predictions of the numerical models are of the same order of the optical measurements, at certain locations, the details of the measurement profile could not be captured. The implicit results deviates from optical measurement results with the strain value of 0.03. Additionally, the explicit result has a maximum deviation of 0.06 in terms of strain.

As seen in Figure 5.7 and Figure 5.8, there is a loss in symmetry in optical measurement result due to the measurement errors mentioned before. Moreover, the reason of inconsistency between explicit and optical measurement results is dynamic effects. In Figure 5.8, the difference between implicit results and optical measurement results does not exceed 0.03 in terms of strain value. Additionally, the explicit result has the maximum deviation of 0.04 in terms of strain from optical measurement results.

Furthermore, the thickness distribution has been investigated. As it was described before, the initial thickness of the blank is 0.8 mm. Generally, if one calculates the final thickness by using sine law, it will be obtained as approximately 0.4. Hence, as can be seen in Figure 5.9 and Figure 5.10, the final thicknesses are as expected. The implicit and optical results are consistent. However, the explicit analysis result captures the final thickness with a maximum error of 8% in Y section. Moreover, the result of explicit analysis in section-X has 5% difference. These discrepancies can be considered acceptable due to manufacturing tolerances in automotive industry.
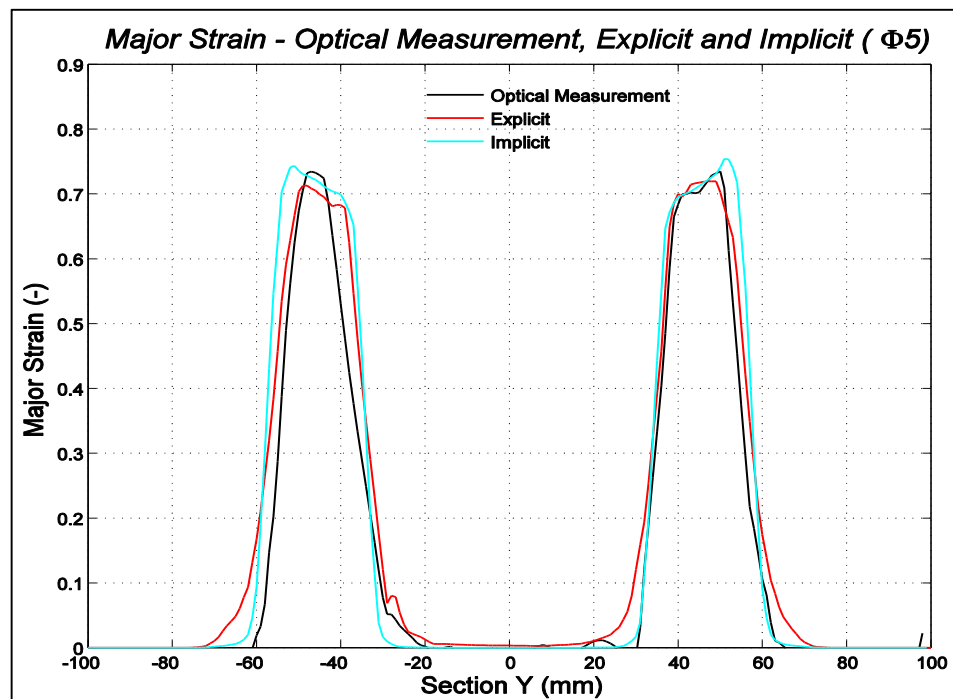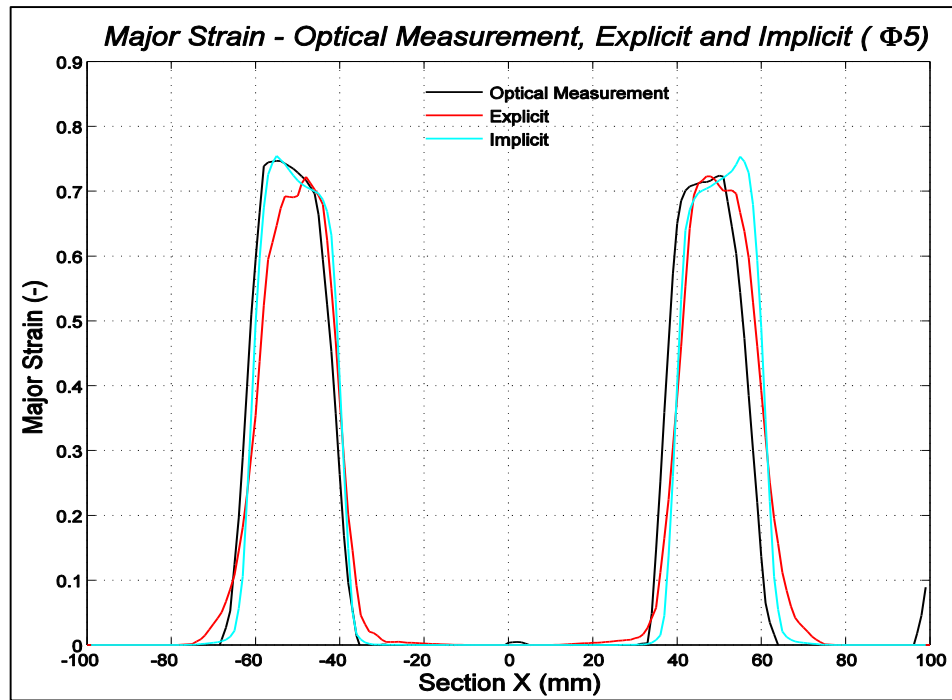

Figure 5.7 The minor strain comparison of optical measurement, explicit and implicit results for section along Y.
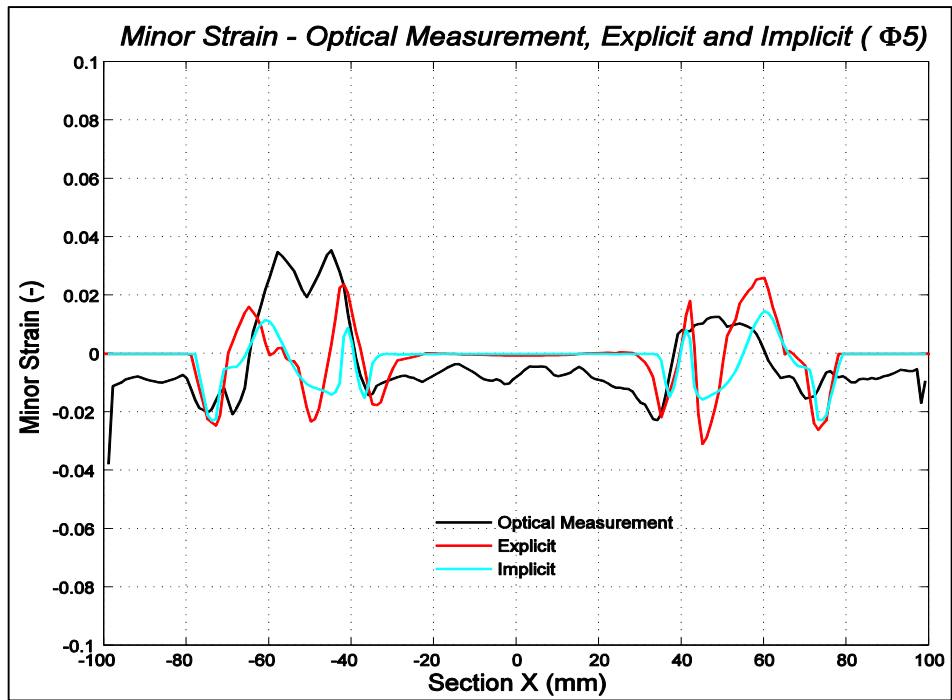
Figure 5.8 The minor strain comparison of optical measurement, explicit and implicit results for section along X.

Figure 5.9 The thickness distributions of optical measurement, explicit and implicit results for section along Y.

Figure 5.10 The thickness distributions of optical measurement, explicit and implicit results for section along X.

Due to minor discrepancies between section-Y and section-X profile comparisons, only section-Y profiles are going to be examined in the rest of the subsection.

The geometrical comparisons for 10 mm diameter tool are presented next. Especially, if only implicit and optical results are considered, the results are consistent throughout the entire part. Although there is a consistency between implicit and optical results, the explicit results deviates at the bottom and top bases. It deviates 2 mm from optical and implicit results at the bottom base. Also, there is a bulge effect [48] at the top base, as seen in Figure 5.11, due to the tool's first indentation at this region.
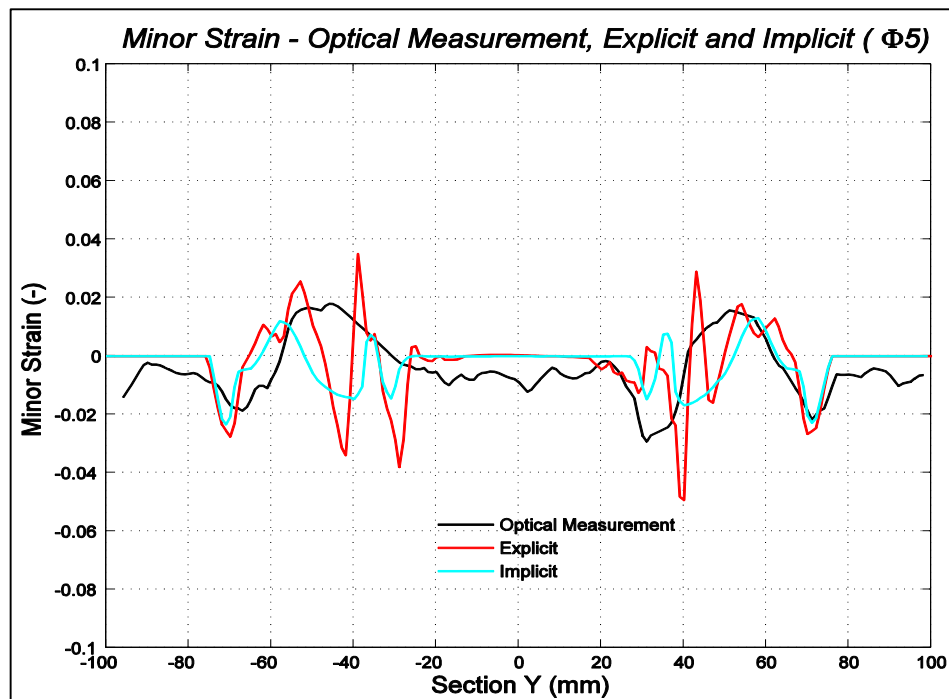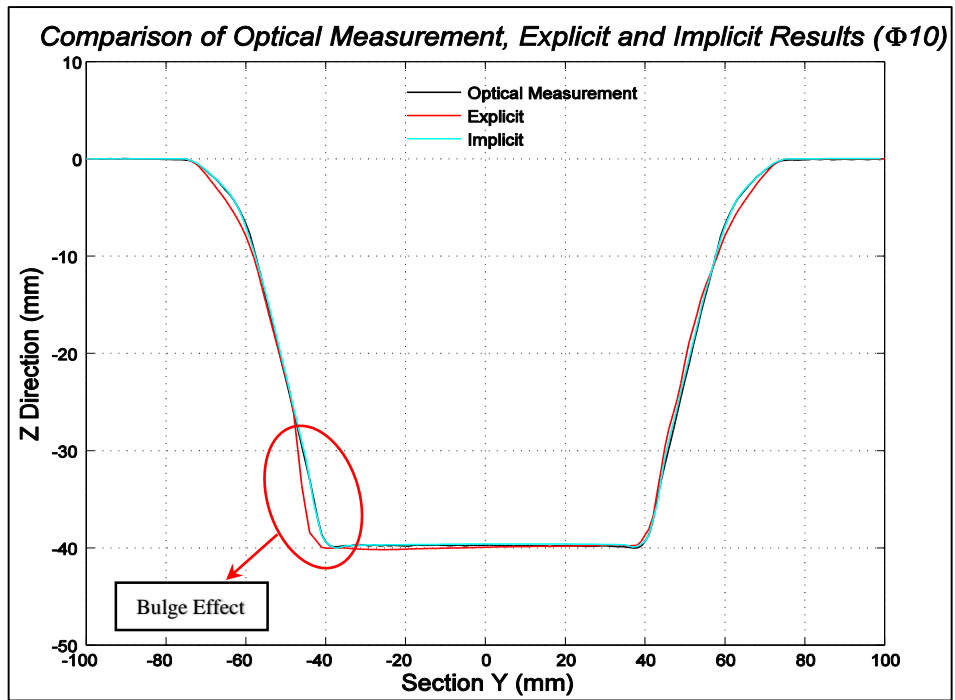
Figure 5.11 The geometrical comparison of optical measurement, explicit and implicit results for section along Y.
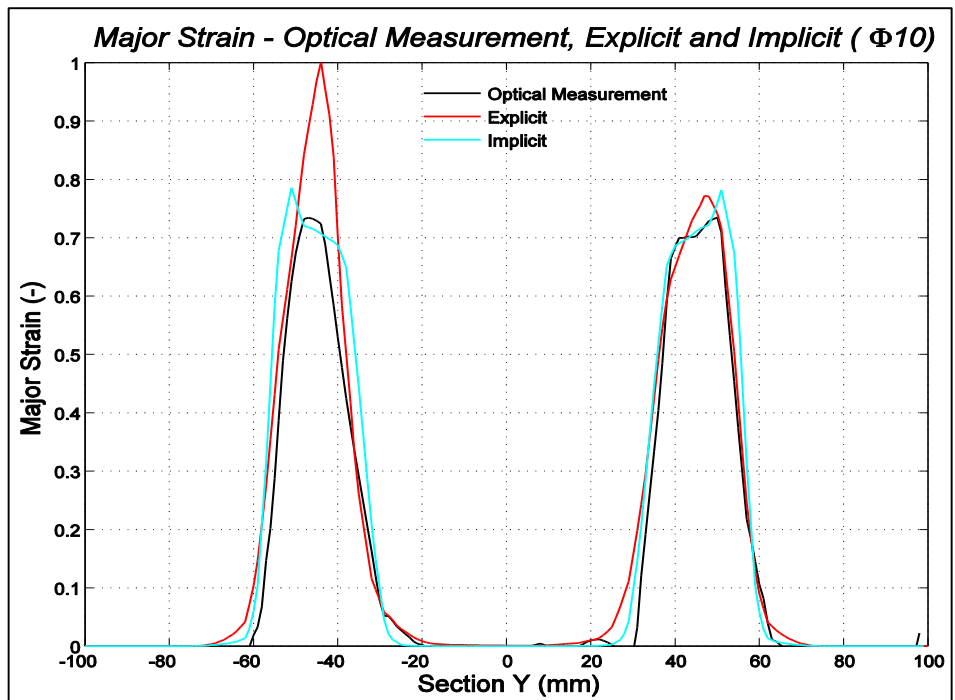
Figure 5.12 The major strain comparison results for section along Y.

The major strain comparisons have also good agreement. As can be seen in Figure 5.12, the implicit analysis result differs 6% from optical measurement results.

79

Moreover, the explicit analysis result is almost identical with implicit results. However, there is a loss in symmetry on the left, which is most probably stemming from the tool path starting position and dynamic characteristics of the solution procedure.

As can be seen in Figure 5.13, both implicit and explicit profiles deviate from optical measurement profile in which the deviation is not exceeding 20%.
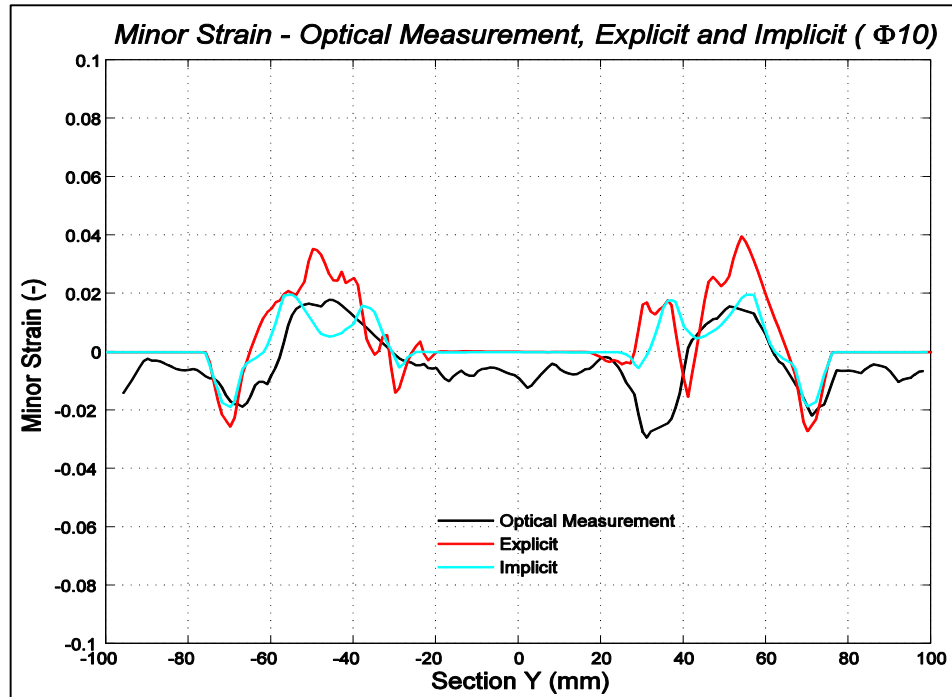
Figure 5.13 The minor strain comparison results for section along Y.

As far as the thickness distribution is concerned, there is loss in symmetry in optical measurement result. Moreover, due to the dynamic effects as mentioned before, the explicit analysis result differs significantly (9%) at the initial position of the tool.
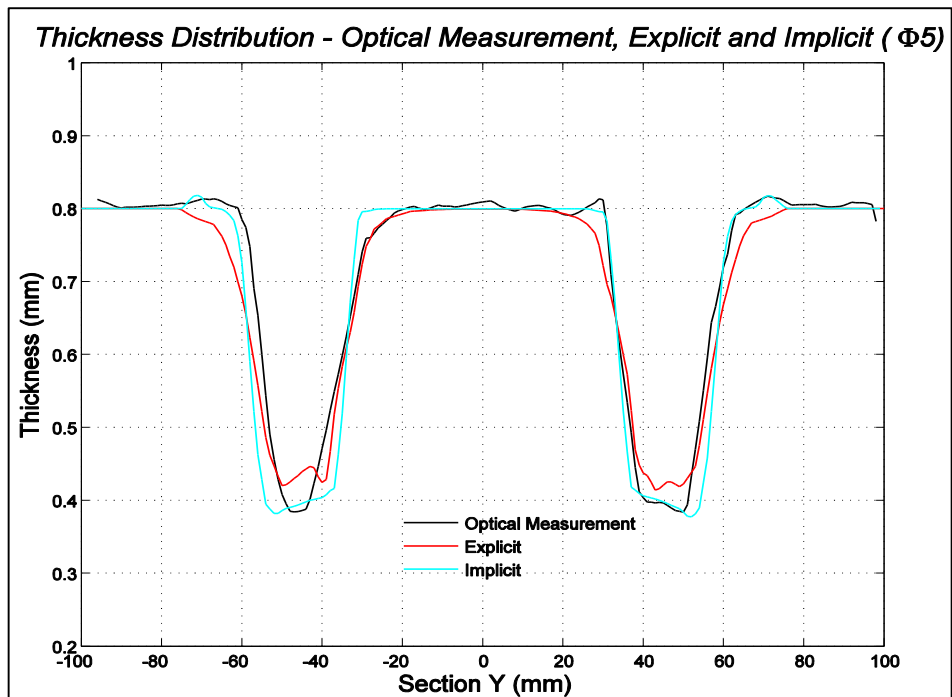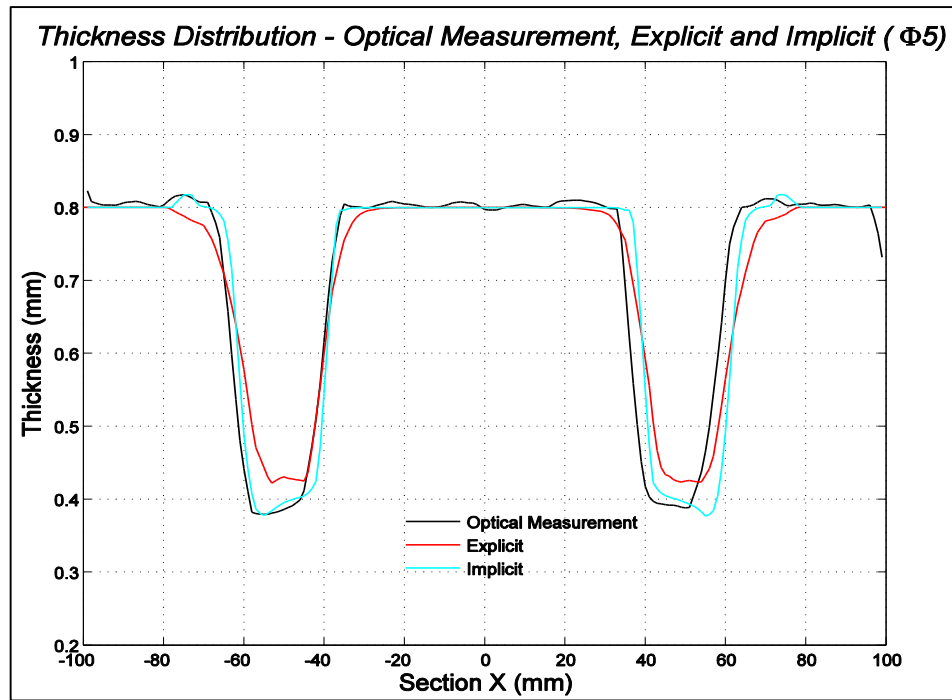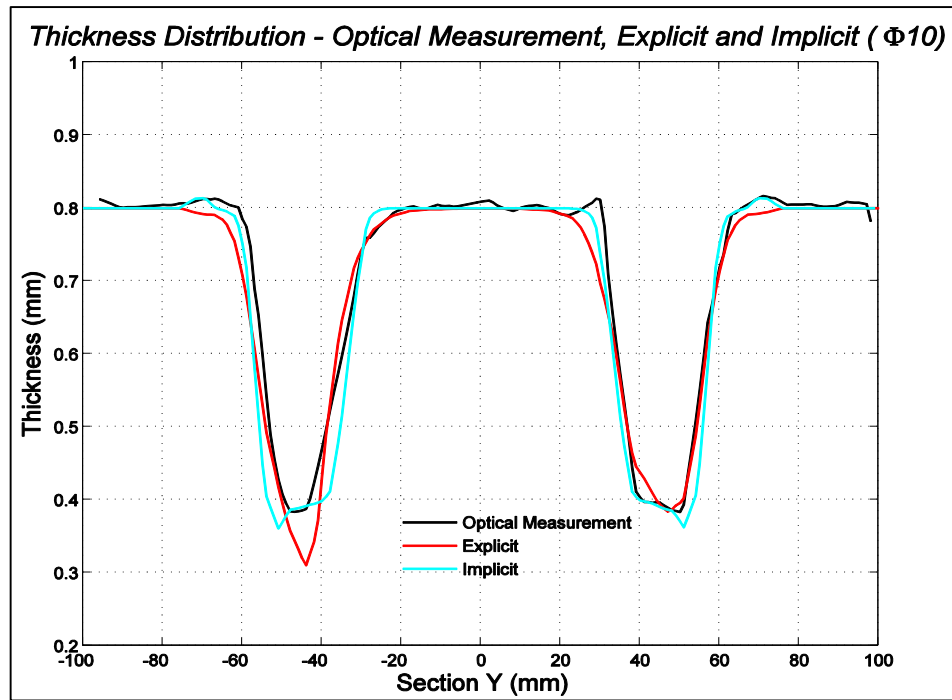
Figure 5.14 The thickness distribution of optical measurement, explicit and implicit results for section along Y.

Another investigation was performed by using 15 mm diameter tool head. In Figure 5.15, the geometric profiles of the truncated cones, which are manufactured by 5 mm, 10 mm and 15 mm diameter tool, are illustrated. As seen in the figure, there is no major discrepancies between the profiles on the bottom base and the inclined wall. On the other hand, there is a difference on the top base. The results and main findings can be itemized as follows:

- If the tool diameter decreases, the irregularities at the top base corner increases due to high contact stresses between the tool and the blank.
- The use of smaller tool effects the geometrical profile at the top base, but it disappears when the tool diameter increases.
- The geometric accuracy decreases while using larger tool tip.
- While forming operation, if any counter tool or partial die was used, the dimensional accuracy would be better for each case.
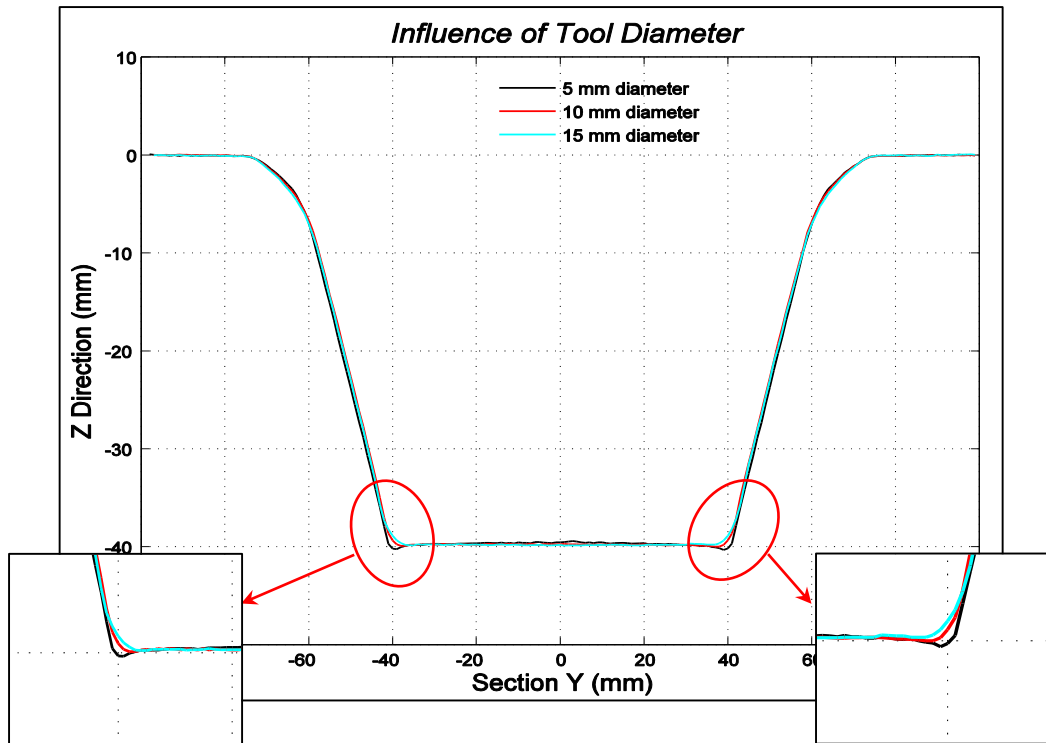
Figure 5.15 The geometrical profiles using 5 mm, 10 mm and 15 mm diameter tool.
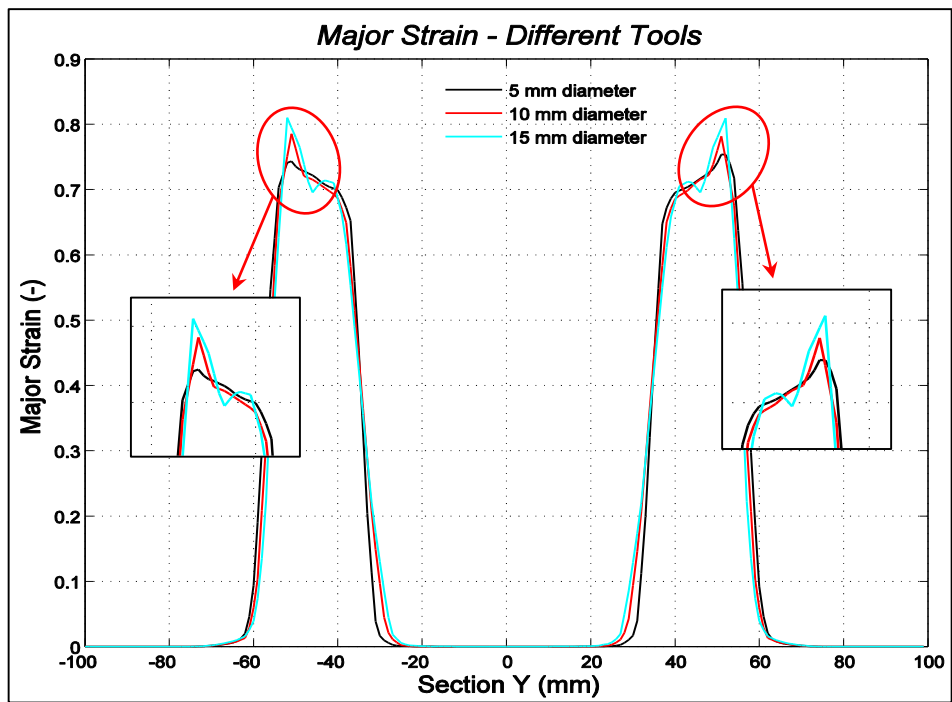
Figure 5.16 The comparison of implicit FEA profiles of 5 mm, 10 mm and 15 mm diameter tool through section along Y.
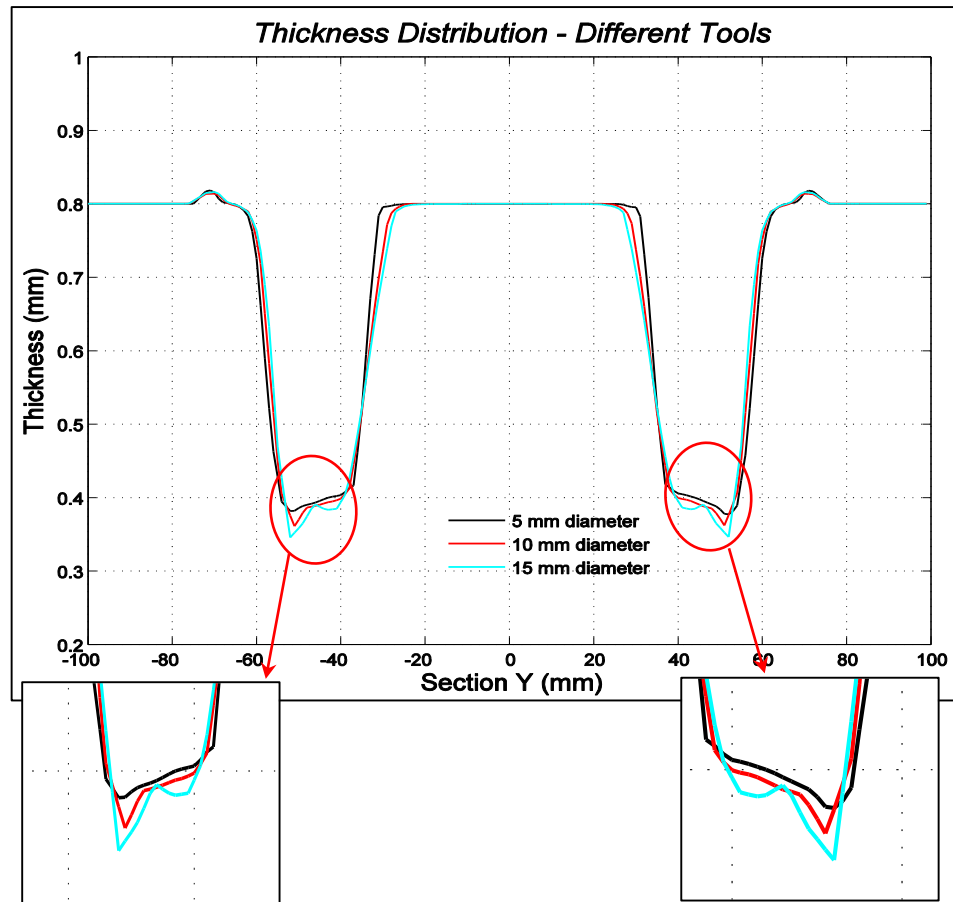
Figure 5.17 The thickness comparison of implicit FEA profiles of 5 mm, 10 mm and 15 mm diameter tool through section along Y.

- While using larger diameter tool, the major strains reach to different values on the inclined walls of the manufactured parts.
- The sharpness of the curves change with decreasing tool diameter. This alteration is similar in thickness distribution profiles. As seen in Figure 5.17, the sharp surfaces has become smoother in smaller tool diameter.
- There is a minor discrepancy at the inclined walls when the tool diameter is increasing.
- The process becomes similar to stamping process by using larger diameter tool, thus it causes a reduction in formability.
- By using smaller tool, the strains are concentrated at the deformation zone. As seen in Figure 5.16, there is a jump at a certain point on the inclined wall when larger diameter tool is used, which causes cracking.

On the basis of these comparisons, it is concluded that regardless of the tool diameter, implicit analysis are very close to the optical measurement results.

The other study is to investigate the implicit analysis and experimental results at different depths. Within this scope the conical parts are manufactured with a depth of 5 mm, 10 mm, 15 mm and 20 mm with 10 mm diameter tool. The wall angles are equal and 40^0 for each part. As seen in the figure, the dimensional accuracies are consistent both in implicit analysis and experimental results.
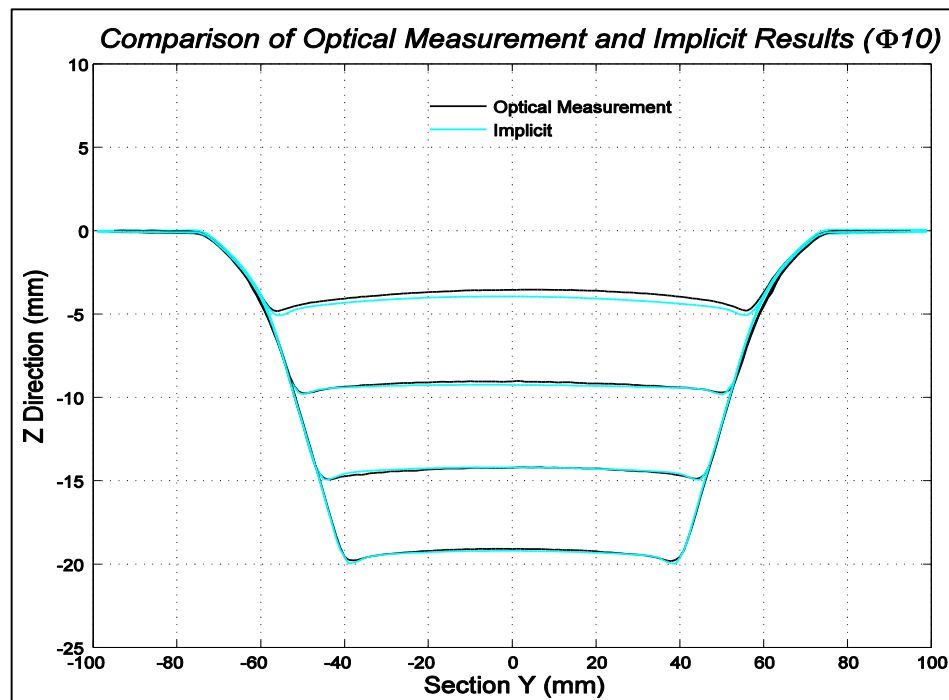
Figure 5.18 The geometrical comparison results at different depths through section along Y.

Figure 5.19 and Figure 5.20 illustrate the results of major strain and the thickness distribution with implicit FEA in comparison with optical measurements. The illustration involves only the half section of the profiles. The maximum value of major strain predicted by the FEA is 0.26, whereas the value is approximately 0.29 in optical measurement for 20 mm deep part. Regarding the major strain values, the agreement is quite good in both cases. On the other hand, it has to be noticed that there is minor discrepancy between FEA and experiments since there could be an experimental error. Additionally, while the major strain variation is higher considering 5 mm depth and 10 mm depth, the major strain values are almost the same in 15 mm and 20 mm deep

part. This suggests that, for this particular geometry after a certain depth, the change in major strain and thickness is marginal.
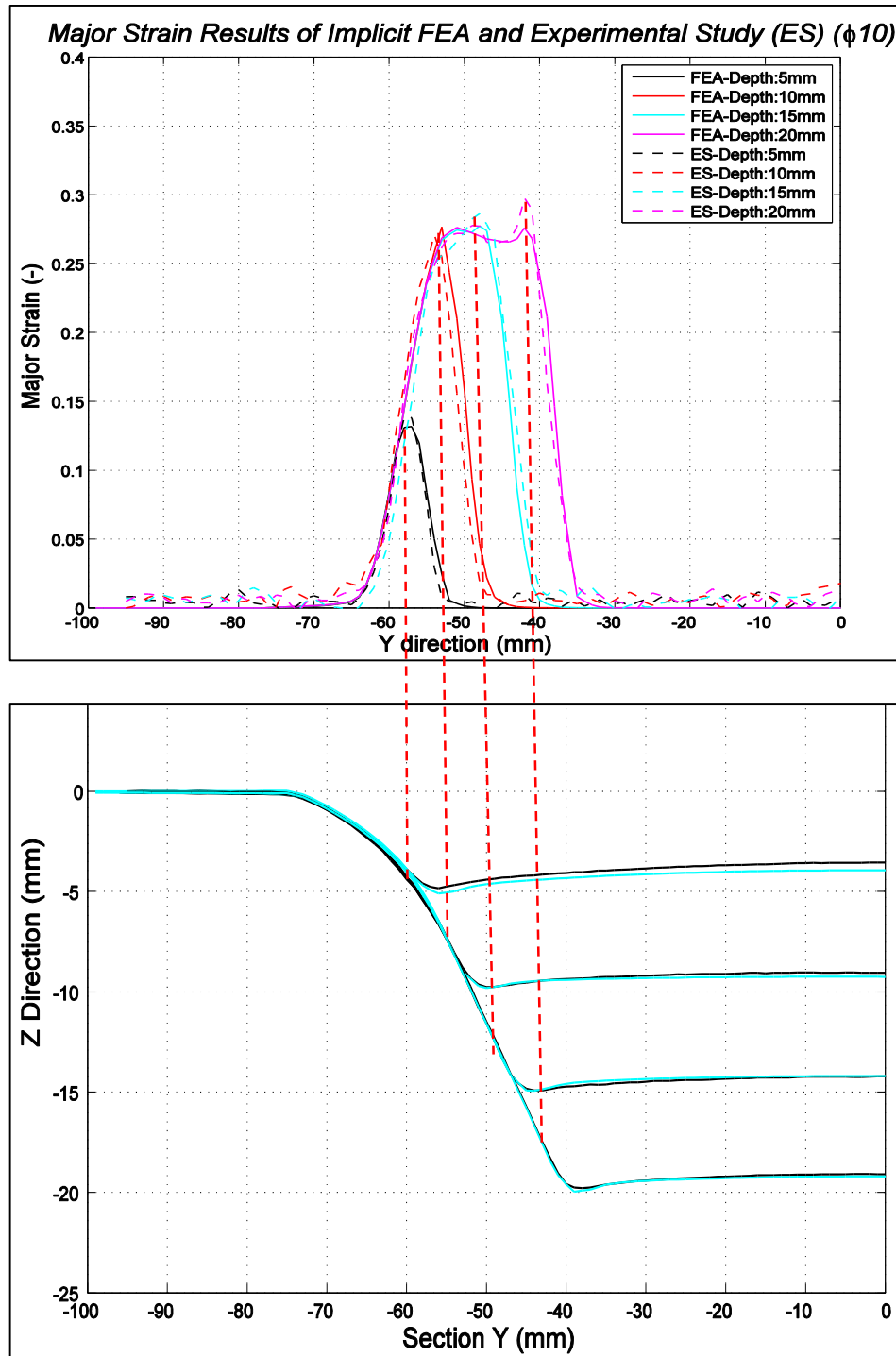
Figure 5.19 The major strain comparison with the geometric profiles at different depths through section along Y.
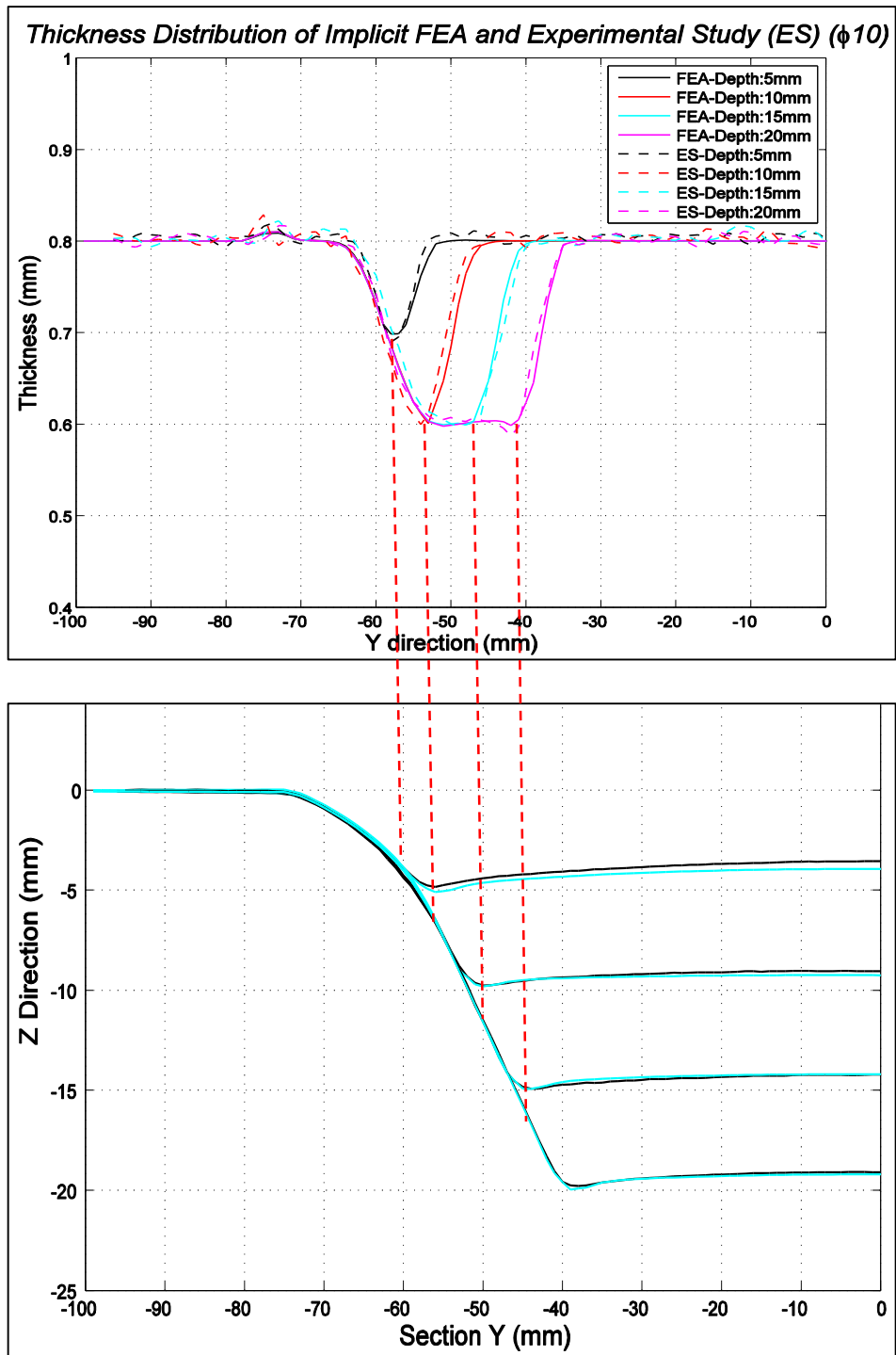
Figure 5.20 The thickness distribution comparison with the geometric profiles at different depths through section along Y.

Furthermore, the thickness distributions of implicit and experimental results are consistent. The variation of the thicknesses shows the same behavior as in major strain comparison. As the thickness value for 5 mm deep part is 0.69 mm, but the thicknesses are almost equal in 10 mm, 15 mm and 20 mm deep parts which are 0.6 mm.

5.2 Truncated Square Pyramid

As opposed to the truncated cone, truncated square pyramid has sharp corners on the lateral surface. Therefore, it is an appropriate case to assess the capabilities of ISF in case of sharp geometric features. The assessments have been made similar to the previous case using two orthogonal X and Y section profiles as shown in Figure 5.21. It was mentioned that the depth of the pyramid is 60 mm and the walls are at an angle of 60^0.
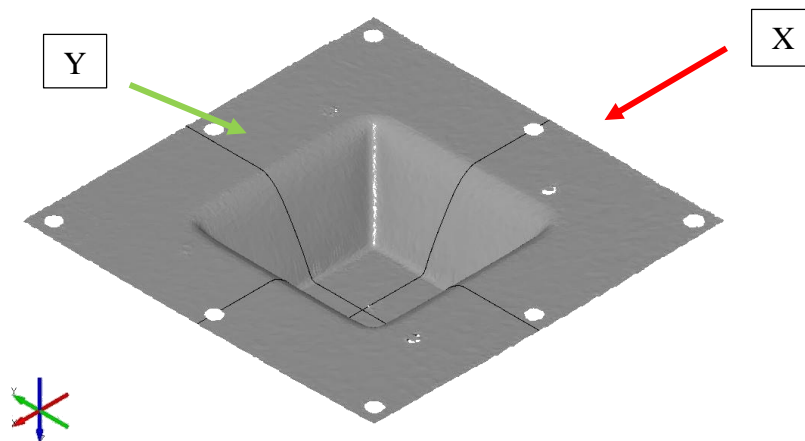
Figure 5.21 The surface of truncated square pyramid from optical measurement with the tool diameter of 10 mm.

In Figure 5.22, the comparison of geometrical profiles of 5 mm diameter tool, obtained from optical measurements and explicit analysis, are illustrated. The explicit analysis profile differs a maximum value of 6 mm from the optical measurement profile at the inclined wall alone section Y. It is worth mentioning that the reason for this relatively large difference is due to the fact that springback cannot be captured in explicit analysis. Furthermore, the optical and explicit profiles at the bottom and top bases are in a good agreement.
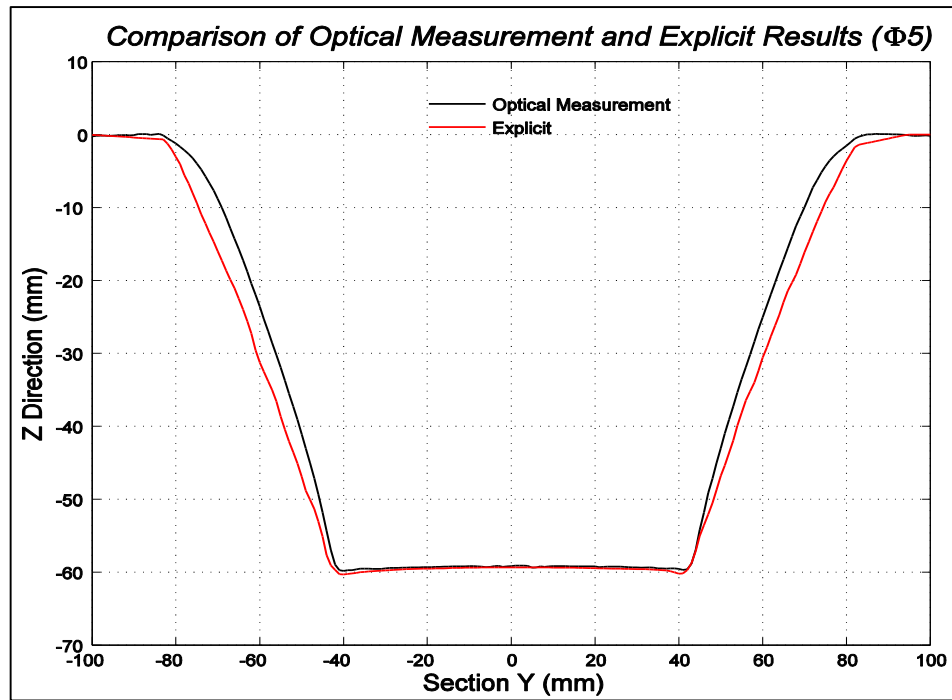
Figure 5.22 The geometrical comparison of optical measurement and explicit results for section along Y.

Additionally, as can be seen in Figure 4.23 (Top), the major strain comparison has been made. At right hand side of the graph, there is a loss in symmetry at explicit results. As mentioned before, this is due to the dynamic effects induced by the tool's acceleration and deceleration. The maximum error is about 13%.

In Figure 4.23 (Bottom), the thickness profiles are shown which are in good agreement. The explicit results are overestimating by approximately 6%, particularly at the edge of the flat surfaces. The final thickness is as expected which is about 0.4 mm.
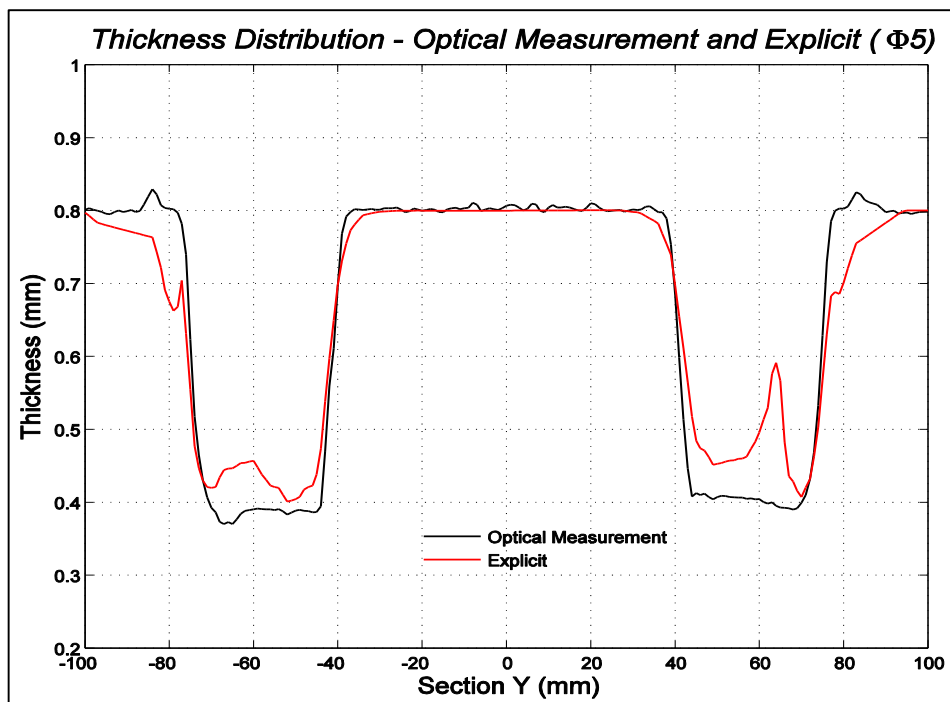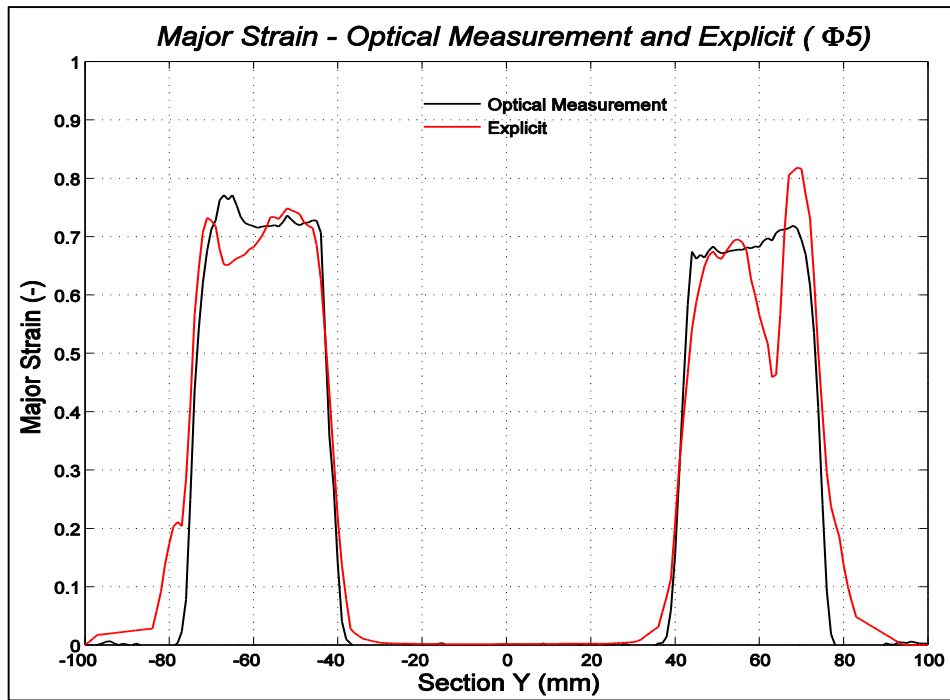
Figure 5.23 The major strain (Top) and thickness distribution (Bottom) comparisons of optical measurement and explicit results for section along Y.

The geometrical comparisons of 10 mm tool also shows good agreement. As can be seen in Figure 5.24, the dimensional accuracy is very well at the top and bottom bases, but deviates about 7 mm at the inclined wall.
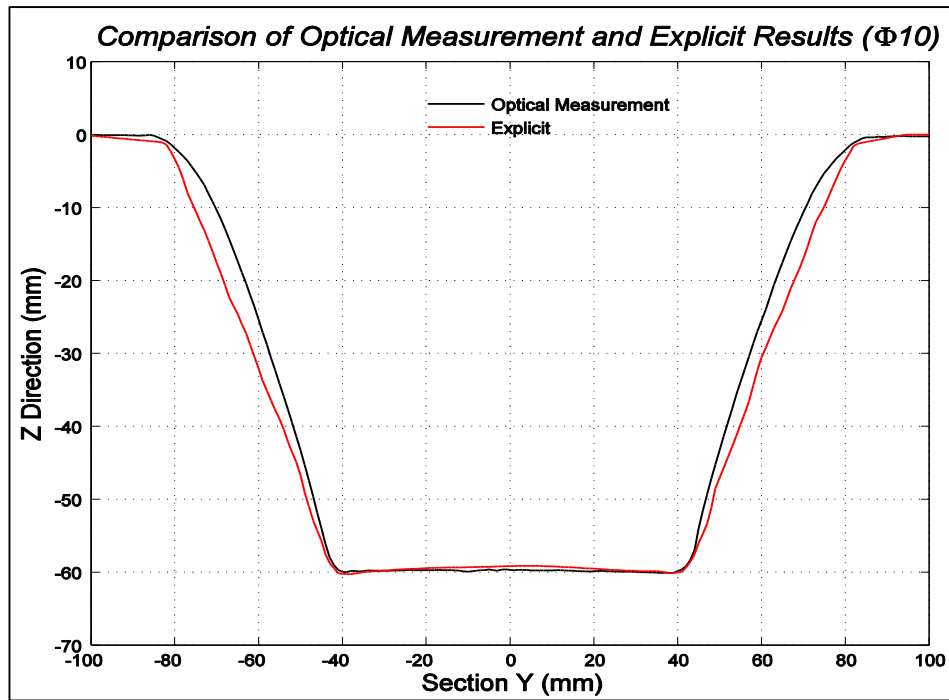
Figure 5.24 The geometrical comparison of optical measurement and explicit results for section along Y.

The major strain profiles show a good consistency as in Figure 5.25. The difference between the FEA result and experiment is about 6% at upper flat edges.
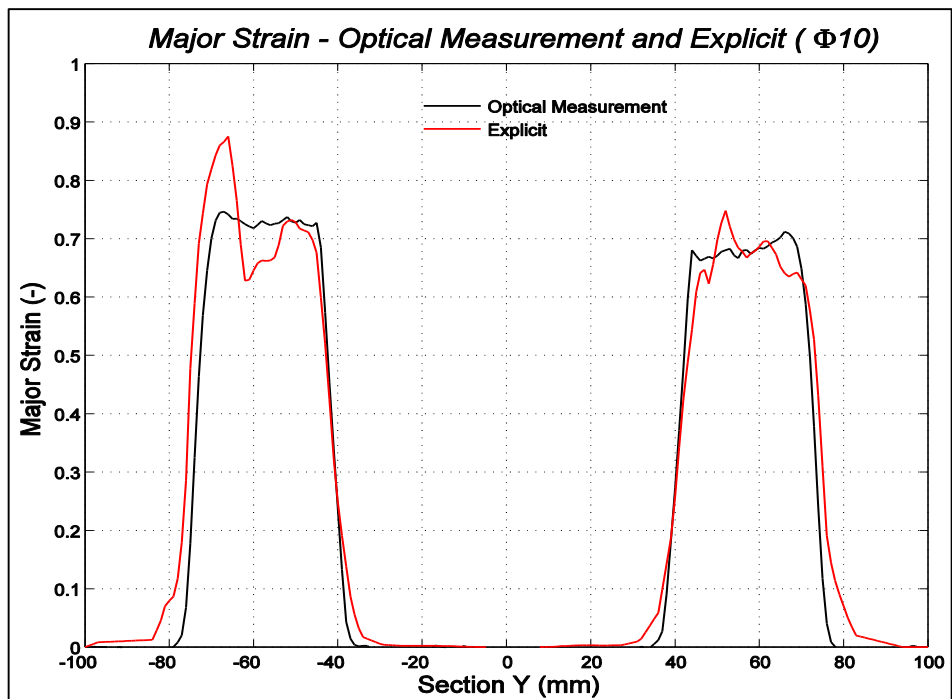
Figure 5.25 The major strain comparison of optical measurement and explicit results for section along Y.

It should be noticed, the discrepancies, in thickness distributions between the parts manufactured by using 5 mm and 10 mm diameter tools, are lower than 0.05 mm. The agreement on inclined wall is better than top base.
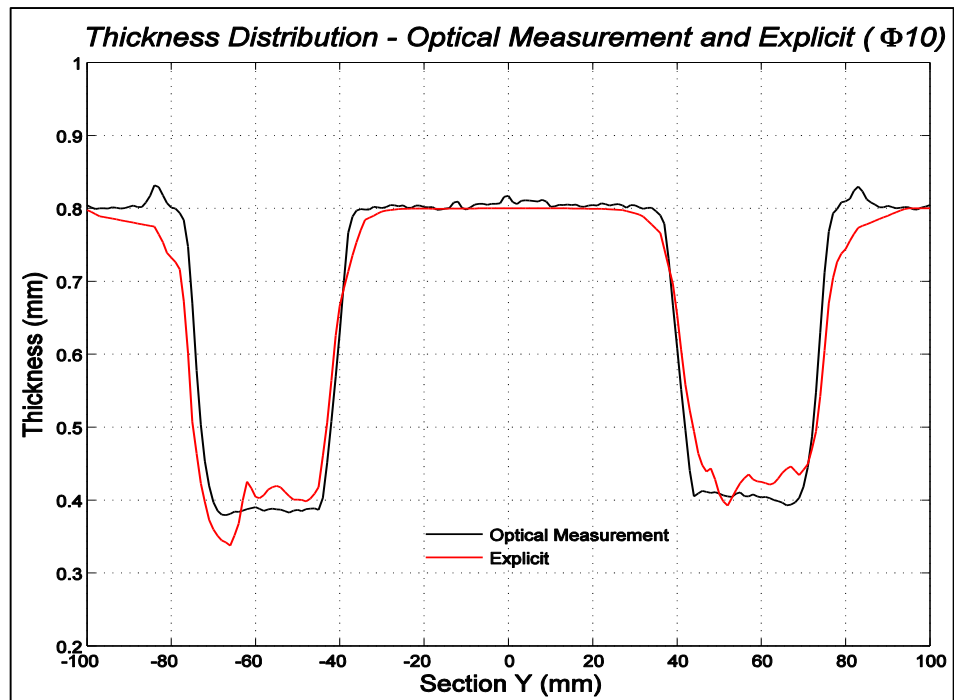
Figure 5.26 The thickness distribution of optical measurement and explicit results for section along Y.
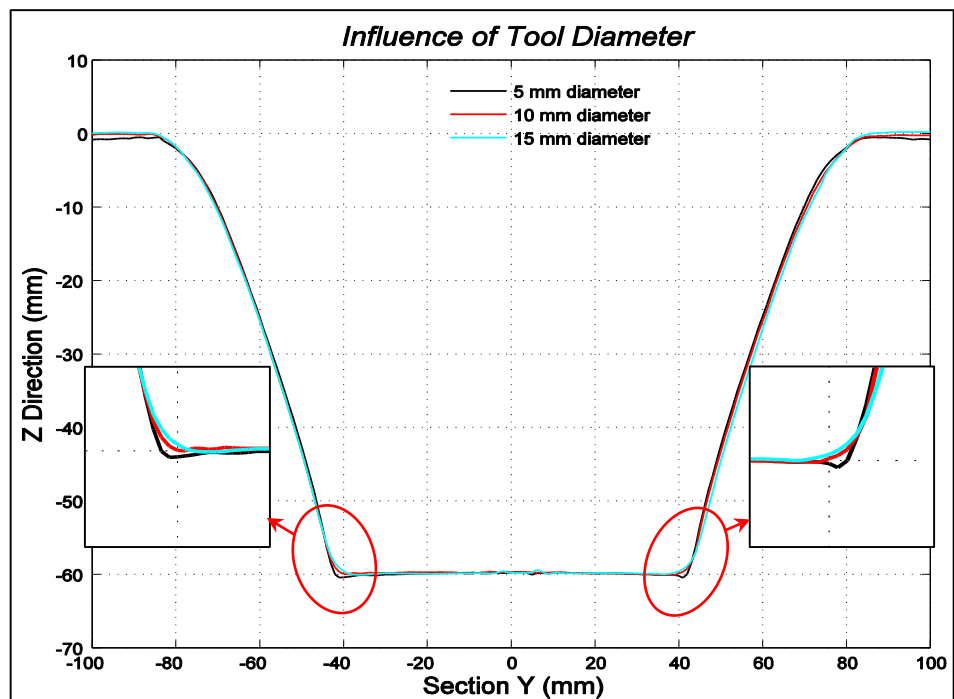
Figure 5.27 The geometrical profiles using 5 mm, 10 mm and 15 mm diameter tool.

In Figure 5.27, the geometric profiles of the truncated square pyramids, which are manufactured by 5 mm, 10 mm and 15 mm diameter tool, are shown. The results are similar to truncated cone's results.
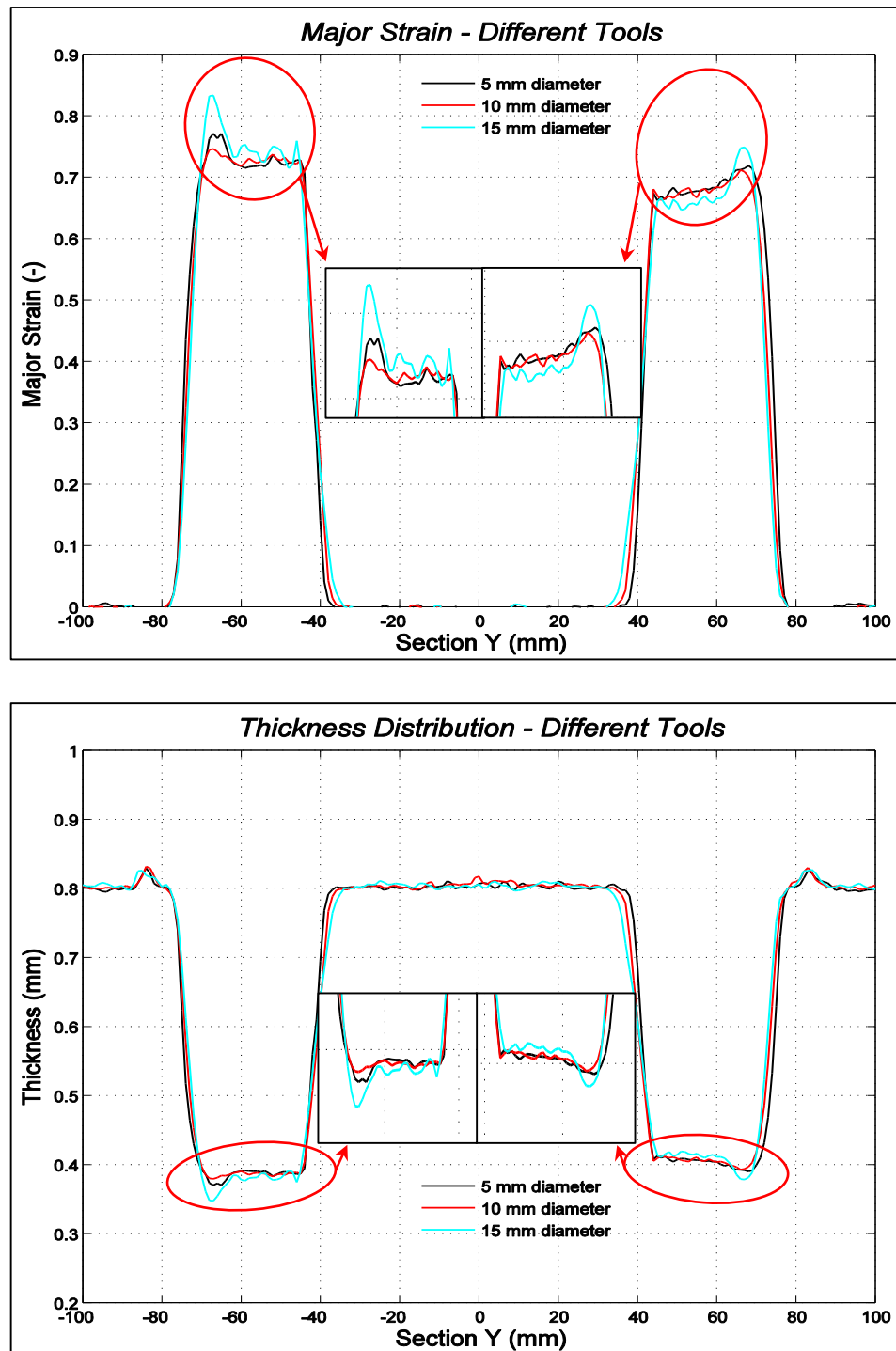
Figure 5.28 The major strain (Top) and thickness distribution (Bottom) comparisons.

To consider the compatibility between implicit and explicit results with respect to experimental results, a relatively smaller truncated square pyramid which has 20 mm

depth with the inclination of 40^0, is manufactured by 10 mm diameter tool. The bottom square has 120 mm x 120 mm dimension. The backing plate was same as in the first pyramidal shape trial.
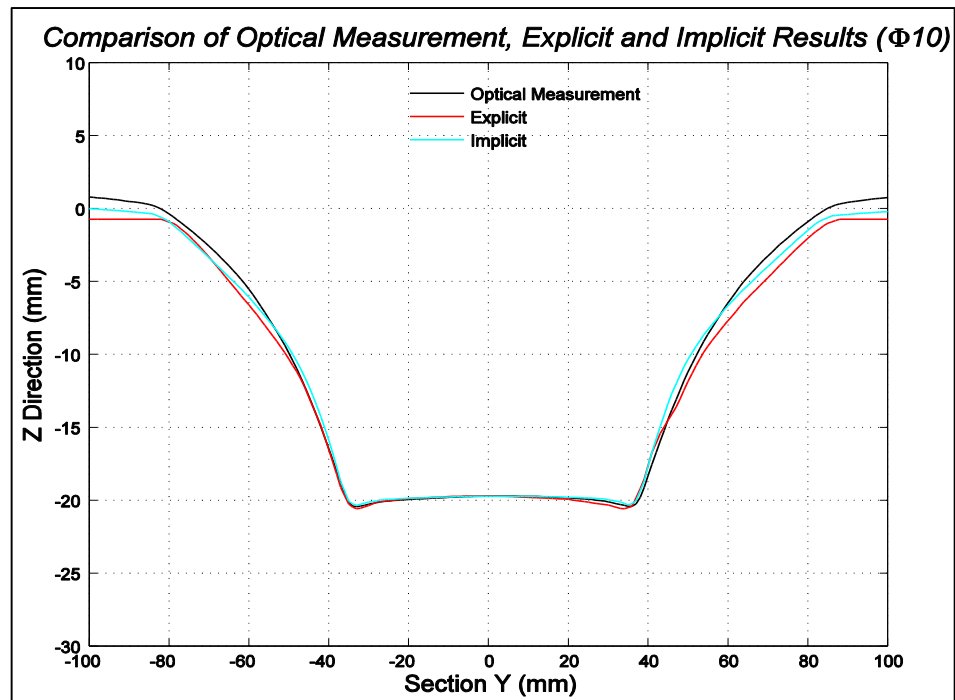
Figure 5.29 The geometrical comparison of optical measurement, explicit and implicit results for section along Y.

In Figure 5.29, the geometrical profiles are shown. At the inclined surface, the implicit and explicit analysis profiles differ from the optical measurement at a maximum value of 3 mm and 2 mm in Y section, respectively. In addition to this, the implicit and explicit profile deviate 0.8 mm and 1.1 mm from experimental profile in Z direction. On the other hand, the explicit and implicit profiles at the bottom base are in good agreement. But, the agreement failed on the top base. The difference is 0.22 mm in Z direction. As seen in the figure, the bottom base consistency is not good. This is most probably caused by the working area because the backing plate's working area is larger than the manufactured part's working area. Besides, the major strains and the thickness distributions are compared with optical measurement result. As seen in Figure 5.30 (Top), the implicit analysis and optical measurement have a good agreement. The deviation at the upper part of the curve in implicit analysis does not exceed 10%. The difference can be considered acceptable.

As seen in Figure 5.30 (Bottom), although the agreement between implicit analysis and optical results seem to be well, there are small deviations which are not exceeding 0.03 mm in thickness. However, the explicit results deviates much more from implicit and optical results.
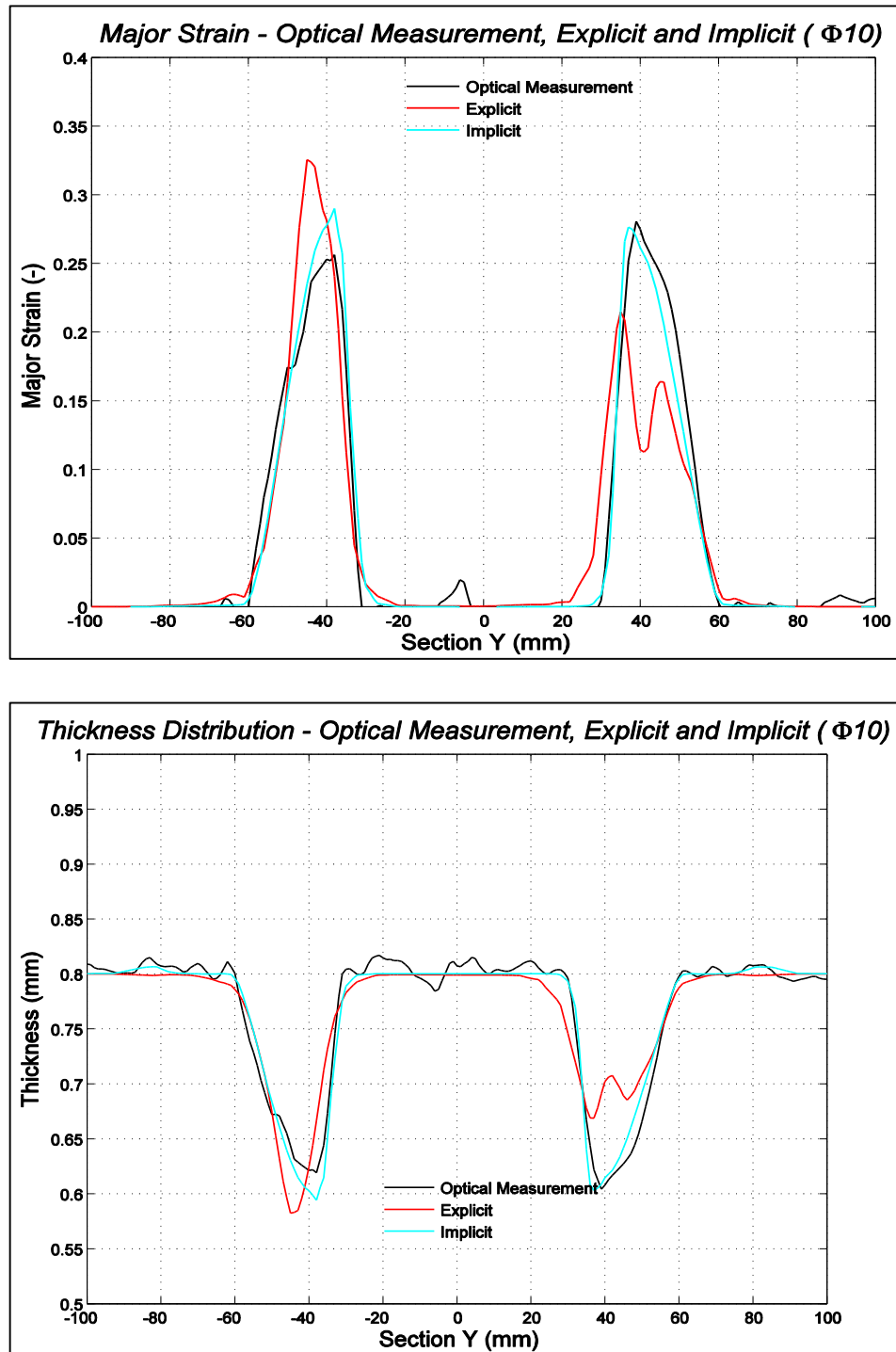
Figure 5.30 The major strain (Top) and the thickness distribution (Bottom) comparisons.

In Figure 5.31 and Figure 5.32 illustrate the results of major strain and the thickness distribution with implicit FEA in comparison with optical measurements. The illustration is same as in truncated cone part. The maximum value of major strain predicted by the FEA is 0.28, whereas the value is approximately 0.29 in optical measurement result for 20 mm deep part. Regarding to major strain values, the agreement is quite good in both cases. The same difference between optical and implicit results is observed in this part. The variation of major strain in 5 mm and 10 mm deep parts is higher than the other manufactured parts. Also, the major strain values are almost same in the parts which have 15 mm and 20 mm depths.

Furthermore, the thickness distributions of implicit and experimental results are consistent. The variation of the thicknesses shows the same behavior as in major strain comparison. While the thickness value for 5 mm deep part is 0.69 mm, for 10 mm deep part is 0.62 and the other parts' thickness is 0.6 mm.
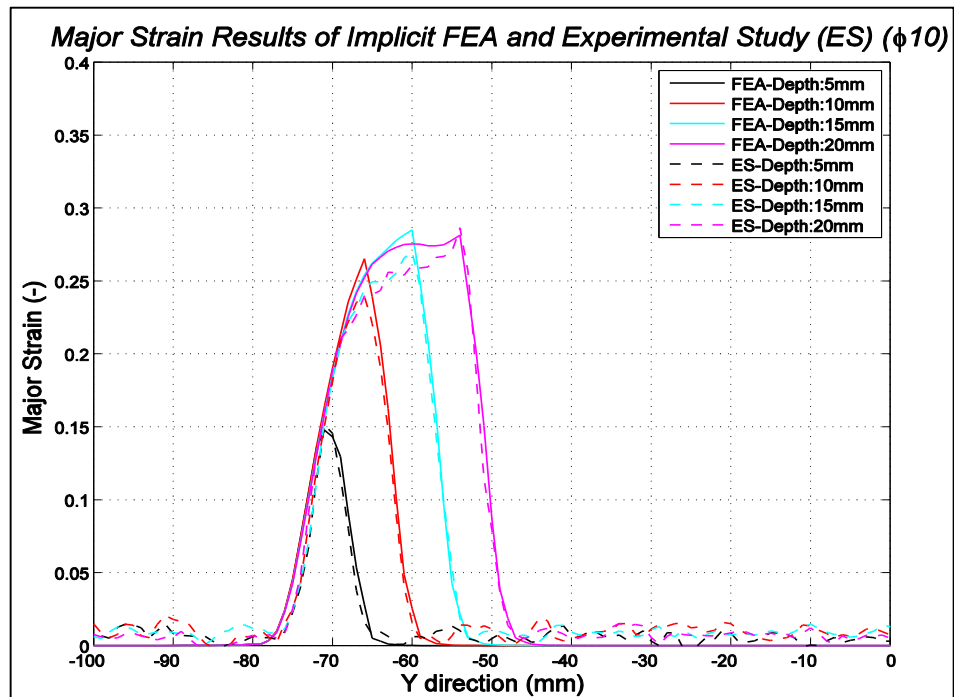
Figure 5.31 The major strain comparison of implicit analysis and optical measurement results at different depths through section along Y.

The findings can be interpreted as below:

- From the FEA view point, the behavior of the major strain does not remain constant with the increasing depth for square pyramid, however in truncated cones, there is not any increase at 10 mm, 15 mm and 20 mm deep parts. This behavior is similar for thickness distribution results.

- The experimental results of the truncated cones deviate from FEA most probably due to the measurement errors. Because, the grid size of truncated cones were larger than square pyramid. This could affect the accuracy of the measurement.

- The curve's shape for 15 mm and 20 mm deep parts resembles to a knife in truncated square pyramids. This may be caused by the deformation behavior at the lateral corners. On the other hand, the curve resembles to a dimpled hill which caused by deformation mode of truncated cones
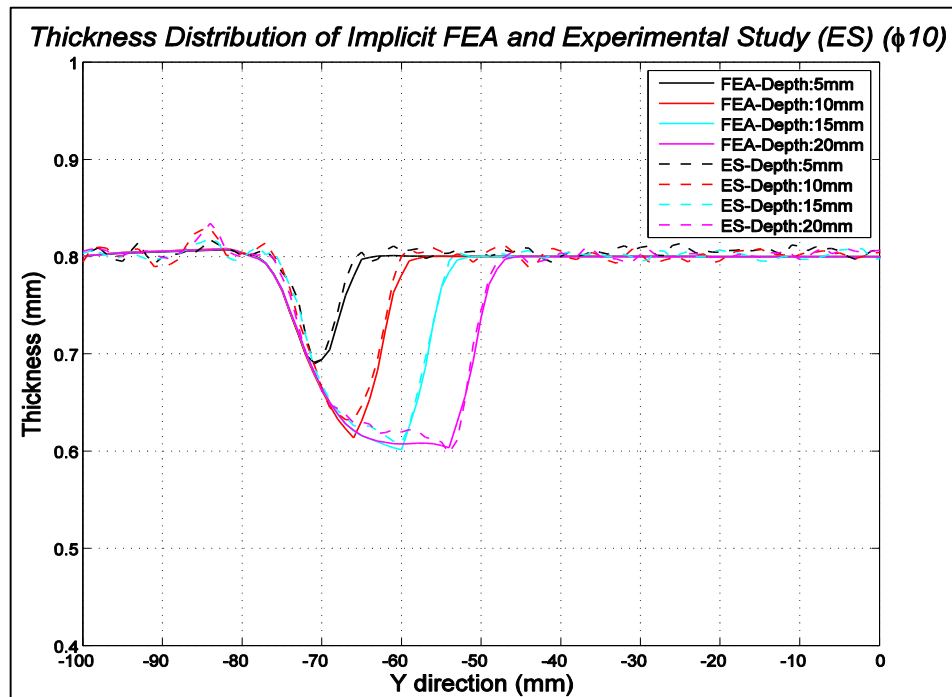
Figure 5.32 The thickness distribution of implicit analysis and optical measurement results at different depths through section along Y.

5.3 Real Car Component

Based on the results presented in the previous discussions, it is concluded that explicit FE models developed in previous sections can be applied for final geometry prediction in ISF. To assess the potential use of explicit FE for tool path identification/optimization in real ISF processes, manufacturing of a Fiat Doblò part is considered. The CAD drawing of the component was given in previous chapters. When compared with the previous examples, the geometry is relatively complex, especially due to steep side walls, reaching approximately 90 degrees of inclination. For the first manufacturing iteration a single-stage tool path is considered. The tool path is evaluated using the explicit model. However, as mentioned in Chapter 4.1, the trial for single step has failed. Then, multi-stage forming has conducted. The tool used in manufacturing the real car component has 10 mm diameter.

First, the geometrical comparisons between explicit analysis and experimental results have been made. Since the part is asymmetric the assessments have been done along section X and section Y. Figure 5.33 illustrates the sections through the X and Y.
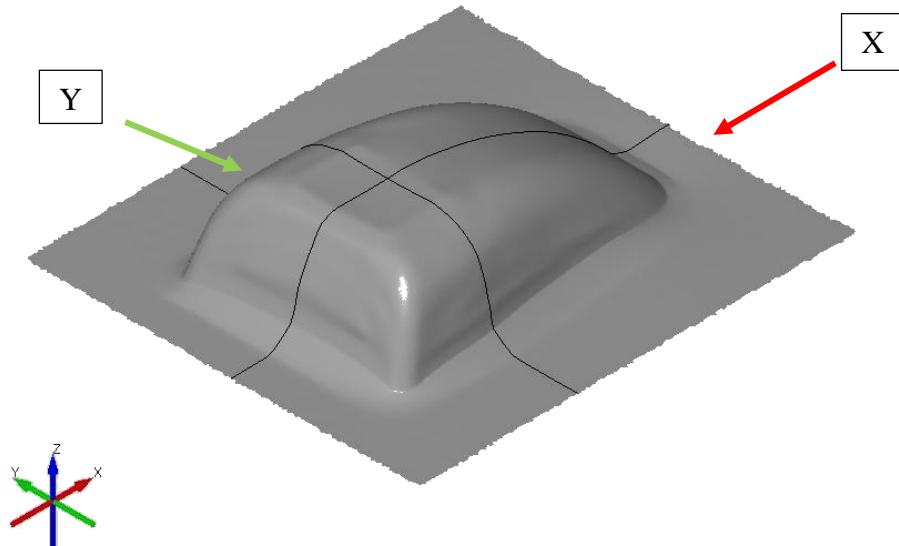
Figure 5.33 The surface of real car component from optical measurement with the tool diameter of 10 mm.

Figure 5.34 demonstrates the geometrical comparisons of section-Y and section-X. When section-Y is analyzed, the explicit analysis profile are almost identical with experimental profile. The difference between them does not exceed 0.9 mm at inclined

walls. However, at the bottom base the difference is about 6 mm in the direction of Y section and 4 mm in the direction of Z. When section-X is analyzed, the agreement in both geometrical profiles are quite good. However, there is a minor inconsistency on the top base. As mentioned before, this is almost certainly caused by the final indentation of the tool before the end of the explicit analysis. The deviation from optical measurement profile does not exceed 2mm in Z direction. The difference at the bottom base can also be explained the movement of the tool in which the tool starts to indent.
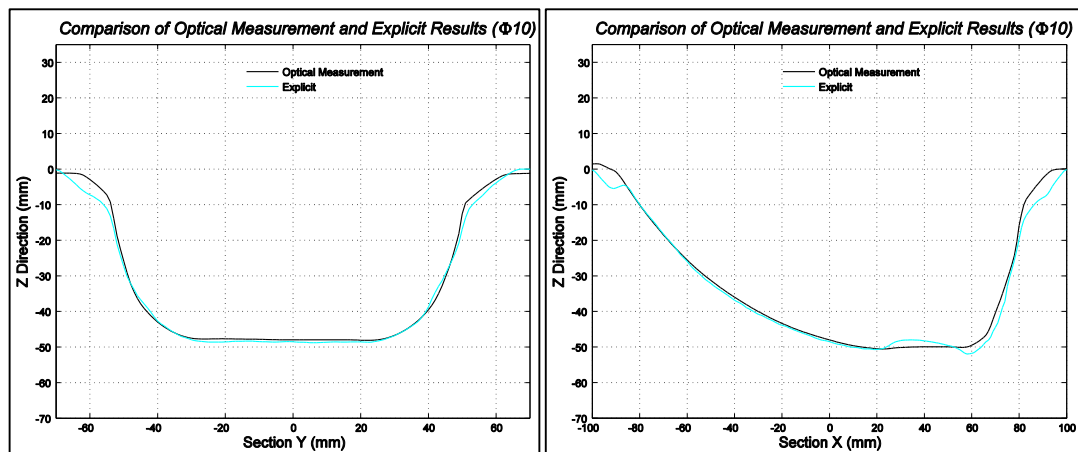
Figure 5.34 The geometrical comparison of optical measurement and explicit results for section along Y (Left) and section along X (Right).

The major strain comparisons have been investigated as well. At first sight, though the profiles has an agreement, there are some differences in both sections. The difference is approximately 15% at section-Y and 7% at section-X in terms of major strains.
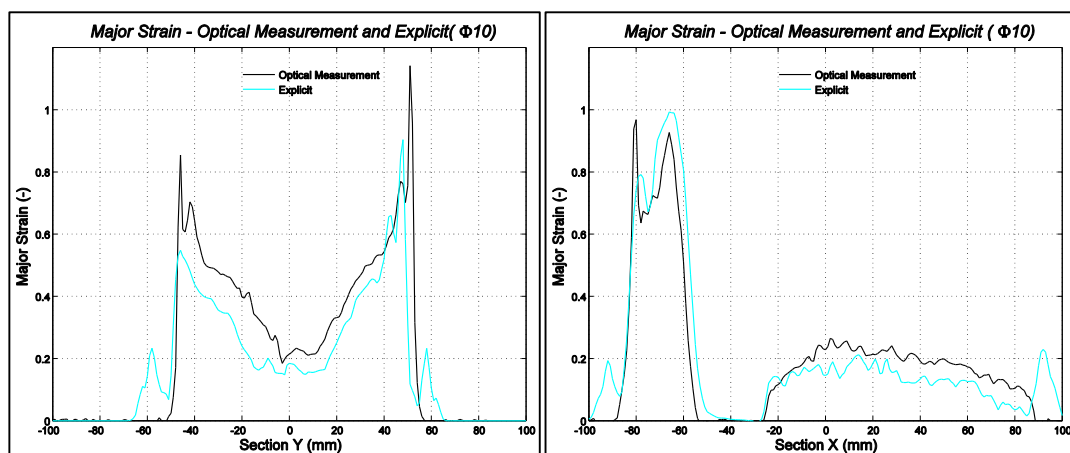
Figure 5.35 The major strain comparisons of optical measurement and explicit results for section along Y (Left) and section along X (Right).

Furthermore, the thickness distribution analysis have been carried out. As can be seen in Figure 5.36, both sections' profiles are consistent with experimental results. However, there is a difference between explicit analysis and experimental results which is about 0.1 mm at section Y and 0.13 mm at bottom flat base in section X in terms of thickness.
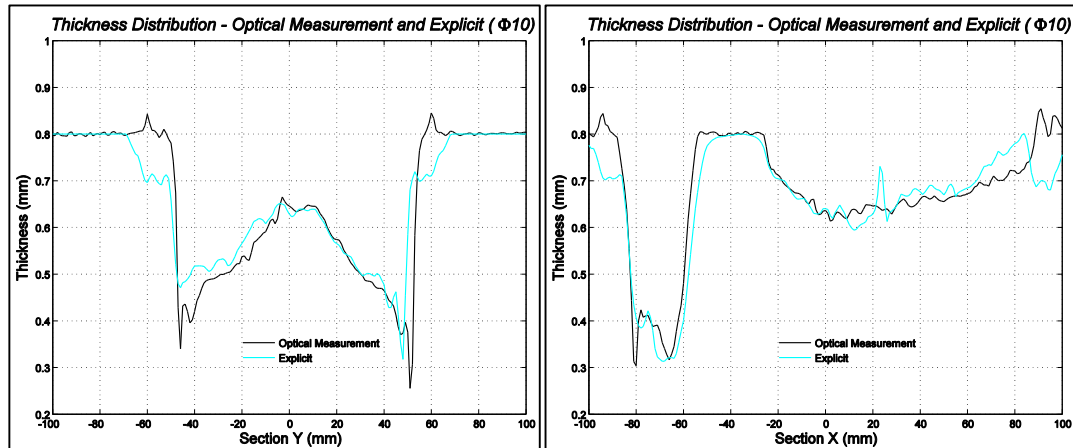
Figure 5.36 The comparison of thickness distribution of optical measurement and explicit results for section along Y (Left) and section along X (Right).

As a result of this subsection, although the explicit analysis is not fully identical with experimental results, in order to investigate the geometric accuracy it can be preferable due to the less process time compared to implicit analysis.

5.4 Case Study

In order to investigate the competitiveness of the ISF and the deep drawing process, the real car component was manufactured both with ISF and deep drawing process. Before manufacturing, the blanks are etched, as in the previous studies, in order to measure the geometrical accuracy, deformation behavior and thickness distribution.

5.4.1 The Comparison of the Real Car Component in ISF and Deep Drawing Process

For a preliminary preparation the blanks are etched by using electropolishing system with the stencil, in which the dots have 2 mm point to point distance. In Figure 5.37,

99

the manufactured die setup is displayed which is mounted on the Schuler Hydraulic
Press with the capacity of 400 tones.

Figure 5.37 The die setup for deep drawing of the real car component.

The blankholder force is 35 kN and the punch force is 65 kN. The manufactured part
is shown in Figure 5.38.

Figure 5.38 The manufactured part by deep drawing operation.

The real car component is also manufactured using ISF process in 3-axes CNC milling
machine with the tool having 10 mm radius. The ISF setup was shown in Figure 4.8.

After completion of the manufacturing process the parts are measured with optical measurement system. The surface, strain and the thickness distributions are obtained.

Firstly, the geometrical profiles are compared with the CAD data in order to see dimensional compatibility. As can be seen in Figure 5.39, the profiles are almost identical with each other. ISF profile deviates from CAD with the value of 1.6 mm at the inclined walls in Y section and with the value of 1.5 mm in X section. The deep drawn profile is more consistent with CAD profile as compared to ISF profile since the springback is much more in ISF process.
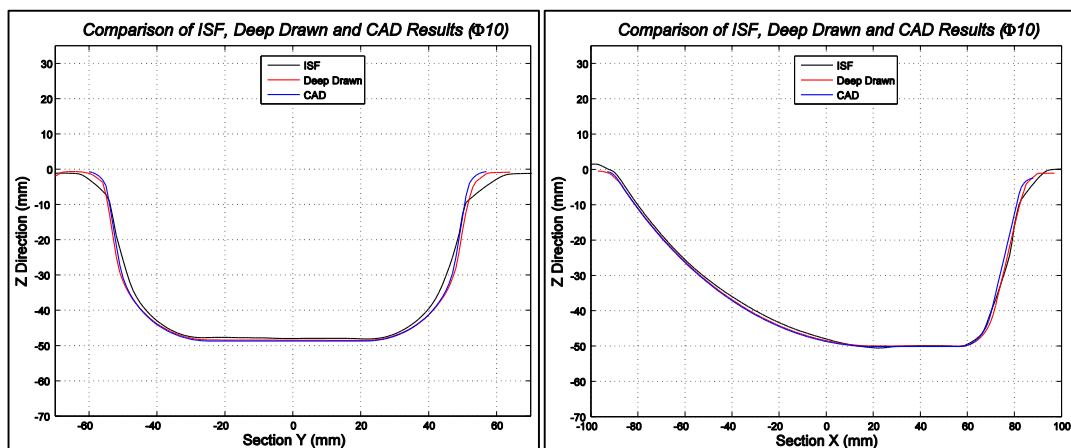
Figure 5.39 The results of geometrical comparison through along Section-Y and Section-X.

Secondly, the major strains are compared. In Figure 5.40, it is observed that the major strain profile of ISF process spreads over a larger area than deep drawing process. It is expected since the formability reaches to higher strains in ISF process. Also, the strain distribution shows a homogeneity in deep drawing process since in ISF process has a localized deformation. The maximum major strain value in ISF is 1.14 at section-Y and 0.97 at section-X. However, the maximum value is 0.21 at section-Y and 0.19 at section-X in deep drawn part.
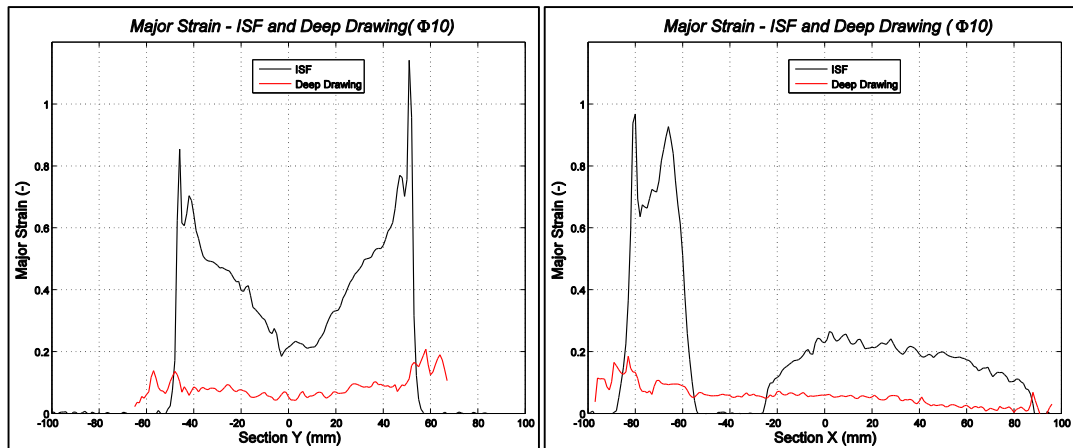
Figure 5.40 The major strain comparison of two processes.
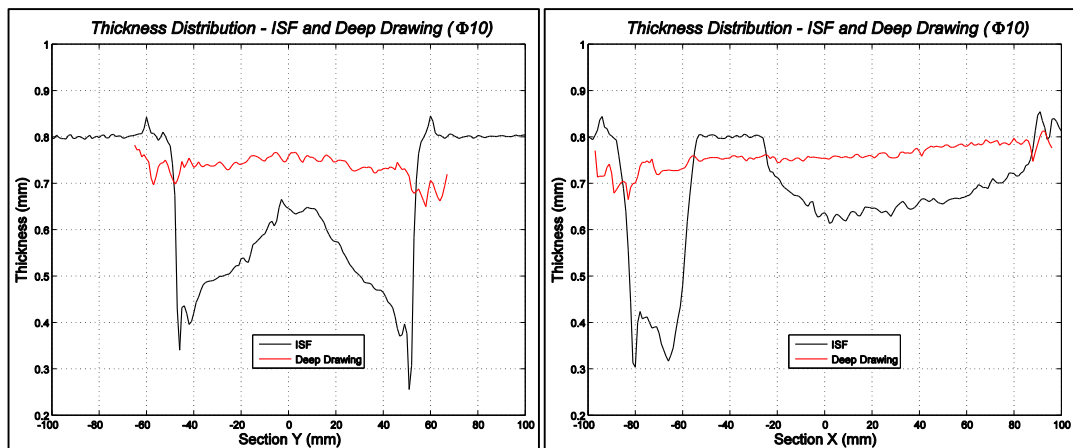
Figure 5.41 The thickness comparison of two processes.

The thickness distributions are shown in Figure 5.41. As seen in the figure, the part manufactured by ISF process has an excessive thinning when compared to deep drawing process. The thinning at ISF part reaches to 0.26 mm at section-Y and 0.3 mm at section-X and the thinning at deep drawn part reaches to 0.65 mm at section-Y and 0.66 mm at section-X.

CHAPTER 6

CONCLUSION AND DISCUSSION

Incremental sheet forming (ISF) process has been a developing process and a subject for a large volume of research over the twenty years. This process has a notable increasing interest for researchers mainly because it provides enhanced formability and flexibility. Also, the process attracts considerable attention in prototype manufacturing due to its flexible nature and reduced manufacturing costs in low volumes.

The motivation of this study is to investigate the process parameters of ISF, in order to provide tools for selecting proper tool path strategies for manufacturing simple geometries as well as complex parts. For this, the compatibility of numerical models and experiments are investigated, starting from basic geometries to complicated shapes. Further, in order to compare the deformation behavior of ISF with that of the deep drawing process, the parts that are manufactured by both methods are measured optically and several comparisons concerning geometrical tolerances, deformation behavior and thickness distribution are made.

Within this scope, firstly, a proper material characterization for FeP04 mild steel is carried out by performing standard tensile test, HBT and FLD test. The findings are summarized below:

- The tensile tests are conducted in rolling, diagonal and transverse directions. The flow curves are almost overlapped, thus the material is assumed to be isotropic.
- To obtain flow curve, which is used in FEA for an accurate model, the combination of tensile test and HBT data are used. The stack compression test

is not used since the curve trend do not converge a parallel line at higher strains in strain direction.

- In ISF process the forming limits are higher than conventional forming process limits. The FLD test is performed in order to observe the deformation behavior, no tearing occurs whether the strain values exceed the traditional FLD.

After executing the material characterization tests, ISF process is modeled using FE software with obtained material properties. Meanwhile, the parts are manufactured and optical measurements are carried out. Optical measurements are performed with 3D coordinate measurement and forming analysis systems. Firstly, two different conditions for simple parts, manufacturing by using different tools and manufacturing to different depths, have been investigated. Later, the real car component is manufactured with 10 mm diameter tool. After numerical and experimental studies, the FEA and experiments are compared in terms of geometrical accuracy, major-minor strain and thickness distribution. The results are consistent with each other. The conclusions are given below:

- The ability of manufacturing the complicated sheet metal products by means of ISF requires accurate tool path strategy. In addition to this, the process parameters such as feedrate, step width and lubrication have a great importance since there is a localized deformation in ISF.

- The experiments considered in this study are conducted to validate the numerical and experimental results.

- Owing to validation of the results, it is concluded that the implicit analysis results are almost identical with experiments in terms of geometry, deformation behavior and thickness distribution.

- The deformation mechanism of ISF is assumed to be plane strain tension at truncated cones' surface and at lateral surfaces of pyramidal shapes, thus it is experimentally shown that ISF has a deformation mode which is very close to plane strain tension. Moreover, on lateral corners at square pyramid, the deformation mode is biaxial stretching.

- Although the strain value reaches to higher values, there is no crack occurrence; which means the formability limits in ISF is much higher than traditional sheet forming processes.

- Using larger tools (in diameter) causes the distribution of the strains over an extended area which makes the process similar to traditional forming process.

- Explicit analysis is relatively fast and gives accurate results especially for estimating the component geometry.

- Although implicit analysis gives accurate results both in terms of geometry and deformation behavior, the computational time is so high.

Finally, when a part to be manufactured by ISF, if desired, the given procedure below should be followed:

➢ To check whether the part has steeper walls or not.

➢ If the part is simple and has no steep walls, then single step tool path should be used.

➢ If the part has steeper walls, then multi stage tool path should be used.

➢ After determining the tool path, the part is manufactured. Meanwhile, the coordinate data is generated from tool path algorithm in order to use this as a boundary condition in FEA software.

➢ Explicit analysis should be used to obtain the geometry of the part due to its lower computational time as compared to implicit analysis.

➢ Implicit analysis should also be used to obtain the geometry of the part and accurate deformation behavior.

REFERENCES

[1] de Brito Camara, J.L.P., Single Point Incremental Forming, MSc Thesis, Mechanical Engineering Department, Universidade Tecnica de Lisboa, 2009.

[2] Jeswiet, J., Micari, F., Hirt, G., Bramley, A., Duflou, J., Allwood, J., Asymmetric Single Point Incremental Forming of Sheet Metal, CIRP Annals - Manufacturing Technology, Volume 54, Issue 2, 2005, Pages 88–114.

[3] Tamer, M. E., Music, O., Ozdemir, I., Baranoglu, B., Sakin, A., Durgun, I., Simulation for Incremental Sheet Forming Process: a Comparison of Implicit and Explicit Finite Element Analysis with Experimental Data, 7th International Conference and Exhibition on Design and Production of Machines and Dies/Molds, June 2013.

[4] Leszak, E. Patent US3342051A1, published 1967-09-19. Apparatus and Process for Incremental Dieless Forming.

[5] Nakagawa, T., Advances in Prototype and Low Volume Sheet Forming and Tooling, Journal of Materials Processing Technology, Volume 98, Issue 2, 29 January 2000, Pages 244–250.

[6] Silva, M.B., Skjoedt, M., Martins, P.A.F., Bay, N., Revisiting the Fundamentals of Single Point Incremental Forming by means of Membrane Analysis, International Journal of Machine Tools and Manufacture, Volume 48, Issue 1, July 2007, Pages 73–83.

[7] Micari, F., Ambrogio, G., Filice, L., Shape and Dimensional Accuracy in Single Point Incremental Forming: State of the Art and Future Trends, Journal

of Materials Processing Technology, Volume 191, Issue 1-3, 2007, Pages 390–395.

[8] Emmens, W.C., van den Boogaard, A.H., An Overview of Stabilizing Deformation Mechanism in Incremental Sheet Forming, Journal of Materials Processing Technology, Volume 209, Issue 8, 2009, Pages 3688–3695.

[9] Emmens, W.C., van der Weijde, D.H., van den Boogaard, A.H., The FLC, Enhanced Formability, and Incremental Sheet Forming, International Deep Drawing Research Group, Issue 1–3, June 2009, Golden, USA.

[10] Emmens, W.C., van den Boogaard, A.H., Tensile Tests with Bending: a Mechanism for Incremental Forming, International Journal of Material Forming, April 2008, Volume 1, Issue 1 Supplement, Pages 1155–1158.

[11] Bambach, M., Hirt, G., Junk, S., Modelling and Experimental Evaluation of the Incremental CNC Sheet Metal Forming Process, 7th International Conference on Computational Plasticity, 2003.

[12] Jackson, K., Allwood, J., Landert, M., Incremental Forming of Sandwich Panels, Journal of Materials Processing Technology, 2008I Volume 204, Issue 1-3, Pages 290–303.

[13] Jackson, K., Allwood, J., The Mechanics of Incremental Sheet Forming, Journal of Materials Processing Technology, Volume 209, 2009, Pages 1158–1174.

[14] Eyckens, P., Moreau, J.D., Duflou, J., van Bael, A., van Houtte, P., MK Modelling of Sheet Formability in the Incremental Sheet Forming Process, Taking into account Through Thickness Shear, International Journal of Material Forming, August 2009, Volume 2, Issue 1 Supplement, Pages 379–382.

[15] Silva, M.B., Skjoedt, M., Atkins, A.G., Bay, N., Martins, P.A.F., Single Point Incremental Forming and Formability Failure Diagrams, The Journal of

Strain Analysis for Engineering Design, 01/2008, 43(1):15-35, DOI:10.1243/03093247JSA340.

[16] Skjoedt, M., Silva, M.B., Martins, P.A.F., Bay, N., Strategies and Limits in Multistage Single Point Incremental Forming, The Journal of Strain Analysis for Engineering Design, 01/2010, 45(1):33-44, DOI:10.1243/03093247JSA574.

[17] Filice, L., Fratini, L., Micari, F., Analysis of Material Formability in Incremental Forming, Cirp Annals-Manufacturing Technology, 01/2002, 51(1):199-202, DOI:10.1016/S0007-8506(07)61499-1.

[18] Kwiatkowski, L., Urban, M., Sebastiani, G., Tekkaya, A.E., Tooling Concepts to Speed up Incremental Sheet Forming, Production Engineering, February 2010, Volume 4, Issue 1, pp 57-64.

[19] Duflou, J.R., Verbert, J., Belkassem, B., Gu, J., Sol, H., Henrard, C., Habraken, A.M., Process Window Enhancement for Single Point Incremental Forming Through Multi-step Tool Paths, CIRP Annals - Manufacturing Technology Volume 57, Issue 1, 2008, Pages 253–256.

[20] Hamilton, K., Jeswiet, J., Single Point Incremental Forming at High Feed Rates and Rotational Speeds: Surface and Structural Consequences, CIRP Annals - Manufacturing Technology, Volume 59, Issue 1, 2010, Pages 311–314.

[21] Hagan, E., Jeswiet, J., A Review of Conventional and Modern Single Point Sheet Metal Forming Methods, Proceedings of the Institution of Mechanical Engineers, Part B, Journal of Engineering Manufacture, 2003, Volume 217, n°2, Pages 213-225.

[22] Hirt, G., Ames, J., Bambach, M., Kopp, R., Forming Strategies and Process Modelling for CNC Incremental Sheet Forming, CIRP Annals - Manufacturing Technology, Volume 53, Issue 1, 2004, Pages 203–206.

[23] Bambach, M., A Geometrical Model of the Kinematics of Incremental Sheet Forming for the Prediction of Membrane Strains and Sheet Thickness, Journal of Materials Processing Technology,

Volume 210, Issue 12, 1 September 2010, Pages 1562–1573.

[24] Bambach, M., Araghi, B.T., Hirt, G., Strategies to Improve the Geometric Accuracy in Asymmetric Single Point Incremental Forming, Production Engineering, June 2009, Volume 3, Issue 2, Pages 145-156.

[25] Ambrogio, G., De Napoli, L., Filice, L., A Novel Approach Based on Multiple Back-Drawing Incremental Forming to Reduce Geometry Deviation, International Journal of Material Forming, August 2009, Volume 2, Issue 1 Supplement, Pages 9–12.

[26] Attanasio, A., Ceretti, E., Giardini, C., Optimization of Tool Path in Two Point Incremental Forming, Journal of Materials Processing Technology, Volume 177, Issues 1–3, 3 July 2006, Pages 409–412.

[27] Ham, M., Jeswiet, J., Dimensional Accuracy of Single Point Incremental Forming, International Journal of Material Forming, April 2008, Volume 1, Issue 1 Supplement, Pages 1171-1174.

[28] Dejardin, S., Thibaud, S., Gelin, J.C., Finite Element Analysis and Experimental Invesitgations for Improving Precision in Single Point Incremental Sheet Forming Process, International Journal of Material Forming, April 2008, Volume 1, Issue 1 Supplement, Pages 121-124.

[29] Dejardin, S., Thibaud, S., Gelin, J.C., Michel, G., Experimental Investigations and Numerical Analysis for Improving Knowledge of Incremental Sheet Forming Process for Sheet Metal Parts, Journal of Materials Processing Technology, Volume 210, Issue 2, 19 January 2010, Pages 363–369.

[30] Rosalbino, F., Scavino, G., Mortarino, G., Angelini, E., Lunazzi, G., EIS Study on the Corrosion Performance of a Cr(III)-Based Conversion Coating on

Zinc Galvanized Steel for the Automotive Industry, Journal of Solid State Electrochemistry, 15 (4): 703-709.

[31] Lange, K., Handbook of Metal Forming, Society of Manufacturing Engineers, McGraw-Hill, Inc., 1985, First Edition, Part 4.1, p. 40–56.

[32] Marciniak, Z., Duncan, J.L., Hu, S.J., Mechanics of Sheet Metal Forming, Butterworth-Heinemann, 2002, p.2, p.31.

[33] Wagoner, R. H., Chenot, J.-L., Fundamentals of Metal Forming, John Wiley&Sons Inc., 1997, p.3, p.5.

[34] Banabic, D., Sheet Metal Forming Processes, Springer, ISBN 978-3-540-88112-4, DOI 10.1007/978-3-540-88113-1 p. 152-179.

[35] Koç, M., Billur, E., Cora, Ö. N., An Experimental Study on the Comparative Assessment of Hydraulic Bulge Test Analysis Methods, Materials & Design, Volume 32, Issue 1, January 2011, Pages 272–281.

[36] Mutrux, A., Hochholdinger, B., Hora, P., A Procedure for the Evaluation and Validation of the Hydraulic Biaxial Experiment, Numisheet-International Conference, 2008, Pages 67–72.

[37] Gutscher, G., Wu, H. C., Ngaile, G., Altan, T., Determination of Flow Stress for Sheet Metal Forming Using the Viscous Pressure Bulge (VPB) Test, Journal of Materials Processing Technology, Volume 146, Issue 1, 15 February 2004, Pages 1–7.

[38] Altan, T., Palaniswamy, H., Bortot, P., Mirtsch, M., Heidl, W., Bechtold, A., Determination of Sheet Material Properties Using Biaxial Bulge Tests, Proceedings of the 2nd In. Conference on Accuracy in Forming Technology, Germany, 2006, ISBN: 3-937524-45-2, Pages 79–92.

[39] Volk, W., Heinle, I., Grass, H., Accurate Determination of Plastic Yield Curves and an Approximation Point for the Plastic Yield Locus With the Bulge Test, ICTP 2011, Pages 799–804.

[40] Banabic, D., Bunge, H.-J., Pöhlandt, K., Tekkaya, A.E., Formability of Metallic Materials, Springer, 2000, ISBN 3-540-67806-5, p. 189-191.

[41] Pöhlandt, K., Material Testing for the Metal Forming Industry, Springer, ISBN 978-3-642-50243-9 DOl 10.1007/978-3-642-50241-5 1989, p. 135.

[42] Hosford, W., Caddell, R., Metal Forming Mechanics and Metallurgy, Third Edition, Cambridge University Press, ISBN 13 978-0-511-35453-3, 2007, p. 237.

[43] Wagoner, R. H., Chenot, J.-L., Metal Forming Analysis, Cambridge University Press, 2001, ISBN 0-521-64267-1, p.198.

[44] Aramis User Manuel, Braunschweig, Germany, 2009, Part-2, Pages 5–11.

[45] Fish, J., Belytschko, T., A First Course in Finite Elements, John Wiley&Sons, Ltd, 2007, ISBN 978-0-470-03580-1, p. 1.

[46] Belytschko, T., Liu, W.K., Moran, B., Nonlinear Finite Elements for Continua and Structures, John Wiley&Sons, Ltd, 2000, ISBN 0-471-98773-5, Pages 3–25.

[47] Bambach, M., Hirt, G., Error Analysis in Explicit Finite Element Analysis of Incremental Sheet Forming, AIP Conference Proceedings, May 2007, Volume 908, Issue 1, Page 859.

[48] Hadoush, A., van den Boogaard, A.H., Efficient Implicit Simulation of Incremental Sheet Forming, International Journal for Numerical Methods in Engineering, 2011, Volume 90 (5), Pages 597–612, ISSN 0029-5981.

[49] Hadoush, A., van den Boogaard, A.H., Time Reduction in Implicit Single Point Incremental Forming Simulation by Refinement-Derefinement, International Journal of Material Forming, April 2008, Volume 1, Issue 1 Supplement, Pages 1167–1170.

[50] Eyckens, P., van Bael, A., Aerens, R., Duflou, J., van Houtte, P., Small-scale Finite Element Modelling of the Plastic Defromation Zone in the

Incremental Forming Process, International Journal of Material Forming, April 2008, Volume 1, Issue 1 Supplement, Pages 1159-1162.

[51] Abaqus User's Manuel, Version 6.12, Section 29.6.1.

[52] Bambach, M., Hirt, G., Performance Assessment of Element Formulations and Constitutive Laws for the Simulation of Incremental Sheet Forming (ISF), VIII. International Conference on Computational Plasticity, COMPLAS VIII, Barcelona, 2005.

[53] Laulusa, A., Bauchau, O. A., Choi, J. Y., Tan, V. B. C., Li., L., Evaluation of Some Shear Deformable Shell Elements, International Journal of Solids and Structures, Volume 43, Issue 17, August 2006, Pages 5033–5054.

[54] Gürbüz, I., Enhanced Characterization and Die Design for Sheet Metal Forming in Automotive Industry, MSc. Thesis, Atılım University, Institute of Science and Technology, 2014.

[55] Hypermill User's Manuel, 2010.

[56] Skjoedt, M., Bay, N., Endelt, B., Ingarao, G., Multi Stage Strategies for Single Point Incremental Forming of a Cup, International Journal of Material Forming, April 2008, Volume 1, Issue 1 Supplement, Pages 1199-1202.

[57] Kitazawa, K., Nakanei, M., Hemi-Ellipsoidal Stretch-Expanding Of Aluminum Sheet By CNC Incremental Forming Process With Two Path Method, *Keikinzoku/Journal of Japan Institute of Light metals,* 47, (1997), 440-445, (in Japanese).

[58] Duflou, J. R., Lauwers, B., Verbert, J., Study on the Achievable Accuracy in Single Point Incremental Forming, Advanced Methods in Material Forming, 2007, pp 251-262.

[59] Ambrogio, G., Costantino, I., De Napoli, L., Filice, L., Fratini, L., Muzzupappa, M., Influence Of Some Relevant Process Parameters On The Dimensional Accuracy In Incremental Forming: A Numerical And

Experimental Investigation, Journal of Materials Processing Technology, Volumes 153–154, 10 November 2004, Pages 501–507.

[60] Hirt, G., Junk, S., Bambach, M., Chouvalova, I., Process Limits and Material Behavior in Incremental Sheet Forming with CNC-Tools, 2003, Materials Science Forum, Volumes 426-432, Pages 3825–3830

[61] GOM-ATOS v6.2, User Information. Braunschweig, Germany, 2009, Chapter A, p. 4-7.

[62] GOM-ARGUS v6.2, User Information. Braunschweig, Germany, 2009, Chapter A, p. 3-9.